Assessment of Seismic Behavior of Mid-Rise R/C Slab Column Buildings in Cyprus Using Fragility Curves and Artificial Neural Network

Ali Kia

Submitted to the
Institute of Graduate Studies and Research
in partial fulfillment of the requirements for the Degree of

Doctor of Philosophy
in
Civil Engineering

Eastern Mediterranean University
February 2015
Gazimağusa, North Cyprus

Approval of the Institute of Graduate Studies and Research

—————————————————
Prof. Dr. Serhan Çiftçioğlu
Director

I certify that this thesis satisfies the requirements as a thesis for the degree of Doctor of Philosophy in Civil Engineering.

—————————————————
Prof. Dr. Özgür Eren
Chair, Department of Civil Engineering

We certify that we have read this thesis and that in our opinion it is fully adequate in scope and quality as a thesis for the degree of Doctor of Philosophy in Civil Engineering.

—————————————————
Asst. Prof. Dr. Serhan Şensoy
Supervisor

Examining Committee
———

1. Prof. Dr. Alemdar Bayraktar   —————————————————

2. Prof. Dr. Ahmet Yakut   —————————————————

3. Asst. Prof. Dr. Mürüde Çelikağ   —————————————————

4. Asst. Prof. Dr. Giray Ozay   —————————————————

5. Asst. Prof. Dr. Serhan Şensoy   —————————————————

ABSTRACT

One of the structural systems in Cyprus is slab-column frame buildings with wide beams and rectangular columns. In this study 4-, 6- and 8-story buildings with regular plan of mid-rise wide-beam buildings in Famagusta, Cyprus were defined. Fragility curves were employed as one of the important seismic assessment tools and constructed using incremental dynamic analysis (IDA) method. In this study, a set of earthquake records were chosen to represent the soil properties and strike-slip type of faulting in this region which also have a good correlation with Turkish design spectrum. These records were scaled to ten different levels of peak ground acceleration (PGA) from PGA=0.1 to PGA=1.0g. The Park & Ang damage index and log-normal cumulative distribution function were used as proper damage index and probability function, respectively. Based on IDA curves, two damage levels including; immediate occupancy (IO) and collapse prevention (CP) were obtained for this type of building and they were compared with criteria which are suggested by FEMA 356. Also, the effects of P-delta and aftershock were evaluated.

Since the nonlinear time history analysis is time consuming, requires complex calculations and powerful computers, for rapid evaluation of damage the artificial neural network (ANN) was used as an efficient tool. In this study, using the results of numerical simulations, 600 data were generated and applied to a multi-layer perceptron (MLP) neural network in order to predict the imposed damage of these sample buildings. In training process, ten different activation functions were examined to find the best kernel function. Also the optimum hidden layer neurons were calculated by using minimum test error method. In this network, 70 %, 15 % and 15 % of all data were used for training, validating and testing process, respectively. Based on obtained

results from ANN, the fragility curves were drawn and compared with the obtained curves from IDA. This application of network also is able to predict the top displacement and the base shear force of sample buildings.

Another application of ANN was used for classification of global imposed damage based on Park & Ang investigation. For this aim, two networks include; multi-class support vector machine (M-SVM) and combination of MLP neural network with M-SVM (MM-SVM) were applied and the label of each actual class was compared with predicted class. The results showed that the ANNs are able to predict and classify the damages with high accuracy and also they can be used as an appropriate and reliable alternative tool for rapid seismic evaluation of structural systems.

Finally, an existing model of R/C wide-beam building (test model) was considered and the obtained fragility curves from classical method and ANN were compared and discussed.

ÖZ

Kıbrıs genelinde betonarme yapı sistemleri arasında döşeme kalınlığında geniş kirişlerin dikdörtgen kolonlar tarafından taşındığı sistemler de bulunmaktadır. Bu çalışmada bu özelliklere sahip 4, 6 ve 8 katlı binalar Gazimağusa şehrinde bulunan yapı özelliklerini taşıyacak şekilde oluşturulmuştur. Bu yapılar için kırılganlık eğrileri, artımsal dinamik analiz (ADA) yöntemi kullanılarak oluşturuldu. Bu amaçla Gazimağusa bölgesinin zemin koşullarını da dikkate alan ve Türk Deprem Yönetmeliği tasarım spektrumuna uyumlu yan atımsal deprem kayıtları kullanılmıştır. Tasarım spektrumuna uyumlu deprem kayıtları en büyük yer ivmesi 0.1g den 1.0g'ye kadar on farklı seviyede ölçeklendirilerek kullanılmıştır. Çalışma kapsamında Park ve Ang hasar endeksi ve log-normal yığılımlı olasılık dağılımı kullanılarak kırılganlık eğrileri elde edildi. Oluşturulan ADA eğrilerinden "hemen kullanım" ve "göçme öncesi" hasar durumları bu yapılar için belirlenmiş ve FEMA356 kriterleri ile de karşılaştırılmıştır. İkinci mertebe moment etkisi ve artcı şoklar da bu çalışma kapsamında değerlendiridi.

Linear olmayan dinamik analizlerin oldukca zaman aldığı ve güçlü bilgisayar gerektirmesinden ötürü, özellikle deprem dayanımının hızlı belirlenmesi (ön değerlendirme) çalışmalarında etkili olacak Yapay Sinir Ağları (YSA) yöntemi bu çalışma kapsamında etkili bir araç olarak kullanılmıştır. Bu bağlamda, nümerik similasyon yapılarak oluşturulan 600 veri çok-katmanlı algılayıcı (MLP) sinir ağları algoritmasına uyarlanarak örnek olarak oluşturulan yapıların hasar durumları tahmin edildi. YSA alıştırma aşamasında on değişik aktivasyon fonksiyonu incelenip en iyi çekirdek fonksiyon bulundu. Buna ilaveten optimum saklı sinir hücreleri en az hata oluşturulacak şekilde hesaplandı. Bu ağda, toplam verilerin %70'i alıştırma, %15'i

doğrulama ve %15'i ise test aşamalarında kullanıldı. YSA analizinden elde edilen sonuçlarara göre kırılganlık eğrileri çizildi ve ADA analizleri sonucunda elde edilen eğrilerle karşılaştırıldı. Bu uygulama ayrıca örnek yapılarda en büyük deplasmanın ve taban kesme kuvvetinin belirlenmesinde de kullanıldı.

YSA ayrıca Park ve Ang global hasar sınıflandırılması uygulamaları için de kullanıldı. Bu amaçla çoklu-sınıf destek vektör mekanizması (M-SVM) ve MLP sinir ağı ile kombine M-SVM (MM-SVM) uygulanıp her bir hasar sınıfı tahmin edilen hasar sınfı ile karşılaştırıldı. Analiz sonuçları göstermiştir ki YSA yöntemi hasar durumlarının belirlenmesinde ve sınıflandırılmasında yüksek doğruluk oranı ile kullanılabilir. Ayrıca YSA ile belirlenen hasar düzeyleri hızlı deprem değerlendirilmesi amacı ile farklı yapı sistemleri için de kullanılabilir.

Son olarak Gazimağusa bölgesinde mevcut bir yapı (kullanılan örnek yapılardan farklı) çalışma kapsamında incelenip YSA algoritması ile elde edilen sonuçlar ADA analiz sonuçları ile karşılaştırılıp sonuçlar tartışıldı.

Anahtar Kelimeler: Artcı şok, Yapay Sinir Ağları, hasar sınıflandırılması, hasar tespiti, kırılganlık eğrileri, artımsal dinamik analiz, Park ve Ang hasar endeksi, Betonarme geniş-kirişli yapılar, deprem davranışı.

DEDICATION

To My Parents

ACKNOWLEDGMENT

I am appreciative of my supervisor Asst. Prof. Dr. Serhan Şensoy for his guidance and encouragement throughout of this study.

TABLE OF CONTENTS

LIST OF TABLES

LIST OF FIGURES

LIST OF ABBREVIATIONS

ACI   American Concrete Institute

ANFIS   Adaptive Neuro-Fuzzy Inference System

ANN   Artificial Neural Network

BPNN   Back-Propagation Neural Network

CANN   Combined Artificial Neural Network

CMLP   Combined Multi-Layer Perceptron

CP   Collapse Prevention

DF   Dominant Frequency

DI   Damage Index

EDP   Engineering Demand Parameter

FEMA   Federal Emergency Management Agency

FN   False Negative

FNN   Fuzzy Neural Network

FP   False Positive

GA   Genetic Algorithm

GPS   Global Position System

IDA   Incremental Dynamic Analysis

IO   Immediate Occupancy

KKT   Karush-Kuhn-Tucker

LS   Life Safety

LSSVM   Least Square Support Vector Machine

MCEER   Multidisciplinary Center for Earthquake

                                Engineering Research

MLP	Multi-Layer Perceptron
MSE	Mean Square Error
M-SVM	Multi-Support Vector Machine
NPV	Negative Predictive Values
ODI	Overall Damage Index
OLS	Orthogonal Least Squares
PGA	Peak Ground Acceleration
PGD	Peak Ground Displacement
PGV	Peak Ground Velocity
PEER	Pacific Earthquake Engineering Research
PHM	Polygonal Hysteretic Model
PPV	Positive Predictive Values
RBF	Radial Basis Function
R/C	Reinforced Concrete
RMSE	Root Mean Square Error
SD	Spectral Displacement
SDI	Story Damage Index
SHM	Smooth Hysteretic Model
SVM	Support Vector Machine
TEC	Turkish Earthquake Code
TL-ANN	Three-Layered Artificial Neural Network
TN	True Negative
TP	True Positive
UAE	United Arabic Emirates
USA	United States of America

LIST OF SYMBOLS

ACC	Accuracy
A	Number of input layer neuron
α	Stiffness parameter
α_i	Lagrange factor
B	Number of hidden layer neuron
β_1	Strength parameter (ductility based)
β_2	Strength parameter (energy based)
C	Penalty factor
C_0	Seismic zone factor
δ	Horizontal displacement
δ_i	Slack variable
δ_m	Maximum experienced deformation of the structural element
δ_u	Ultimate deformation of the structural element
f'_c	Compressive strength of concrete
fsu	Ultimate stress of steel bar
fy	Yield stress of steel bar
f	Activation function for hidden layer
g	Activation function for output layer
h	Story height
I	Residential building factor
K	Reinforce concrete moment frame factor

L_p	Saddle point
$\grave{\mu}$	Mean of error
μ_i	Lagrange factor
PRE	Precision
P_y	Yield strength of the structural element
P_i	Additional gravity load shear
R	Correlation coefficient
SEN	Sensitivity
SPC	Specificity
S	Spectral factor
T	Fundamental period
T_0	Soil period
$\int dE_h$	Hysteretic energy absorbed
Φ	Normal distribution function
σ	Standard deviation of error
γ	Slip or crack parameter
w	Neuron weight

Chapter 1

INTRODUCTION

1.1 Background

The natural disasters such as earthquake and strong winds may lead to catastrophic results, such as, earthquakes on January 26, 2001 in India (20,005 killed, 166,836 injured, 339,000 buildings destroyed), February 24, 2003 in china (263 killed, 4,000 injured, 10,000 buildings destroyed), May 1, 2003 in eastern of Turkey (176 killed, 521 injured), May 21, 2003 in northern Algeria (2,266 killed, 10,261 injured) and February 24, 2004 in Morocco (628 killed, 926 injured) (USGS, 2014). Engineering measures have been taken to reduce the risks of earthquakes and damages caused by them including evaluation and identification of the behavior of materials particularly concrete and steel, improvement in analysis and design of buildings, control and more precise monitoring of the implementation and better workmenship.

Generally, the seismic behavior of buildings are commonly impressed by three factors including; lateral load acting, geometry of buildings and the properties of materials in linear and nonlinear states which are used in construction. Therefore, the identification of these aspects to predict the structure responses are significant. On the other hand, the accurate determination of earthquake loads are difficult, therefore this factor is one of the major uncertainties to identify seismic response of buildings. Similarly, geometries of buildings are different from each other and it is very difficult to have an exact model. Also the material properties in construction are depending on

manufacturing processes and there is a confusion in selecting appropriate material properties. However, these uncertainties can be decreased by collecting data throughtout proper engineering knowledge. In the last decades, engineers tried to improve the numerical and experimental methods in order to achieve the more realistic seismic responses of buildings. Indeed, these results can be used in two ways; seismic vulnerability assessment and retrofitting of existing buildings that were designed and constructed based on previous codes and still in use, improve design codes to reach more reliable design and construction for new buildings.

1.2 Objectives of the study

The primary goal of this study is to evaluate the vulnerability of existing reinforced concrete (R/C) wide-beam buildings which are built in the Mediterranean area and is also available in North Cyprus. Since this type of buildings were built in the last few decades and also still in use, their seismic behavior should be considered seriously. For this purpose, the fragility curves were selected as an efficient tool and by considering the real behavior of construction material, selecting a set of ground motion record which has most correlation with design spectrum and using nonlinear time history analysis, behavior of these buildings type were evaluated. In addition, incremental dynamic analysis (IDA) curves were applied in order to find the damage criteria for this type of buildings and the obtained results were compared with suggested criteria based on FEMA 356 (2000). In the meantime, the P-Delta and also aftershocks effects were discussed.

Another aim of this study is to apply the artificial neural network (ANN) as an alternative and rapid evaluation method with function approximation operation as a fast, efficient and accurate tool to predict the amount of imposed damages and drive the fragility curves. Also this method can be used as an alternative method instead of

2

FEMA 154 (2002) with more accuracy, time saving ability and high efficient. This model of network also can be able to predict another response of buildings such as the top displacement and the base shear force. Furthermore, it was applied to determine the effective ground motion parameters.

Another model of ANN with clustering and classification capability was selected in order to classify the global damage of buildings to three classes that includes; Repairable (Economic), Beyond Repair (Not Economic) and Loss of Building (Collapse). These networks can create a compatibility model for similar buildings with additional data beyond whatever is previously used in order to predict and classify the amount of imposed damage due to earthquake in minimum time and high precision and then drive the fragility curves with establishing a good relation between the structural and ground motion parameters as input parameters and damage values as output parameters of network.

1.3 Overview of the thesis

This thesis is composed of seven chapters. The first chapter describes the introduction. It briefly discusses about the problem statements, aims and scopes and includes; background, objectives of the study and overview of the thesis. Chapter two concerns with literature review. This review includes the application of fragility curves for seismic evaluation of R/C buildings and the extensive usage of ANN in several fields of civil engineering in order to solve the different problems with prediction and classification approach. Chapter three illustrates the method and requirements that were carried out in this research. The analysis and results for obtaining the fragility curves based on IDA and ANN are explained and presented in chapters four and five, respectively. Chapter six discusses about obtained results throughout the thesis, comparison between obtained fragility curves based on classical method (IDA) and

computational method (ANN) and finally an existing R/C wide-beam building (case study) is evaluated. Lastly, the conclusion of this study is presented in chapter seven. It comes together with the appendices which consist of Matlab codes and reference links.

Chapter 2

LITERATURE REVIEW

The significance of danger for buildings caused by earthquakes worldwide is being increasingly perceived as a result of poor quality materials, imprecision in construction and failed supervision. Due to the improvement in structural engineering, such as the study of a building's seismic behavior and observation of a building's damage, radical changes can now be observed in this field. It is important to evaluate existing structures in order to determine some ways for improving the seismic resistance of vulnerable buildings. In recent years, several different methods of retrofitting have been developed to upgrade the seismic performance of existing undamaged buildings before being subjected to an earthquake (Elnashai and Sarno, 2008). For instance, retrofitting can be conducted by adding new structural elements (such as structural walls or steel braces) or by increasing the strength of weak structural elements by using concrete and/or steel jackets, fiber-reinforced polymer sheets, etc. (Durucan and Dicleli, 2010; Obaidat et al., 2011; Promis and Ferrier, 2012). Fragility curves are one of the useful tools for evaluating the seismic vulnerability of buildings. These curves indicate the estimation of the damage probability as a function of the ground motion indices. Ozel et al. (2011) used fragility analysis to investigate the seismic reliability of mid-rise R/C building retrofitted with eccentric steel braces. To increase the seismic reliability of existing buildings, D-, K-, and V-type eccentric braces were used, and the fragility curves were compared before and after retrofits. Buratti et al. (2010) investigated seismic fragility curves for R/C frame structures considering the uncertainties in both

structural parameters and seismic excitation. The fragility curves obtained by different methods were compared, using the results from a full Monte Carlo simulation as the reference solution. A seismic fragility assessment of typical low- and mid-rise R/C buildings in Turkey was conducted by Erberik (2008). The damage was estimated by using the generated fragility curves. The estimated damage distribution seemed to be comparable to the actual damage data. Kappos (2010) provided a methodology for the derivation of capacity curves and fragility curves in terms of peak ground acceleration (PGA) and spectral displacement (SD) for various types of R/C buildings in Greece. Mwafy (2012) developed analytical fragility curves for modern high-rise buildings in the United Arabic Emirates (UAE), and the significance of assessing the seismic risk of this type of buildings under the effects of anticipated seismic scenarios was emphasized. The vulnerability assessment analysis of some existing typical R/C school buildings in Albania was performed by Baballeku et al. (2008). Pushover analyses were performed to provide their respective capacity curves, and the probable damage levels of the buildings were assessed by using the fragility curves.

Nowadays, one of the popular computational models which have been applied widely in different fields of science is ANN. Recently, ANNs are used in different fields of civil engineering, such as, traffic management and transportation systems, damage prediction of structures, thermo-graphic inspection of electrical installations within buildings, forecast water pressure in pipes, etc., in order to solve complex relationships by considering effective indices and establishing a good relationship between input and output parameters. Moreover, these networks can be applied in damage classification problems.

For confined reinforced concrete columns containing fiber-reinforced polymer, a combined ANN (CANN) was presented by Köroglu et al. (2012). The network can

estimate the flexural capacities with high accuracy. Tesfamariam and Liu (2010) used eight different neural networks for classification of reinforced concrete buildings to three classes; damaged, life safety (LS) and immediate occupancy (IO). The obtained results showed that the performance of classification depends on the characteristics of database. A MLP neural network was employed in order to evaluate the effective design parameters of R/C buildings under earthquake by Araslan (2010). He considered 256 buildings between 4 and 7 story with change in quality of R/C structure materials and load-bearing system to obtain the buildings capacity. The results showed that among eight considered parameters, short column formation and shear wall ratio have the most effect on buildings performance. On the other hands, transverse reinforcement and compressive strength of concrete were identified as the least significant parameters. Two different neural networks; a back-propagation neural network (BPNN) and a fuzzy neural network (FNN) were used in order to measure the pressure on a large gymnasium roof by Fu et al. (2007).They showed that BPNN can be applied as effective tool for the design and analysis of wind effects on large roof structures. Gonzalez and Zapico (2008) suggested a method for seismic damage identification of steel moment-frame buildings using a multi-layer perceptron (MLP) neural network. The obtained results from MLP were accepted with minimum error of test and train data. In order to evaluate the damage level of beams, a neural network with back-propagation algorithm was used by Li and Yang (2008). They showed that the obtained results of this network were having enough efficiency.

The first classification algorithm was presented by Fisher (1936). In this algorithm, minimizing the classification error of train data was evaluated as an optimization criterion. This method has been used in many classification algorithms, yet there are some problems encountered mainly the generalization properties of the classifiers,

which are not directly involved in the cost function. Also for doing the training process, determining the structure of network was not easy. As an example, determining the optimum number of neurons in the hidden layers of the MLP neural networks or the number of Gaussian functions in radial basis function (RBF) neural networks are difficult and time consuming. Cortes and Vapnik (1995) introduced a new learning statistical theory which led to present the support vector machines (SVMs). The significant features of these networks are their ability to minimize the classification errors, maximize the geometric margins between classes, design the classifiers with maximum generalization, and automatically determining the architecture of network for classifiers and modeling the nonlinear separator functions using nonlinear cores.

In a tunnel construction, an intelligent controlling system was presented by Jun et al. (2013). This system needed to recognize the geophysical parameters to find the optimum solution of problems. Therefore, a nonlinear optimization technique was employed using the least square support vector machine (LSSVM). The results showed that this method is timesaving and easy to use in local optimal problems. Mingheng et al. (2013) employed several different models of traffic flow using SVM to find the best intelligent traffic control tool. They obtained that amongst the three proposed models, the SVM with the historical pattern data for the target road section model has the best performance. Vafaei et al. (2013) applied MLP neural network to identify the real-time seismic damage for concrete shear walls. It was observed that the neural network could detect the amount of imposed damage with high accuracy. Two different neural networks; the adaptive neuro-fuzzy inference system (ANFIS) and the three-layered artificial neural network (TL-ANN) model were used to estimate the earthquake load reduction factor for industrial structures by Ceylan et al. (2012). They showed that the ANFIS model was more successful than the TL-ANN model. Xie et

al. (2013) investigated the amount of voids inside the concrete using SVM. The grid-algorithm and the genetic-algorithm were used to determine the kernel function and network parameters. The obtained results presented that the SVM exhibits a promising performance for identification of voids inside the concrete. In addition, ANNs were used in conjunction with each other. Koroglu et al. (2012) applied MLP neural network in two models; Single MLP and combined MLP with itself (CMLP) for estimation of the flexural capacity for the quadrilateral FRP-confined R/C columns. They obtained the model of CMLP had lower prediction error than the single MLP model. In order to classify the cardiac arrhythmias, Castillo et al. (2012) considered a hybrid intelligent system which consists of the Fuzzy K-Nearest Neighbors with the MLP and very high classification rate was obtained. To predict the Short-Term wind power generation, combination of genetic algorithm (GA) and orthogonal least squares (OLS) algorithm with RBF neural network was proposed by Chang (2013). The test results indicated the proposed model is reliable with the sufficient performance.

Since many researches have been done on different types of buildings which are constructed based on previous code and instruction, but unfortunately no research has been centrally done on wide-beam R/C building. Also this type of buildings are available and still in use, therefore the seismic evaluation of these buildings is significant. For this aim, some criteria should be considered, such as, nonlinear behavior of material including concrete and steel bar, how to distribute and absorb the earthquake energy by structural elements, determine the damage level criteria and compare with existing procedure guideline like FEMA 356, assessment of the collapse processing and etc. Since doing the nonlinear time history analysis is difficult, time consuming and needs high engineering knowledgement, thus in this research it was attempted to present a new method in order to evaluate the seismic performance of

buildings with high accuracy, minimum time and simplicity of operation. This method can be used for evaluation of an extensive space like a city by considering some suitable sample from a set of specified buildings type and carrying out nonlinear dynamic analysis. Then using the obtained data, the seismic performance of remained buildings will be predicted with high precision. Many applications of this strong mathematical tool have been done in many fields of science such as medical science, different engineering fields, aerospace, military science and etc. Also this method can be used for retrofitting programs, disaster management and insurance company. It might be said that the performance of ANN in simplest case is like nonlinear regression but more complicated. Indeed the ANN made a relation between input and output parameters using some functions such as tangent hyperbolic, sine hyperbolic, etc. Then by using this pattern, the test data were evaluated. Also the different models of ANN with various applications were used in this research as powerful mathematical tool which can solve the complex and difficult problems that cannot be solved by prevalent mathematical methods.

Chapter 3

METHODOLOGY

3.1 Sample buildings and material properties

One of the existing building types in Cyprus is slab-column frame buildings with wide beams and rectangular columns where the beam height is equal to the slab thickness. This type of building is made in the Mediterranean area such as Spain, Italy, Greece and is also available in North Cyprus (Climent et al., 2009; Kulkarni and Li, 2009; Climent et al., 2010; Goldsworthy and Abdouka, 2012). The structural system of exterior wide beam-column connections is shown in Figure 3.1.
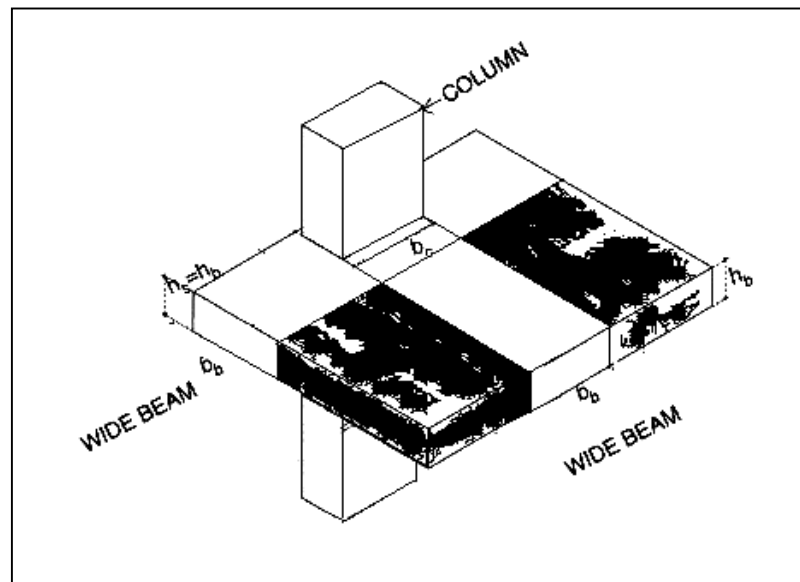
Figure 3.1: Typical exterior wide beam-column connection

This type of buildings were largely used by many architects because it has more flexibility for definition of spaces and also effective in reducing the use of formwork.

However, this model of buildings has several problems, such as, lack of sufficient transferring of the bending moment from the wide beam to the column, poor energy absorption capacity, inadequate lateral stiffness, etc. Using the wide beam-column connection has been limited or prohibited in seismic regions. As an example, the ACI-ASCE (1991) prohibited using the wide beams in structures in order to dissipate energy in response of ground motions during inelastic behavior of the structure. ACI 318-83 (1983), ACI 318-89 (1989), ACI 318-95 (1995) and ACI 318-99 (1999) codes permitted wide beams if:

$$b_b \leq (b_c + 1.5h_b) \tag{3.1}$$

The New Zealand standard NZS3101-95 (1995) limited b_b to:

$$b_b \leq min\{ b_c + 0.5h_c; 2b_c\} \tag{3.2}$$

The more recent ACI 318-05 (2005) and ACI 318-08 (2008) limit b_b to:

$$b_b \leq min\{ b_c + 1.5h_c; 3b_c\} \tag{3.3}$$

where b_b is the width of wide-beam, b_c is the width of column, h_c is the depth of column, h_b is the height of wide-beam or slab thickness (Climent et al., 2010).

In this study, three R/C wide-beam buildings with the 4-, 6- and 8-levels were defined with regular plan in order to present the mid-rise buildings in Famagusta city. Based on information mentioned in existing building plans, these buildings were designed according to 1975 version of the Turkish seismic design code (TEC-1975, 1975). Also, the American Concrete Institute (ACI) building code was used for designing the structural components (ACI 318-83, 1983). The duality in selecting codes (i.e. Turkish and American codes) may be a drawback for such buildings. Moreover, based on previous researches and experimental tests of this building type, the material strength of concrete and steel of these buildings stock were measured as 15MPa for compressive strength of concrete and 220MPa and 300MPa for yield and

ultimate strength of steel, respectively (Rasol, 2014; Arslan, 2010). Soil type IV (D-type) was specified based on this zone property.

3.1.1 1975 Seismic Design Code

The TEC regulation of 1975 has been introduced and used since 1975 as a seismic code to be applied in disaster areas. The code considered the spectrum coefficient based on the natural period of the building and soil conditions. Ductility term was explicitly used for this code and also base shear factor was calculated based on this term in order to provide the sufficient resistance under earthquake. The earthquake coefficient of the 1975 code is calculated as:

$$C = C_0 \cdot K \cdot I \cdot S \tag{3.4}$$

where C_0 is seismic zone factor, K is a factor related to structure system type, I is an important factor and S is a spectral factor (Ilki and Celep, 2012; Soyluk and Harmankaya, 2012)

3.1.2 ACI 318-83 Code

ACI 318-83 (1983) regulation has been presented by the ACI for designing the structural concrete members with considering the minimum requirement. This code designs the concrete members using the ultimate strength of materials by considering appropriate safety margin through applying reduction factors. Also these factors include the safety of material properties for controlling the strength, any variations in concrete member dimensions and steel positions, lack of precision in design and considering the structural members ductility. These factors are 0.9 for flexure and axial tension, 0.75 and 0.7 for axial compressions with and without flexure, respectively. Furthermore, factors 0.85 for shear and torsion and 0.7 for bearing on concrete were considered (ACI 318-83, 1983).

Based on observations of wide-beam buildings, dimensions of the columns were selected as rectangular sections with aspect ratios (width/height ratio of cross section

area) between 1.5 and 3. Also the beams with same thickness of slab (15cm) were used as a connection elements between columns. SAP2000 was used in order for primary design of these models. Figures 3.2-3.7 depict the plans and section views for the 4-, 6-, and 8-story buildings, respectively. Since the plans of studied buildings were rectangular in shape with different strengths in the x- and y-directions, therefore the samples were selected in order to investigate in the weaker direction (x direction) only.
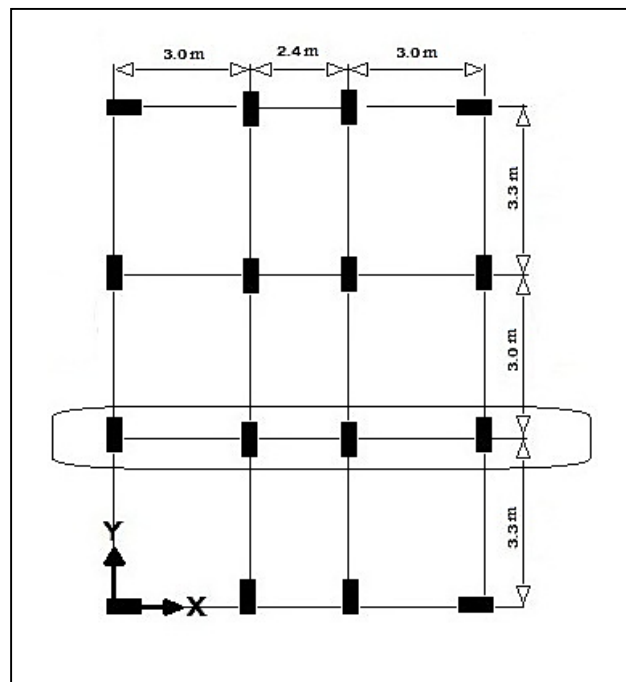
Figure 3.2: Plan view of four-story building
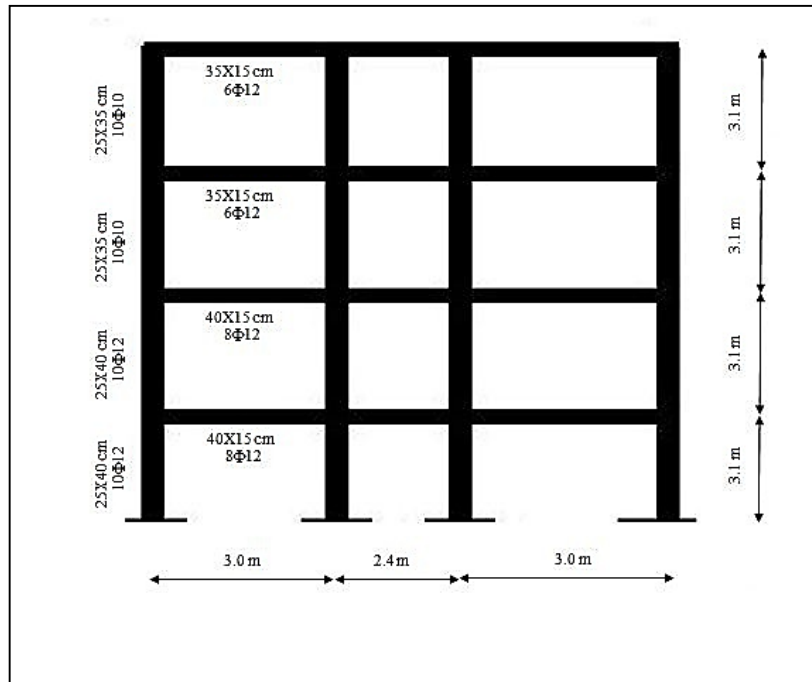
Figure 3.3: Section view of four-story building
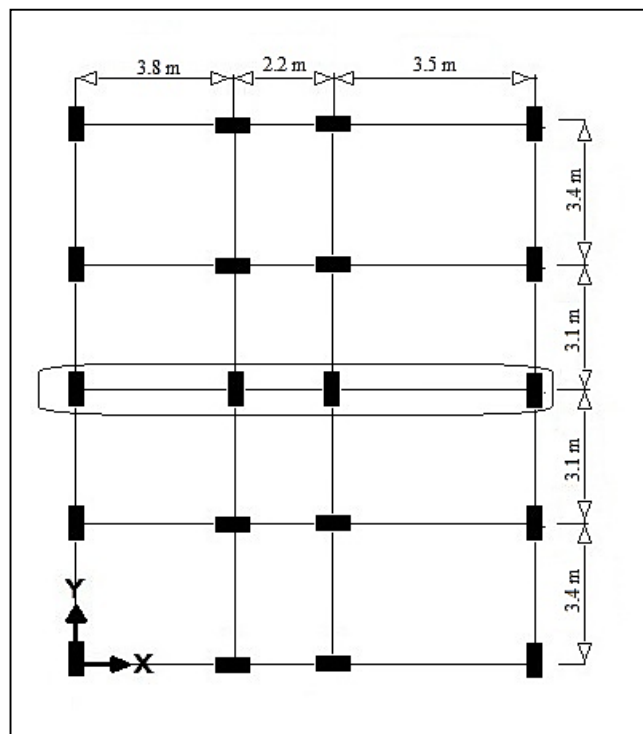
Figure 3.4: Plan view of six-story building
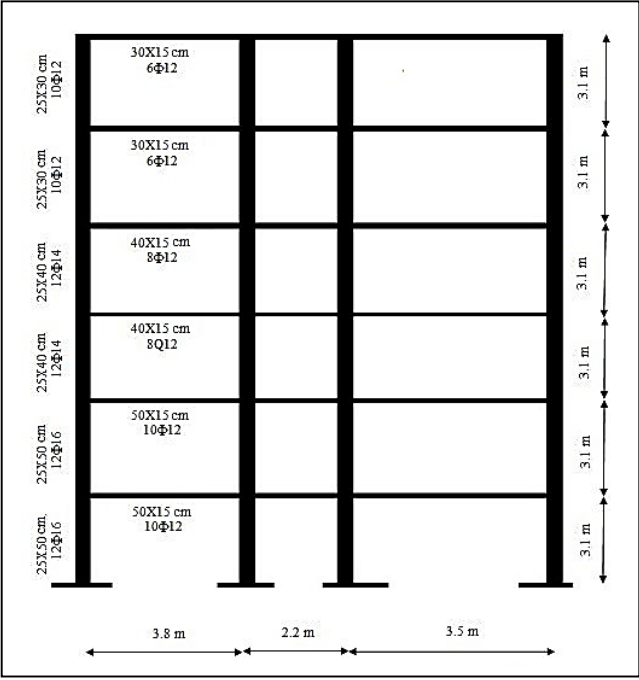
Figure 3.5: Section view of six-story building
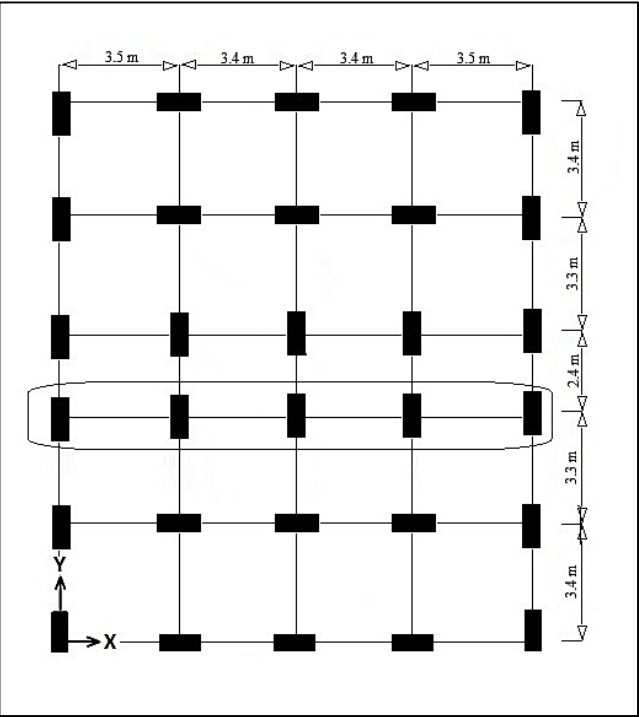
Figure 3.6: Plan view of eight-story building

16
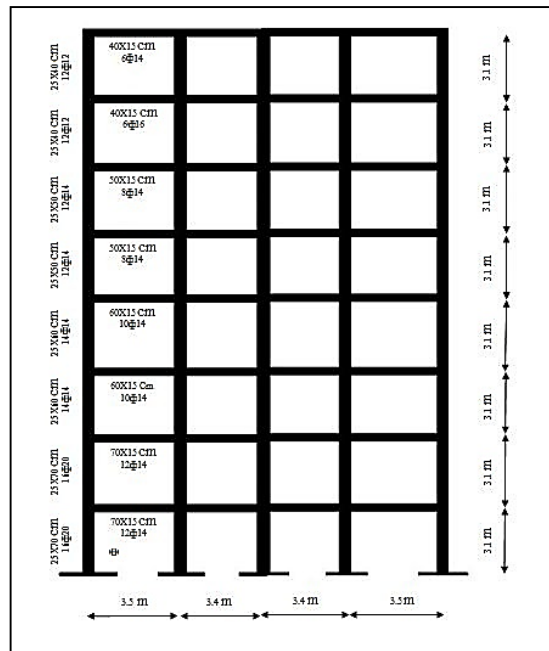
Figure 3.7: Section view of eight-story building

3.2 Ground motions

A significant step for performing nonlinear time history analysis is selection of a representative set of ground motion records which have high correlation with design spectrum and also cover the site properties. For this aim, the effective parameters of earthquakes in a region should be considered. These parameters include; the distance from the fault line, the soil profile, the time duration of the earthquake as well as the variation in intensity, amplitude and frequency content, etc. For Cyprus area, a strike-slip fault mechanism was specified by Cagnan and Tanircan (2010).

In this study, due to uncertainty and lack of strong ground motion data for the Famagusta region, a series of earthquakes that occurred in other areas of the world were selected. The records were taken from the Berkeley data-base site (PEER, 2013). These records have been chosen based on the strike-slip fault mechanism, the D (Z4-type according to TEC (2007)) site classification (Shear-wave velocity < 180 m/s) and

17

a distance less than 100 km from the fault line which is representative for Famagusta region (Cagnan and Tanircan, 2010).

For the best set of records, different methods, such as, the time domain, the frequency domain or the time-frequency domain adjustments were suggested (Hancock et al., 2006; Rizzo et al., 1975; Suarez and Montejo, 2005). These methods are used to match the response spectrum with design spectrum but they lead to change the time or frequency content of the original records. In this study, twenty records were selected carefully in order to have most correlation with the design spectrum specified by the Turkish design code (TEC, 2007) using trial and error approach. For this purpose, twenty records considered randomly from a larger set of proper input records and then by calculating the mean of these twenty records, the amount of correlation between mean and design code are calculated. This process is repeated until to reach the best correlation value. The mean and response spectrums of individual records are shown in Figure 3.8. Moreover, the characteristics of these ground motions are tabulated in Table 3.1.
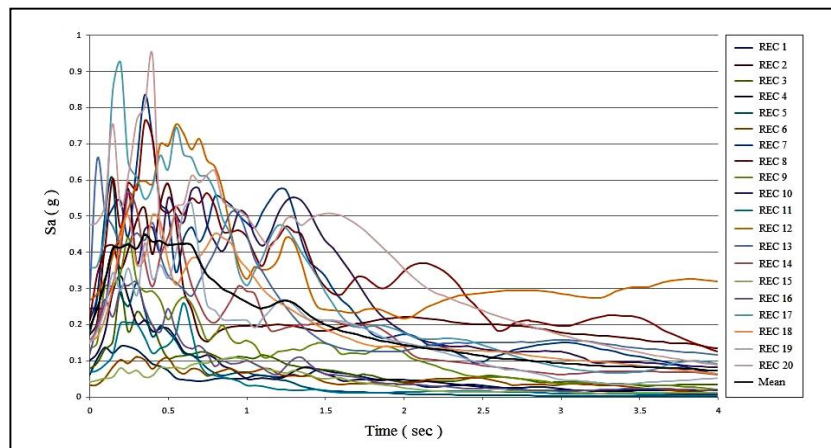
Figure 3.8: The mean and response spectrums of individual records

Table 3.1: Characteristics of the twenty natural records

Name	Event	Year	Time Effective (s)	PGA (g)	PGV (cm. s⁻¹)	PGD (cm)
REC1	Park field	1966	27.80	0.059	5.90	2.86
REC2	Park field	1966	06.99	0.476	79.34	22.59
REC3	Imperial Valley-06	1979	12.82	0.171	42.75	02.83
REC4	Imperial Valley-06	1979	23.32	0.078	13.00	24.18
REC5	Victoria- Mexico	1980	10.64	0.101	7.77	05.99
REC6	Victoria- Mexico	1980	15.37	0.150	25.00	09.54
REC7	Westmorland	1981	08.40	0.171	05.90	00.47
REC8	Westmorland	1981	18.50	0.155	25.83	12.96
REC9	Morgan Hill	1984	35.98	0.032	05.33	02.21
REC10	Superstition Hills-B	1987	16.86	0.211	30.14	20.44
REC11	Superstition Hills-B	1987	28.75	0.207	34.50	21.31
REC12	Superstition Hills-B	1987	16.05	0.358	44.75	17.46
REC13	Landers	1992	36.32	0.136	11.33	05.03
REC14	Landers	1992	17.62	0.245	49.00	43.66

REC15	Kobe- Japan	1995	24.52	0.070	4.38	01.54
REC16	Kocaeli- Turkey	1999	15.34	0.268	67.00	57.17
REC17	Kocaeli- Turkey	1999	09.39	0.242	30.25	29.76
REC18	Kocaeli- Turkey	1999	14.99	0.152	21.71	09.81
REC19	Duzce- Turkey	1999	19.22	0.042	8.40	08.09
REC20	Duzce- Turkey	1999	16.09	0.114	11.40	9.74

In order to adapt the mean response spectrum with Turkish design spectrum (TEC-2007, 2007), scaling the real ground motion records is necessary. Therefore, based on Figure 3.8, the mean curve from this set of records has good correlation with target curve (Turkish design spectrum) but they are not perfectly fitting to each other. Therefore, an optimization program was written via MATLAB software in order to find the best scale of mean records using root mean square error (RMSE) reduction technique. Flowchart of the proposed optimization algorithm is depicted in Figure 3.9.
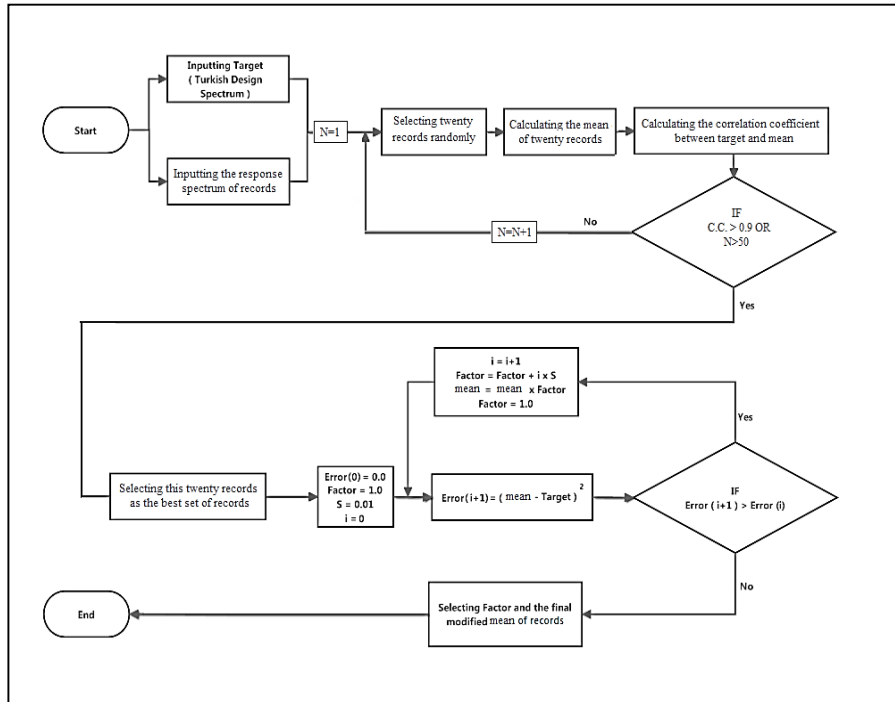
Figure 3.9: Flowchart of the search optimization algorithm

Therefore, based on RMSE reduction technique, factor 2.3 was obtained for this set of records. The mean and response spectrums of this set of scaled records are shown in Figure 3.10.
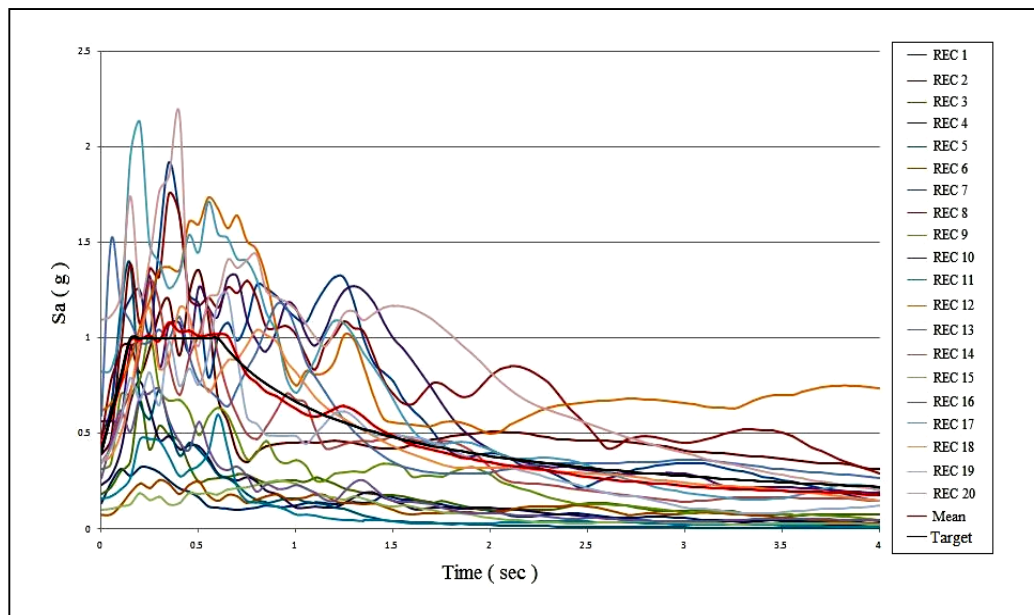
Figure 3.10: Target (Turkish design spectrum), mean and response spectrums of individual modified records

3.3 Damage indices

In order to evaluate the damage level of structures under earthquake loads, several different indices were presented by researchers. These criteria provide the value of structural failure based on a proper theoretical background. Mathematical models of damage that have been determined based on assessment of vulnerabilities can be defined as functions of structural strength, ductility, the distance from the fault line, the duration of the earthquake, etc. Gradually, combination of visual observations of damage and numerical analysis and extensive investigation in this field led to defining the damage indices for the evaluation of a building's vulnerability. Recently, considering the seismic behavior of structures under oscillatory motions of the earth has led to improve the damage function. As continue, several important damage indices which were suggested and used for concrete buildings are presented.

3.3.1 Ductility ratio index

Ductility ratio index is defined as ratio of maximum deformation to the yield deformation and has been extensively applied to evaluate the seismic capacity of building undergoing inelastic deformation (Newmark and Rosenblueth, 1971). Experimental studies showed that this index is not properly working when shear distortion was happened in joints and the bottom bars pull out through the concrete.

3.3.2 Slope ratio index

Slope ratio index is defined as ratio of the secant slope in loading branch to the slope in unloading branch of force-displacement diagram and calculates the damage based on stiffness degradation under seismic loading (Saiidi and Sozen, 1981).

3.3.3 Normalized cumulative rotation index

Normalized cumulative rotation index is defined as ratio of total inelastic rotations during half cycles to the yield rotation and is depended on duration and intensity of the

ground motion (Allahabadi and Powell, 1988; Banon and Veneziano, 1982). The analytical analysis and experimental results showed that those of indices which calculated the damage values only based on dissipated energy or cumulative inelastic deformation cannot consider the complex process of damage propagation.

3.3.4 Inter-story drift ratio index

This index expresses the amount of damage according to a relative horizontal displacement parameter. Hueste and Bai (2007) utilized the FEMA 356 (2000) global drift limits to assess the seismic fragility of R/C buildings and compared them with drift limits based on the FEMA 356 (2000) member-level criteria. Rajeev and Tesfamariam (2012) investigated this index to evaluate the non-ductile R/C frames while considering soil-structure interaction. This index has also been applied for steel, masonry and wood buildings by several researchers (Ozel and Guneyisi 2011, Kazantzi et al. 2008, García and Negrete 2009, Park et al. 2009, Lee and Rosowsky 2006). This index is defined as:

$$DI = \frac{\delta_{i+1} - \delta_i}{h} \qquad (3.5)$$

in which δ_{i+1} is the horizontal displacement of the $(i+1)^{th}$ story, δ_i is the horizontal displacement of the ith story and h is the height between stories.

Table 3.2 represents the inter-story drift ratio limit states based on the FEMA 356 (2000) global-level criteria.

Table 3.2: Inter-story drift limit states based on FEMA 356 (2000) global-level criteria

Structure Type	Inter-Story Drift Limits (%)		
	Light Damage (IO)	Moderate Damage (LS)	Severe Damage (CP)
R/C With Shear Wall	0.5	1	2
R/C Without Shear Wall	1	2	4

3.3.5 Park & Ang index

The Park & Ang damage index was proposed by Young-Ji Park, Alfredo H.-S. Ang and Yi Kwei Wen in 1985 for the seismic vulnerability assessment of R/C buildings and is defined as the linear combination of the maximum displacement and the dissipated energy (Park et al., 1985). This index is defined in the following equation:

$$DI = \frac{\delta_m}{\delta_u} + \frac{\beta}{\delta u.P_y} \qquad (3.6)$$

where δ_m and δ_u are the maximum experienced deformation and ultimate deformation of the structural element, respectively; P_y is the yield strength of the structural element; $\int dE_h$ is the hysteretic energy absorbed by the structural element during the response history; and β is a constant parameter which is considered equal to 0.1 for nominal strength deterioration (MCEER-09-0006, 2009).

The Park & Ang damage index can be extended to the story and overall scales by a summation of damage indices, as follows:

$$SDI_j = \sum_{k=1}^{m_j} \lambda_{kj}.DI_{kj} \qquad (3.7)$$

$$\lambda_{kj} = \frac{E_{kj}}{\sum_{i=1}^{m_j} E_{ij}} \qquad (3.8)$$

in which SDI_j is the damage index of the jth story, DI_{kj} is the damage index of the kth

element of the jth story, E_{kj} is the hysteretic energy of the kth element of the jth story, $Ej=\sum_{i=1}^{m_j} E_{ij}$ is the hysteretic energy of the jth story, and m_j is number of the elements of the jth story. Additionally, the overall damage index (ODI) is as follows:

$$ODI = \sum_{i=1}^{N} \lambda_i.(SDI_i) \tag{3.9}$$

$$\lambda_i = \frac{E_i}{\sum_{s=1}^{N} E_s} \tag{3.10}$$

where ET $=\sum_{s=1}^{N} E_s$ is the overall hysteretic energy and N is the number of stories.

For the Park & Ang damage index, nine damaged R/C buildings have been evaluated after the 1971 San Fernando earthquake in the USA and the 1978 Miyagiken-Oki earthquake in Japan by Park and Ang. The evaluations suggested the limit states shown in Table 3.3.

Table 3.3: Interpretation of Park & Ang damage index

Degree of damage	Limit State	Description of physical damage
Minor	< 0.2	Minor Cracks throughout Building Partial Crashing of Concrete in Columns
Moderate	0.2 – 0.4	Extensive Large Cracks Spalling of Concrete in Weaker Elements
Severe	0.4 – 1.0	Extensive Crashing of Concrete Disclosure of Buckled Reinforcements
Collapse	> 1.0	Total Collapse of Building

To evaluate the amount of global damage of the sample buildings in Famagusta based on the Park & Ang damage index, the states of damages suggested by Young-Ji Park, Alfredo H.-S. Ang and Yi Kwei Wen shown in Table 3.4 are used.

Table 3.4: The classification of damage values based on the Park and Ang investigation

State of Structure	Amount of Damage
Repairable (Economic)	D.I.$\leq$ 0.4
Beyond Repair (Not Economic)	$0.4 <$ D.I. ≤ 1.0
Loss of Building	D.I. > 1.0

3.4 Fragility curve

The first application of fragility curves was done for probabilistic analysis of nuclear power plants. In fact, these curves show that the probability of imposed damage under various seismic excitations. These curves depend on one of the earthquake intensity parameters, such as the PGA, peak ground velocity (PGV), or peak ground displacement (PGD), etc. Additionally, the earthquake damage levels (i.e., slight, moderate, severe, collapse, etc.) can be considered in this analysis. The analysis used for obtaining seismic response data can be nonlinear time history analysis or inelastic spectral analysis or nonlinear static analysis, etc. Figure 3.11 shows the steps of the proposed methodology in the development of fragility curves.
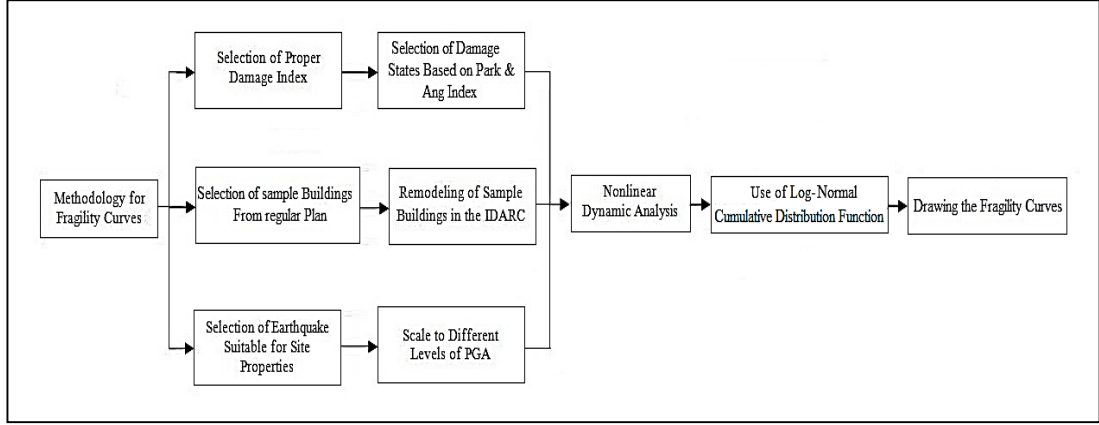
Figure 3.11: The steps of the proposed methodology used in the development of fragility curves

The probability of a structural response exceeding the limit state of a given earthquake intensity can be defined as:

$$P = P[EDP > AC] = 1 - [EDP < AC] = 1 - \emptyset \left(\frac{AC-\mu}{\sigma}\right) \qquad (3.11)$$

Where EDP is the engineering demand parameter obtained from the output of a nonlinear dynamic analysis, AC is the limit state derived from Table 3.3, Φ is the normal distribution function, and μ and σ are the mean and standard deviation of AC, respectively.

Also log-normal cumulative distribution function is selected to reduce the computational effort of seismic data and drive the fragility curves. This function is expressed as following:

$$P = F(x \mid \mu, \sigma) = \frac{1}{\sigma\sqrt{2 \cdot \pi}} \int_0^x \frac{e^{\frac{-(\ln(t)-\mu)^2}{2 \cdot \sigma^2}}}{t} \, dt \qquad (3.12)$$

3.5 Artificial neural network

ANNs are widely applied in many fields of sciences such as engineering, medical science, mathematics, etc., for linear and nonlinear regression, function approximation, classification, and other technical and scientific applications. The basic parts of a neural network are composed of activation function, architecture of network

and learning rules. The architecture of ANNs is inspired by the human brain. Indeed, neural networks are used to determine a general solution for complex and irrelevant data that lead to extracting a pattern for these types of problems. Therefore, the network is able to predict the new situations and act like an expert system.

3.5.1 Multi-Layer Perceptron (MLP) neural network

One of the most widely used neural network which has been employed for function approximation problems is MLP. A one-layer feed-forward MLP neural network consists of several neurons in input layer, optimum neurons in hidden layer and a neuron in output layer. Each layer nodes are connected to the next layer nodes with specific weight similar to synaptic weight in human neural networks. The architecture of a MLP neural network is shown in Figure 3.12.
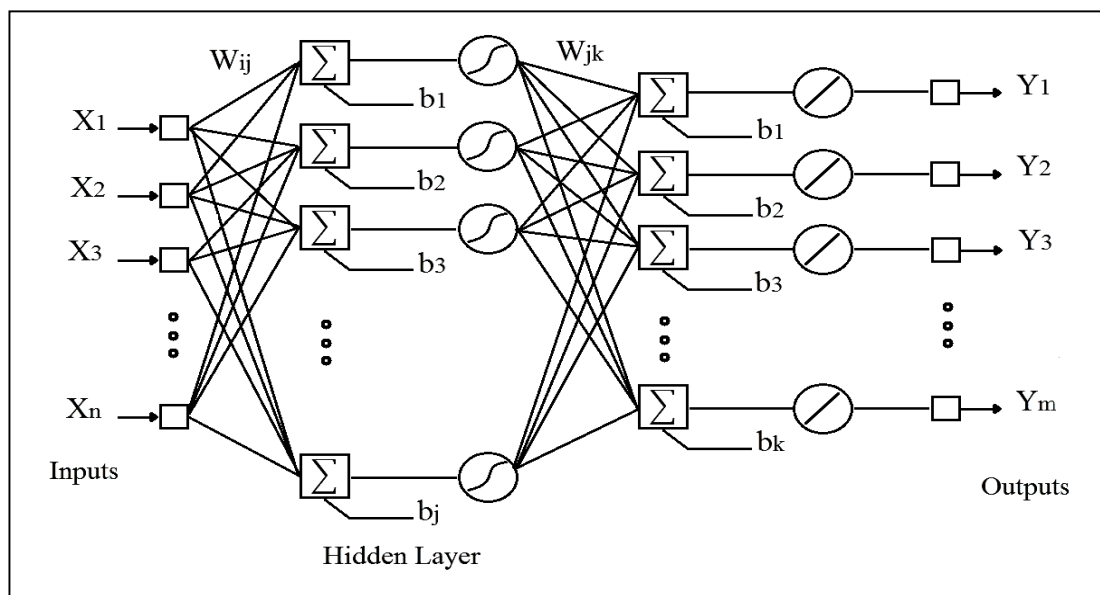
Figure 3.12: Structure of a MLP neural network model with one hidden layer feed-forward

To determine and update the weights and bias terms for learning the MLP network, a proper algorithm is needed and it is directly depended on input data. Thus, in this research the Levenberg–Marquardt back-propagation algorithm was selected and used

which has best performance for this network. It is a combination of the gradient descent and Gauss–Newton algorithm and is used as an improved algorithm which is employed in many researches. This algorithm is known as a method of damped least-squares for minimizing a function by using a numerical solution. The back propagation learning algorithm includes; propagation and weight update. Therefore, in order to carry out of this process, the neuron's outputs for each layer are calculated by using previous layer information (front-propagation). Then based on training pattern target, the gradient of the weights for each layer are computed using the difference between the target and the output of each layer (back-propagation) and finally, the weights of each layer can be updated (weight update). The amount of each neuron in the hidden layer is calculated by using equation 3.13:

$$P_j = f\left(\sum_{i=1}^{A} x_i^T \cdot w_{ij} + b_j\right) \tag{3.13}$$

where the function f is the activation function for hidden layer (calculated based on minimum test error), A is the number of input layer neuron, x_i is the ith network's input, w_{ij} is the inter-connection between i^{th} input layer neuron and j^{th} hidden layer neuron and b_j is the bias term of the jth hidden layer neuron.

Also, in the output layer, the amount of each neuron is determined as:

$$y_k = g\left(\sum_{j=1}^{B} p_j^T \cdot w_{jk} + b_k\right) \tag{3.14}$$

where g is the activation function for output layer (linear transfer function), B is the number of hidden layer neuron, p_j is the jth hidden layer neuron value of network, w_{jk} is the inter-connection between j^{th} hidden layer neuron and k^{th} output layer neuron and b_k is the bias term of kth output layer neuron. Also the Matlab code was mentioned in appendix A.

3.5.2 Support Vector Machine

SVM has been introduced for the classification and pattern recognition problems by Cortes and Vapnik (1995). It is a relatively new learning algorithm used for binary classification problems. The main difference between SVM and the other algorithms is the SVM minimizes the operational risk as an objective function instead of minimizing the classification error. The original pattern classification of this machine is to classify the linear input data using the perfect hyperplane into two classes with the largest margin in between classes. For nonlinear input data, a nonlinear mapping is used to transfer the input data from the primal space to the higher dimensional feature space and leads to find the proper hyperplane. Furthermore, SVMs have also been extended to solve multi-class problems. Also the Matlab code was mentioned in appendix B.

3.5.2.1 Linear SVM

In this section, a simple introduction of the linear SVM is presented (Burges, 1998). Considering a train sample data includes $\{(x_1,y_1),(x_2,y_2), \dots , (x_n,y_n)\}$, where each sample has the inputs ($x_i \in R^d$), and one class label ($y_i \in \{+1,-1\}$) which is shown in Figure 3.13.
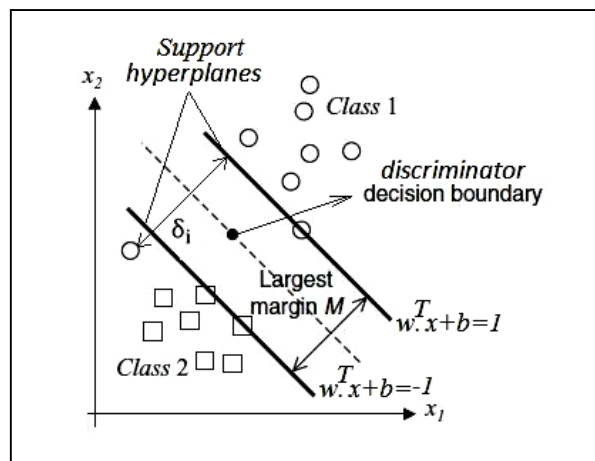
Figure 3.13: A sample of linear soft margin SVM (Cortes and Vapnik, 1995)

In the two dimensional space, the discriminator is a line in the middle of the margin between the classes. Thus, for *N*-dimension space, the discriminator is a hyperplane. Suppose the distance between the each separate data and the discriminator is equal to 1, the two support hyperplanes are considered parallel to the discriminator and the classifier function can be obtained as follows (see Figure 3.13):

$$\begin{cases} w^T \cdot x_i + b \geq 1 \,, & if \;\; y_i = 1 \quad\; i = 1, 2, \dots, n \\ w^T \cdot x_i + b \leq -1 \,, & if \;\; y_i = -1 \quad i = 1, 2, \dots, n. \end{cases} \qquad (3.15)$$

For a unique separator, the maximum margin between classes is needed. Thus, if the distance between the support hyperplanes is equal to M, using equation 3.15, the optimum margin (M) is given by:

$$M = \frac{(|b+1| - |b-1|)}{\|w\|} = \frac{2}{\|w\|} \cdot \qquad (3.16)$$

After calculating the maximum margin, the target function is defined as following:

Maximize (M) = Maximize $\frac{2}{\|w\|}$ = Minimize $\;\|w\|$ = Minimize $\frac{1}{2} \|w\|^2$ = Minimize

$\frac{1}{2} w^T.w$

Subject to (s.t.):

$$\begin{cases} w^T \cdot x_i + b \geq 1 \,, & if \;\; y_i = 1 \quad\; i = 1, 2, \dots, n \\ w^T \cdot x_i + b \leq -1 \,, & if \;\; y_i = -1 \quad i = 1, 2, \dots, n. \end{cases} \qquad (3.17)$$

Since the probability of being the separated data in nature is very low and more datasets are inseparable, therefore, the discriminator (hyperplane) is also determined based on minimum number of errors. As a result, those members belong to another class are penalized based on the distance from the boundary of its own class (δ) (see Figure 3.13). This strategy is represented as a model of soft margin SVM. For this reason, non-negative variables (δ_i) are defined and called as slack variable s.t. $\delta_i \geq 0$. Thus, the equation 3.17 is changed as following:

Minimize $\frac{1}{2} w^T \cdot w$

s.t. : $\begin{cases} w^T \cdot x_i + b \geq 1 , \\ w^T \cdot x_i + b \leq -1 , \end{cases}$ $\quad\quad \begin{array}{ll} if \ y_i = 1 & i = 1, 2, \dots , n \\ if \ y_i = -1 & i = 1, 2, \dots , n \end{array}$

$\quad\quad \delta_i \geq 0.$ $\hspace{8cm}$ (3.18)

By multiplying the both sides of first s.t. of the equation 3.18 by y, the primal

problem becomes:

Minimize $\frac{1}{2} w^T \cdot w$

s.t. : $\ y_i(w^T \cdot x_i + b) \geq 1 - \delta_i \quad\quad i = 1, 2, \dots , n$

$\quad\quad \delta_i \geq 0$ $\hspace{8cm}$ (3.19)

thus

$L_p = \frac{1}{2} w^T \cdot w - \sum_{i=1}^{n}[y_i(w^T \cdot x_i + b) - 1 + \delta_i] \quad\quad i = 1, 2, \dots , n.$ $\hspace{2cm}$ (3.20)

The primal problem is a quadratic program but it cannot be solved easily because it

is not just depended on the parameters which are related to input vectors. Therefore,

this equation changes from the primal form to dual form by using the Lagrange

method. The Lagrange factors (α_i, μ_i) must be nonnegative real coefficients and

equation 3.20 becomes:

$L_p = \frac{1}{2} w^T \cdot w + C \sum_{i=1}^{n} \delta_i - \sum_{i=1}^{n} \alpha_i [y_i(w^T \cdot x_i + b) - 1 + \delta_i] - \sum_{i=1}^{n} \mu_i \cdot \delta_i \quad,$

$\alpha_i, \mu_i \geq 0$ $\hspace{8cm}$ (3.21)

where C is penalty factor. In this case, L_p is a saddle point. Thus, at this point, the

minimum value should be taken with respect to the parameters w, b and δ and the

maximum value should be taken with respect to the Lagrange multipliers (α_i, μ_i). This

can be done by taking the partial derivative with respect to w, b and δ in order to

change the primal problem to a maximum problem as following:

$\frac{\partial L_p}{\partial w} = 0 \hspace{3cm} \rightarrow w - \sum_{i=1}^{n} \alpha_i \cdot y_i \cdot x_i = 0$ $\hspace{4cm}$ (3.22)

$\frac{\partial L_p}{\partial b} = 0 \hspace{3cm} \rightarrow \sum_{i=1}^{n} \alpha_i \cdot y_i = 0$ $\hspace{4.5cm}$ (3.23)

$\frac{\partial L_p}{\partial \delta} = 0 \hspace{3cm} \rightarrow C - \alpha_i - \mu_i = 0.$ $\hspace{4cm}$ (3.24)

By substituting equations 3.22 and 3.23 into equation 3.21, the dual problem is

obtained as follows:

$$L_D = -\frac{1}{2} \sum_{i=1}^{n} \sum_{j=1}^{n} \alpha_i \cdot \alpha_j \cdot y_i \cdot y_j \cdot x_i^T \cdot x_j + \sum_{i=1}^{n} \alpha_i. \tag{3.25}$$

Also based on the equation 3.24, the box constrains are defined as:

$$\begin{cases} \alpha_i \geq 0 \\ \mu_i \geq 0 \\ \alpha_i + \mu_i = c \end{cases} \quad \rightarrow \quad \begin{cases} 0 \leq \alpha_i \leq C \\ 0 \leq \mu_i \leq C. \end{cases} \tag{3.26}$$

In addition, by considering h_{ij} and f as the following definition:

$$h_{ij} = y_i \cdot y_j \cdot x_i^T \cdot x_j \tag{3. 27}$$

$$f = \begin{bmatrix} -1 \\ -1 \\ \cdot \\ \cdot \\ \cdot \\ -1 \end{bmatrix} \tag{3.28}$$

and substituting h_{ij} and f into equation 3.25, the dual formulation becomes:

$$L_D = -\frac{1}{2} \sum_{i=1}^{n} \sum_{j=1}^{n} \alpha_i \cdot \alpha_j \cdot h_{ij} + \sum_{i=1}^{n} \alpha_i \qquad , \alpha_i \geq 0 \tag{3.29}$$

$$L_D = -\frac{1}{2} \alpha^T \cdot H \cdot \alpha - f^T \cdot \alpha \tag{3.30}$$

where H and α are defined as:

$$H = [h_{ij}] = \begin{bmatrix} h_{11} & \cdots & h_{1n} \\ \vdots & \ddots & \vdots \\ h_{n1} & \cdots & h_{nn} \end{bmatrix} \qquad , H \in R^{n \cdot n} \tag{3.31}$$

$$\alpha = \begin{bmatrix} \alpha_1 \\ \alpha_2 \\ \cdot \\ \cdot \\ \cdot \\ \alpha_n \end{bmatrix}. \tag{3.32}$$

Therefore, the target function is expressed as follows:

Minimize $\frac{1}{2} \alpha^T \cdot H \cdot \alpha + f^T \cdot \alpha$

s.t. : $\begin{cases} w^T \cdot x_i + b \geq 1, & if \ y_i = 1 \quad i = 1, 2, \dots, n \\ w^T \cdot x_i + b \leq -1, & if \ y_i = -1 \quad i = 1, 2, \dots, n \end{cases}$

$$\sum_{i=1}^{n} \alpha_i \cdot y_i = 0$$

$$0 \le \alpha_i \le C. \tag{3.33}$$

The quadratic programming problem (equation 3.33) can be solved easily by using the quadprog function in the Matlab software and the values of α_i are calculated. Then by substituting α_i values into equation 3.22, the values of w are obtained. Also for calculating the bias term, the Karush-Kuhn-Tucker (KKT) conditions (fletcher, 1987) are necessary and sufficient for the optimization problems. Therefore, these conditions should be established in optimum point (equation 3.20). The bias value is calculated as:

$$\text{K. K. T} \rightarrow \alpha_i[y_i(w^T \cdot x_i + b) - 1 + \delta_i] = 0$$

$$\mu_i \cdot \delta_i = (C - \alpha_i) \cdot \delta_i = 0. \tag{3.34}$$

Thus based on K.K.T conditions three cases are occurred:

Case 1: None support vectors if $(\alpha_i = 0)$

$$\alpha_i = 0 \rightarrow \begin{cases} \mu_i = C \rightarrow \delta_i = 0 \\ \\ y_i(w^T \cdot x_i + b) - 1 \ge 0. \end{cases} \tag{3.35}$$

Case 2: Outliers if $(\alpha_i = C)$

$$\alpha_i = C \rightarrow \begin{cases} \mu_i = 0 \rightarrow \delta_i \ge 0 \\ \\ y_i(w^T \cdot x_i + b) - 1 + \delta_i = 0. \end{cases} \tag{3.36}$$

Case 3: Support vectors if $(0 < \alpha_i < C)$

$$0 < \alpha_i < C \rightarrow \begin{cases} 0 < \mu_i < C \rightarrow \delta_i = 0 \\ \\ y_i(w^T \cdot x_i + b) - 1 = 0. \end{cases} \tag{3.37}$$

In case 3, each x_i corresponding to α_i are support vector machines. Thus by multiplying both sides of first s.t. of the equation 3.33 by y as following:

$$w^T \cdot x_i + b = y_i \tag{3.38}$$

the amount of the bias term can be obtained as follows:

$$S = \{i \mid 0 < \alpha_i < C\}, i \in S \tag{3.39}$$

$$b = \frac{1}{|S|} \sum_{i=1}^{S} (y_i - w^T \cdot x_i) \tag{3.40}$$

and also using equation 3.22, w becomes:

$$w = \sum_{i=1}^{n} \alpha_i \cdot y_i \cdot x_i. \tag{3.41}$$

Finally, by having the amounts of w and b, the optimal hyperplane decision function can be expressed as follows:

$$y_i = Sign\ (w^T \cdot x_i + b). \tag{3.42}$$

3.5.2.2 Nonlinear SVM

For nonlinear data, the selection of optimal hyperplane for separation of data is difficult. For this case, Cortes and Vapnik (1995) used the Hilbert-Schmidt theory (Heckman, 1997) in order to transform the d-dimensional input vector x into (usually higher) an N-dimensional feature vector by using an N-dimensional vector function $\emptyset$:

$$\emptyset : R^d \to R^N$$

$$\emptyset : x \to z$$

$$z = \emptyset(x).$$

Therefore based on the SVM algorithm, the discriminator equation can be applied into z space instead of x space as following:

$$w^T \cdot x + b = 0 \quad \to w^T \cdot z + b = 0 \quad \to w^T \cdot \emptyset(x) + b = 0. \tag{3.43}$$

And according to the properties of soft margin classifier method, the dual problem is obtained as follows:

$$L_D = \frac{1}{2} \sum_{i=1}^{n} \sum_{j=1}^{n} \alpha_i \cdot \alpha_j \cdot y_i \cdot y_j \cdot \emptyset(x_i^T) \cdot \emptyset(x_j) - \sum_{i=1}^{n} \alpha_i \quad , \alpha_i \geq 0 \tag{3.44}$$

by substituting $K(x_i, x_j)$ instead of $\emptyset(x_i^T) \cdot \emptyset(x_j)$, the dual formulation becomes:

$$L_D = \frac{1}{2} \sum_{i=1}^{n} \sum_{j=1}^{n} \alpha_i \cdot \alpha_j \cdot y_i \cdot y_j \cdot K(x_i, x_j) - \sum_{i=1}^{n} \alpha_i \quad , \alpha_i \geq 0 \tag{3.45}$$

where $K(x_i, x_j)$ is kernel trick (nonlinear function), and is applied to change the linear discriminator model into nonlinear form.

Therefore, the optimal hyperplane decision function is expressed as following:

$$y = sign\left(\sum_{i=1}^{n} \alpha_i \cdot y_i \cdot K(x_i, x) + b\right). \tag{3.46}$$

3.5.2.3 Multi-class SVM (M-SVM)

The basic theory of SVM is designing the discriminator (hyperplane) with maximum margin between the two classes, while the most of classification problems are in the multi-class models (Crammer and Singer, 2001). For N classes' model, Vapnik (1995) presented a strategy to compare one class against the remaining classes and this leads to generate the N classifiers. Therefore, this method needs the solution of the N quadratic programming optimization problems and it is named 'one-versus-rest' method.

Chapter 4

ANALYSIS AND RESULTS THROUGH IDA

4.1 Primary design of models

As mentioned in section 3.1, the primary design was done in order to determine the dimensions of structural members and steel bars. For this purpose, 1975 Turkish design code (1975) and ACI 318-83 (1983) were used as seismic code and the reinforced concrete members design code, respectively via SAP2000. The seismic factor and details of each building are given as follows:

$$C = C_0 \cdot K \cdot I \cdot S \geq \frac{C_0}{2} \tag{4.1}$$

$$S = \frac{1.0}{|0.8 + T - T_0|} \leq 1.0 \tag{4.2}$$

$$T = 0.09 \frac{H}{\sqrt{D}} \quad , \quad 0.07 \, N \leq T \leq 0.1 \, N \tag{4.3}$$

$C_0 = 0.1$ for seismic zone I

$K = 0.6$ for reinforce concrete moment frame

$I = 1.0$ for residential building , $T_0 = 0.8$ for soil type IV

Table 4.1: The fundamental period, spectral factor and seismic factor

Story No.	T	S	C
4	0.385	2.597	0.06
6	0.544	1.838	0.06
8	0.60	1.67	0.06

Table 4.1 shows the fundamental period, spectral factor and seismic factor for each sample building. The properties of buildings are shown in Table 4.2. Furthermore, the beam and column section details for each sample building are tabulated in Table 4.3 and 4.4, respectively.

Table 4.2: The sample buildings properties

No.	Direction	First Mode Period (s)	No. of Stories
1	X	0.57	4
2	Y	0.54	
3	X	0.75	6
4	Y	0.68	
5	X	0.97	8
6	Y	0.80	

Table 4.3: The beam sections for each sample building

Story level	Beam section		
	4 story	**6 story**	**8 story**
1, 2	40x15cm 8Φ12	50x15cm 10 Φ 12	70x15cm 12 Φ 14
3, 4	35x15cm 6 Φ 12	40x15cm 8 Φ 12	60x15cm 10 Φ 14
5, 6		30x15cm 6 Φ 12	50x15cm 8 Φ 14
7, 8			40x15cm 6 Φ 14

Table 4.4: The column sections for each sample building

Story level	Column Section		
	4 story	**6 story**	**8 story**
1, 2	25x40cm 10 Φ 12	25x50cm 12 Φ 16	25x70cm 16 Φ 20
3, 4	25x35cm 10 Φ 10	25x40cm 12 Φ 14	25x60cm 14 Φ 14
5, 6		25x30cm 10 Φ 12	25x50cm 12 Φ 14
7, 8			25x40cm 12 Φ 12

Because the amount of S from Table 4.1 for each sample building were obtained more than one, therefore this parameter value considered equal to 1. After the design step, structural models are analyzed via IDARC-2D software, i.e. nonlinear time history analysis process is applied after defining the hysteresis parameters. In next section, these parameters are explained.

4.2 Hysteretic rule

One of the main aspects for modeling the nonlinear behavior of structural elements is hysteretic model type. The IDARC software contains two hysteretic types with complex models including; the polygonal and smooth hysteretic models.

The performance of the Polygonal Hysteretic Model (PHM) is based on piecewise linear behavior. The PHM contains initial or elastic behavior, yielding, cracking, stiffness and strength degrading stages, crack and gap closures and it can be defined by four models as:

1- Trilinear Model

2- Bilinear Model

3- Vertex Oriented Model

4- Nonlinear Elastic-Cyclic Model (Sivaselvan and Reinhorn, 1999).

The Smooth Hysteretic Model (SHM) involves continuous change of stiffness due to yielding, but sharp changes due to unloading and declining behavior.

A general model of smooth hysteretic was introduced by Sivaselvan and Reinhorn (1999) which is acts based on internal parameters with stiffness and strength decline and pinching properties (MCEER-09-0006, 2009).

In this study, a PHM was used to define the structural members hysteretic based on Trilinear Model.

4.2.1 Trilinear model

For the first time this model was proposed by Park et al. (1987) and applied in original release of IDARC. The trilinear model contains stiffness decline, strength decline, slip-lock, non-symmetric response and a trilinear monotonic envelope. This acts by changing from one linear phase to another and is dependent on the deformation history. The typical of trilinear hysteretic curves is shown in Figure 4.1.
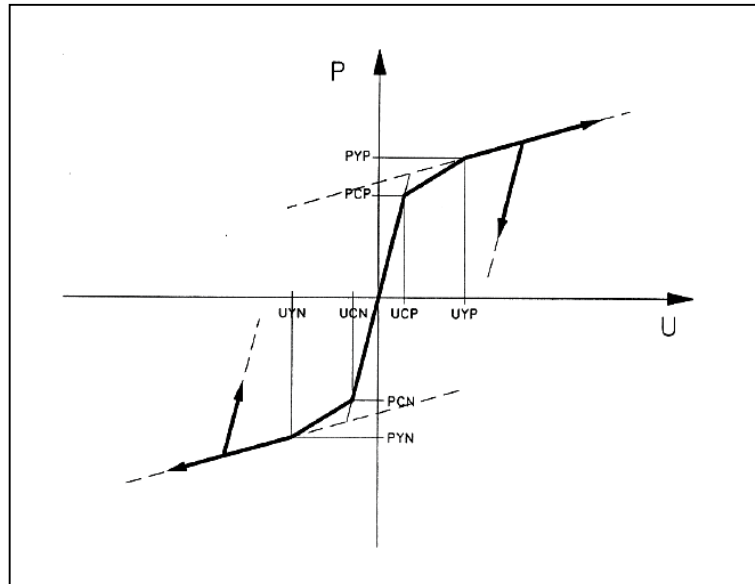
Figure 4.1: A typical trilinear hysteretic model

In IDARC software, three main parameters should be defined for hysteretic model. These parameters consist of stiffness degradation, strength degradation and pinching. Since the hysteretic behavior of PHMs is starting from a yielding moment, so the paths of loading and unloading between yielding and cracking is the same.

4.2.2 Stiffness degradation parameter

The stiffness decline is expressed by using primary slope in hysteretic cyclic model and it occurs based on geometric effects. Also by increasing the ductility, the elastic stiffness will be decreased. Park et al., (1987) presented that the stiffness decline parameter can be modeled using the pivot rule. Indeed, this factor is determined by dividing the amount of moment in pivot point to yield point which is expressing the area enclosed by the hysteresis loops. In IDARC software, this parameter is shown by α index. The schematic representation of this parameter is shown in Figure 4.2.
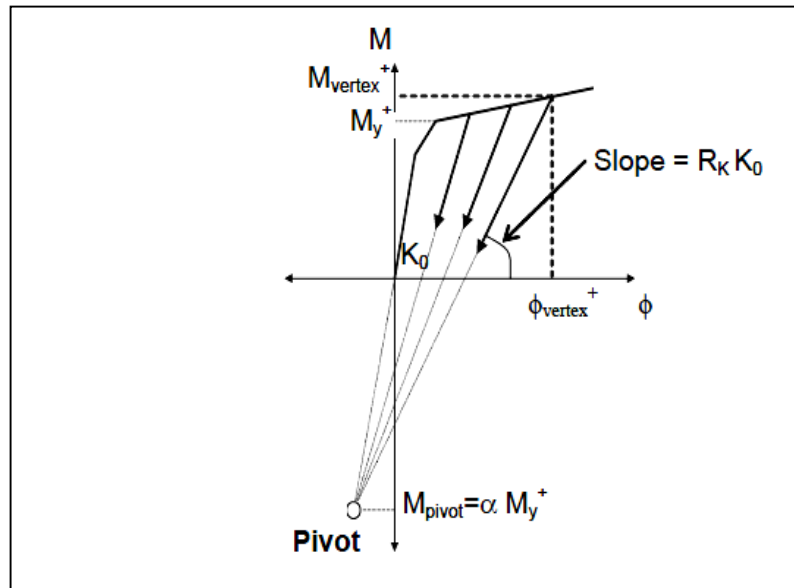
Figure 4.2: The sketch of stiffness decline in the PHM

4.2.3 Strength degradation parameter

The strength decline is expressed by using the reduced capacity in the backbone curve. Indeed this parameter shows the stability of response and also the rate of achieving failure. In IDARC software, this parameter is defined by using two factors including; β_1 which shows that the rate of strength decline based on ductility and β_2 which represents this rate based on hysteretic energy dissipation. The schematic representation of this parameter is shown in Figure 4.3.
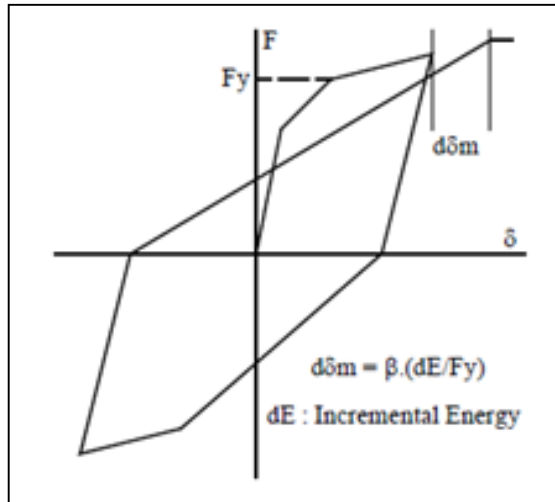
Figure 4.3: The sketch of strength decline in the PHM

4.2.4 Pinching parameter

The pinching factor is expressed using the crack closure, bond slip, bolt slip, etc. Indeed, it is modeled by considering the target point for the loading branch to be the crack closing point. In IDARC software, this parameter is shown by γ index. The schematic representation of pinching factor is shown in Figure 4.4.
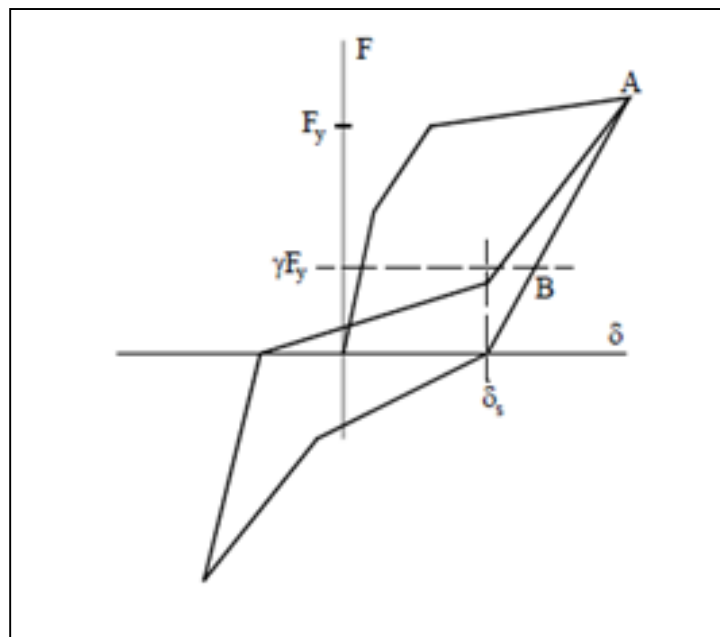
Figure 4.4: The sketch of pinching factor in the PHM

In IDARC software, four levels were considered for definition of these indices that include; (a) Severe degrading (b) Moderate degrading, (c) Mild degrading and (d) No degrading (Default).The range of these indices are shown in Table 4.5.

Table 4.5: The stiffness, strength and pinching range for severe, moderate, mild and no degrading cases (MCEER-09-0006, 2009)

Effect	α Stiffness parameter	β_1 Strength parameter (ductility based)	β_2 Strength parameter (energy based)	γ Slip or crack parameter
Severe	4.0	0.60	0.6	0.05
Moderate	10.0	0.30	0.15	0.25
Mild	15.0	0.15	0.08	0.40
No degrading	200.0	0.01	0.01	1.00

4.2.5 Determination of hysteretic indices

In order to evaluate and determine the hysteretic behavior of structural members, the IDARC indices should be calibrated using the experimental results under cyclic load test. Since that the structural members used in these building involve the rectangular cross section with aspect ratio (width over height) around two, therefore the obtained results of experimental test were used which were done by National Science Foundation Pacific Earthquake Engineering Research Center (PEER, 2013) for 165 spiral and 253 rectangular sections of reinforced concrete columns. Among these samples, a rectangular sample which was tested by Aboutaha and Machado (1999) was selected because the dimension and bar percentage of tested sample were

similar to sections used in this research and also the strong moment of inertia was placed in perpendicular direction of earthquake load. The informations of this tested sample are shown in Table 4.6.

Table 4.6: The property of tested sample (Aboutaha and Machado (1999))

Concrete section detail	Parameter	Value
Geometry	f'_c (Mpa)	21.9
	Axial Load (KN)	0.0
	Section width, B (mm)	914.4
	Section height, H (mm)	547.2
	Column length, L (mm)	1219.2
	Cross Area (mm^2)	418064
Longitudinal Reinforcement Data	Bar Diameter (mm)	25
	Total # Bars	16
	Clear Cover (mm)	38
	Reinforce Ratio	0.0188
	Yield stress, f_y (Mpa)	434
	Ultimate stress, f_{su} (Mpa)	690
Transverse Reinforcement Data	Bar Diameter (mm)	9.53
	Bar Spacing (mm)	406.4
	Total # Hoop sets	3
	Yield stress, f_y (Mpa)	400
	Ultimate stress, f_{su} (Mpa)	627

Based on Table 4.6, this section was modeled in IDARC software and imposed under Quasi-Static Cyclic Analysis. The pattern load was considered same as the experimental load which was used in real test and is shown in Figure 4.5. Then the hysteretic energy curves were derived based on each hysteretic modeling rule and finally they were compared with the obtained curve from experimental test. Figure 4.6 shows the comparison of results for severe, moderate, mild and no degrading (default) cases.
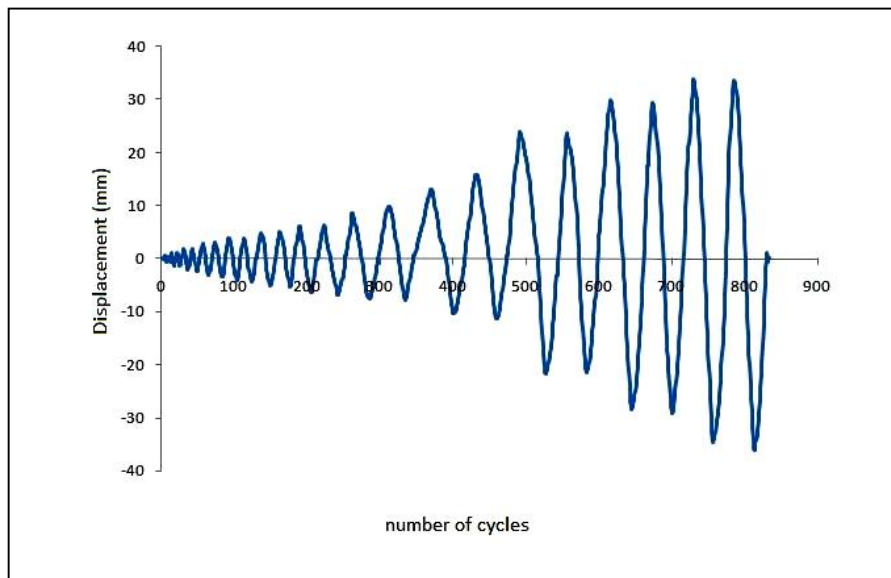
Figure 4.5: The pattern load of full-scale tested sample column (Aboutaha and Machado (1999))
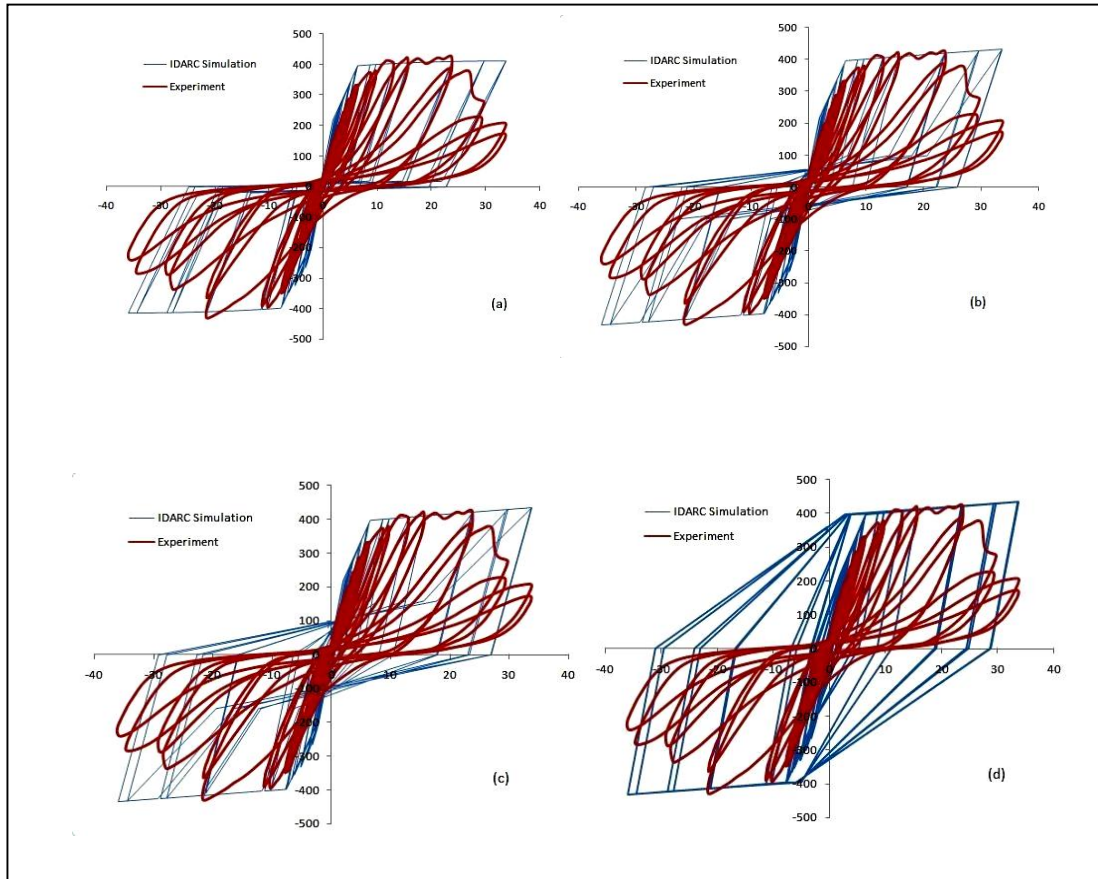
Figure 4.6: Comparison of tested sample versus computed response for (a) severe degrading (b) moderate degrading, (c) mild degrading and (d) no degrading (default) (Aboutaha and Machado (1999))

Based on compared curves, the best fitting between tested samples and computed responses was obtained in moderate degrading state but the pinching effect should become stronger. Therefore the amounts of β_1 and γ factors were changed to 0.3 and 0.1, respectively. This fitting of response hysteretic is shown in Figure 4.7.
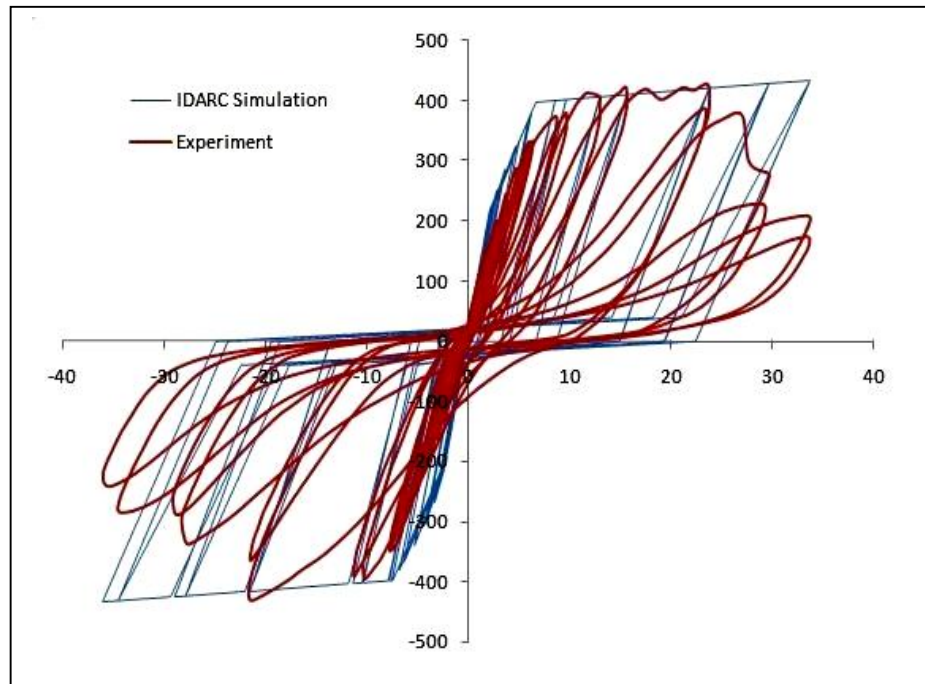
Figure 4.7: Comparison of tested sample versus computed response with modified strength and pinching parameters (Aboutaha and Machado (1999))

For the remaining columns which their strong moment of inertia were placed in parallel direction with earthquake load, another sample was selected from tests done by Aboutaha et al. (1999). The informations of this sample are shown in Table 4.7.

Table 4.7: The property of tested sample (Aboutaha and Machado (1999))

Concrete section detail	Parameter	Value
Geometry	f'_c (Mpa)	26.9
	Axial Load (KN)	646
	Section width, B (mm)	400
	Section height, H (mm)	600
	Column length, L (mm)	1784
	Cross Area (mm^2)	240000
Longitudinal Reinforcement Data	Bar Diameter (mm)	24
	Total # Bars	10
	Clear Cover (mm)	24
	Reinforce Ratio	0.0188
	Yield stress, f_y (Mpa)	434
	Ultimate stress, f_{su} (Mpa)	690
Transverse Reinforcement Data	Bar Diameter (mm)	12
	Bar Spacing (mm)	80
	Total # Hoop sets	3
	Yield stress, f_y (Mpa)	400
	Ultimate stress, f_{su} (Mpa)	627

For this test, the pattern load is shown in Figure 4.8. The hysteretic energy curves were derived based on each hysteretic modeling rule and finally they were compared with the obtained curve from experimental test. Figure 4.9 shows that the comparing results for severe, moderate, mild and no degrading (default) cases.
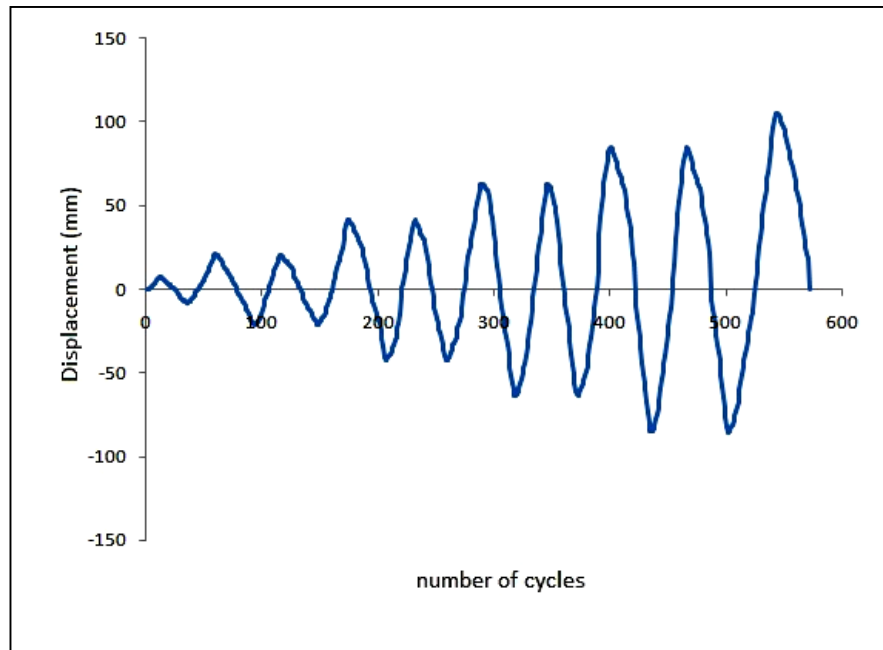
Figure 4.8: The pattern load of full-scale tested sample column (Aboutaha and Machado (1999))
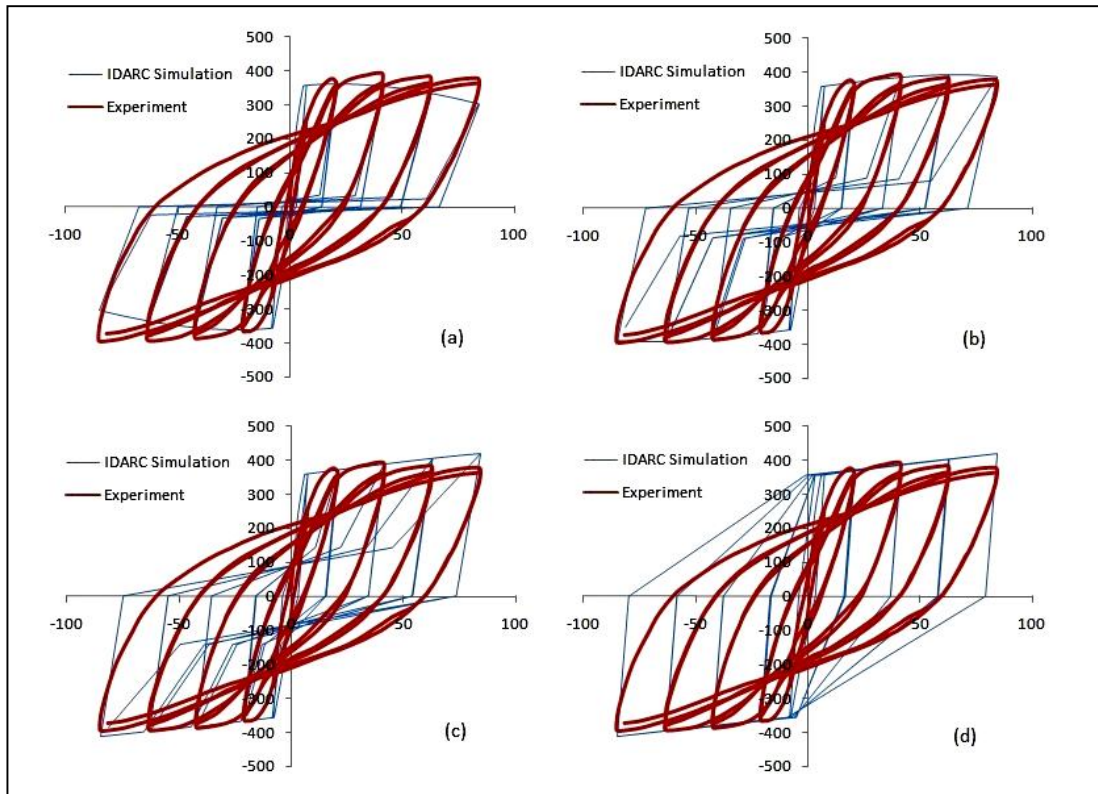
Figure 4.9: Comparison of tested sample versus computed response for (a) severe degrading (b) moderate degrading, (c) mild degrading and (d) no degrading (default) (Aboutaha and Machado (1999))

Based on compared curves, the nearest fitting between tested sample and computed responses was obtained between mild and no degrading states. Therefore the amounts of α, β_1, β_2 and γ factors were changed to 4.0, 0.3, 0.15 and 0.8, respectively. This fitting of hysteretic response is shown in Figure 4.10.
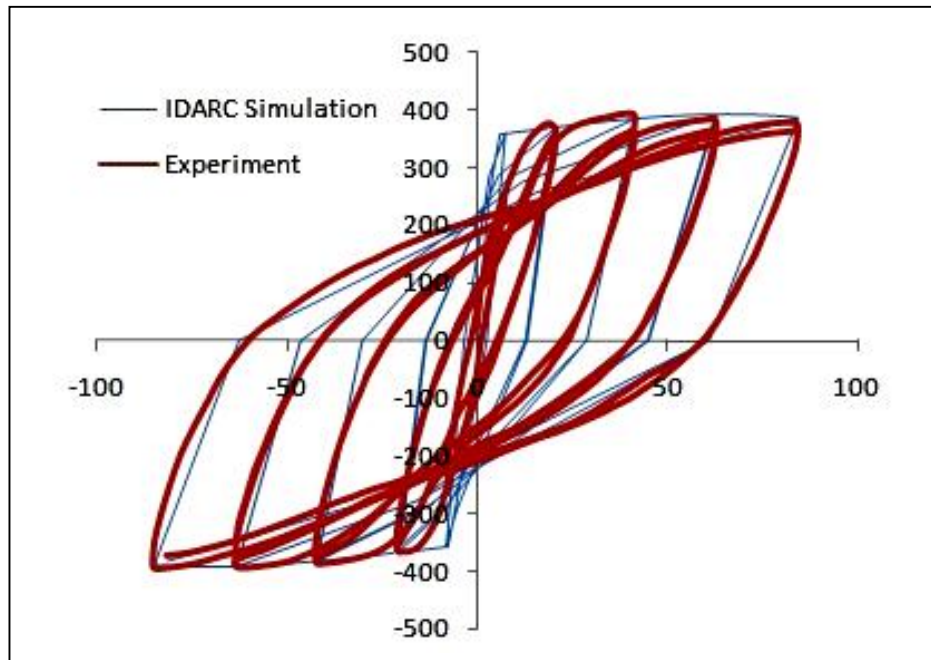
Figure 4.10: Comparison of tested sample versus computed response with modified stiffness, strength and pinching parameters (Aboutaha and Machado (1999))

4.3 3D model

Based on information mentioned in Table 4.2, all sample buildings in X direction are weaker than Y direction. Therefore each sample was remodeled and excited only in X direction via IDARC-2D software. The steps for development of fragility curves were mentioned in Figure 3.11. The obtained fragility curves for each sample buildings are shown in Figures 4.11-4.13, respectively. Also the log-normal cumulative distribution function parameters that were used for drawing the fragility curves are tabulated in Table 4.8.
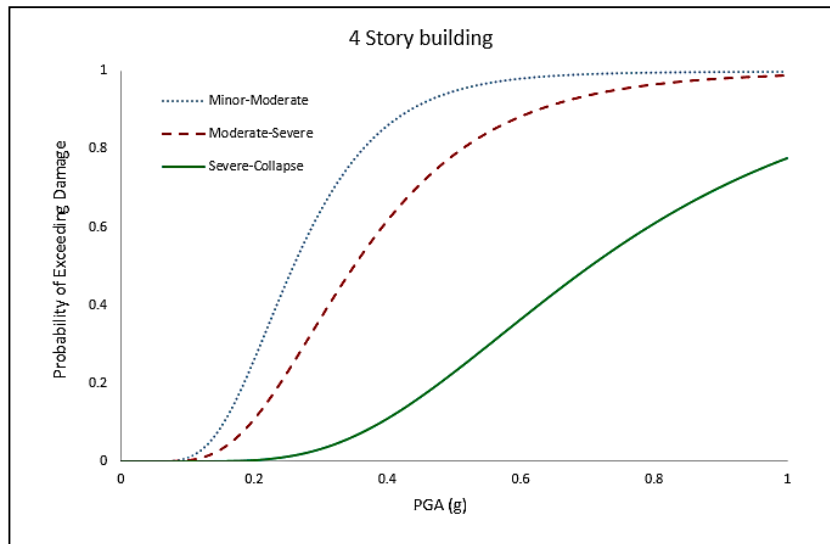
Figure 4.11: The fragility curves for four story building
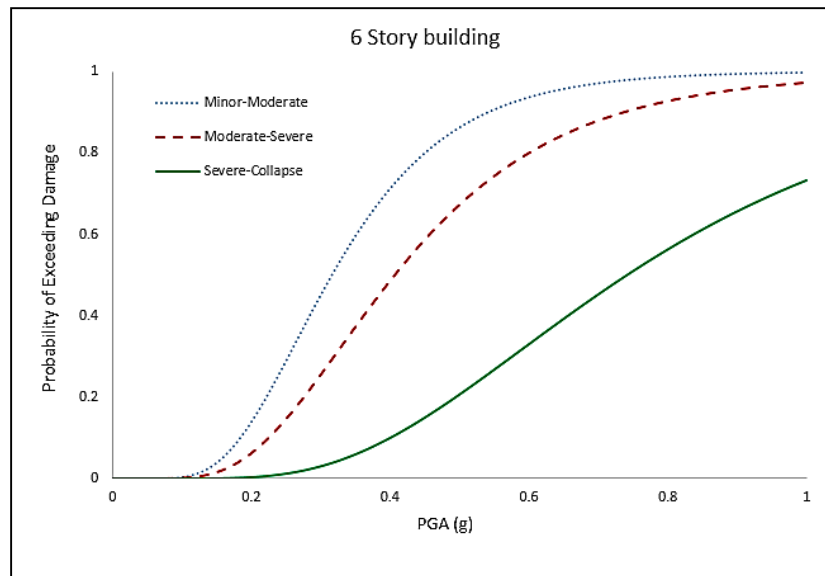
Figure 4.12: The fragility curves for six story building

54
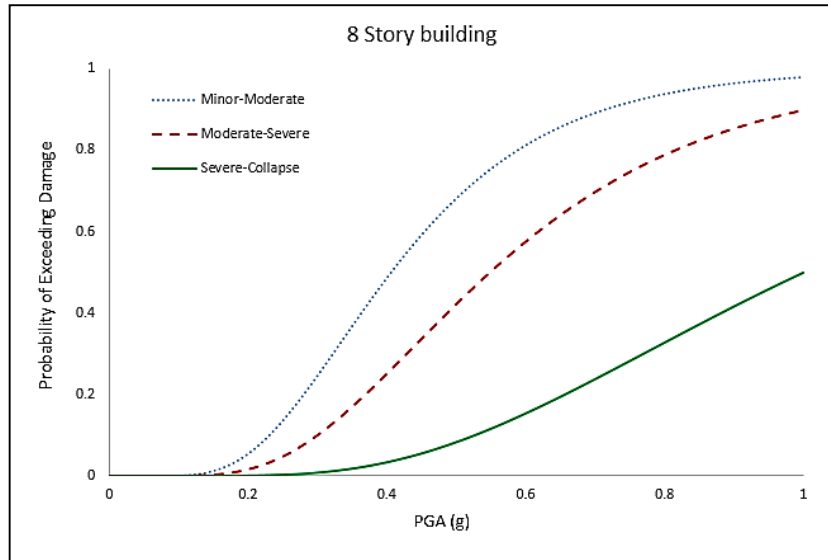
Figure 4.13: The fragility curves for eight story building

Table 4.8: The used mean and standard deviation values for drawing the fragility curves

	Level	Minor-Moderate	Moderate-Sever	Sever-Collapse
Mean	4	0.28	0.39	0.78
	6	0.35	0.45	0.83
	8	0.45	0.61	1.13
Standard Deviation	4	0.64	0.67	0.89
	6	0.66	0.69	0.91
	8	0.71	0.79	1.07

As an example the nonlinear dynamic response of each sample building under Duzce-Turkey record which is scaled to 0.5g was considered and evaluated. Figure 4.14 and 4.15 show the record and top displacement of each sample building, respectively.
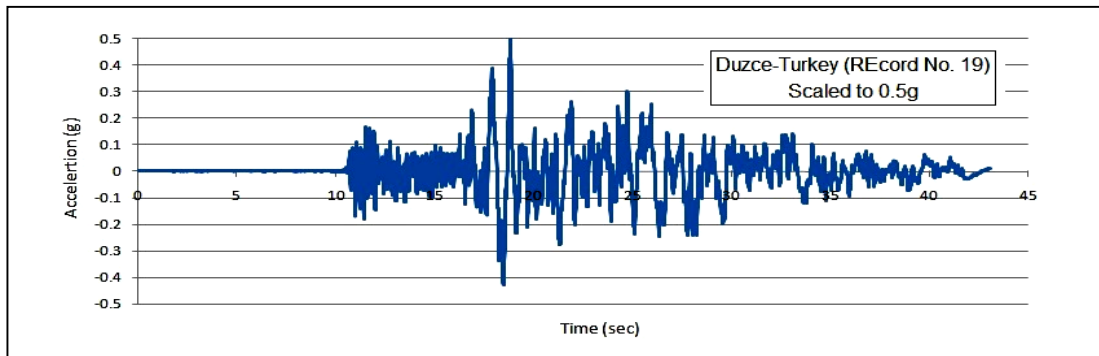
Figure 4.14: The Duzce-Turkey ground motion record scaled by 0.5g
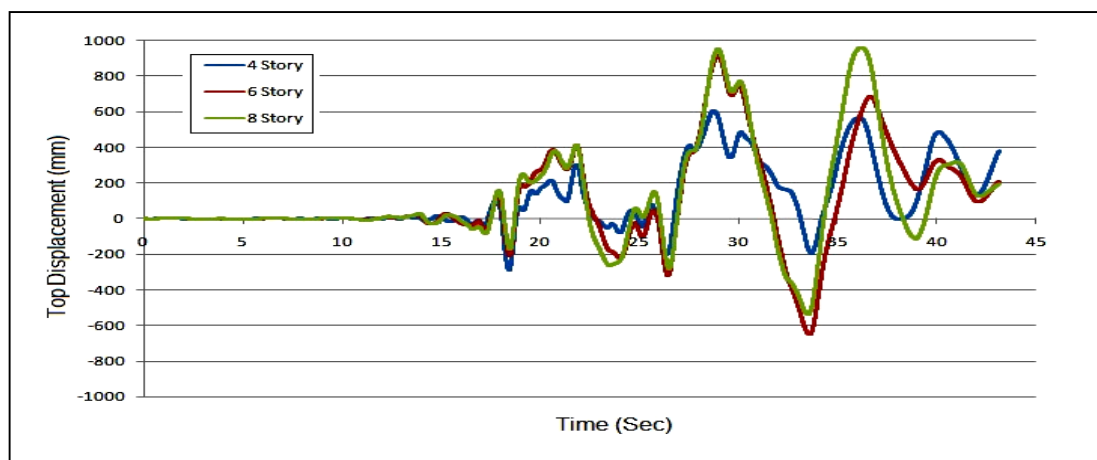
Figure 4.15: The top displacement for four, six and eight story buildings

The damage process of beams and columns from external frame and middle span for each sample buildings are shown in Figures 4.16-4.18, respectively. The results show that the maximum and minimum damage for columns were observed in the first story and the last story, respectively. Whereas this process was revised for beams, it means that the maximum and minimum damages were observed in last story and first story, respectively.
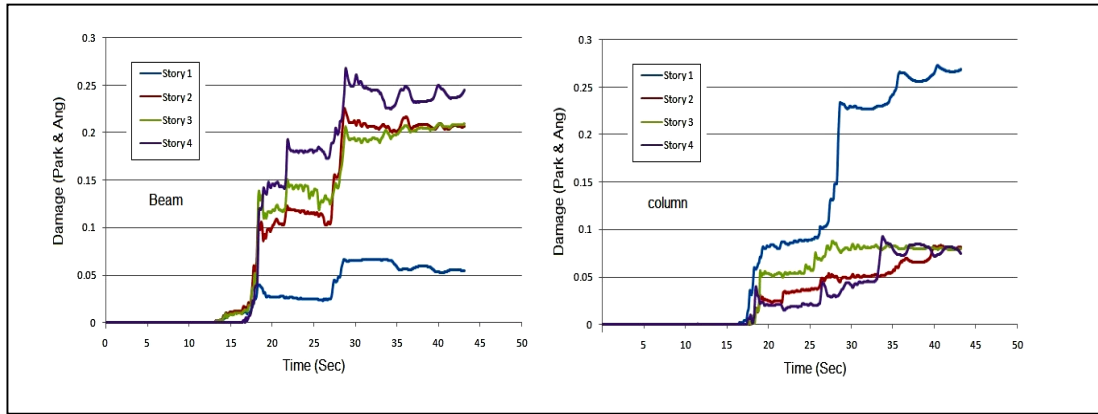
Figure 4.16: The process of beams and columns damage for four story building
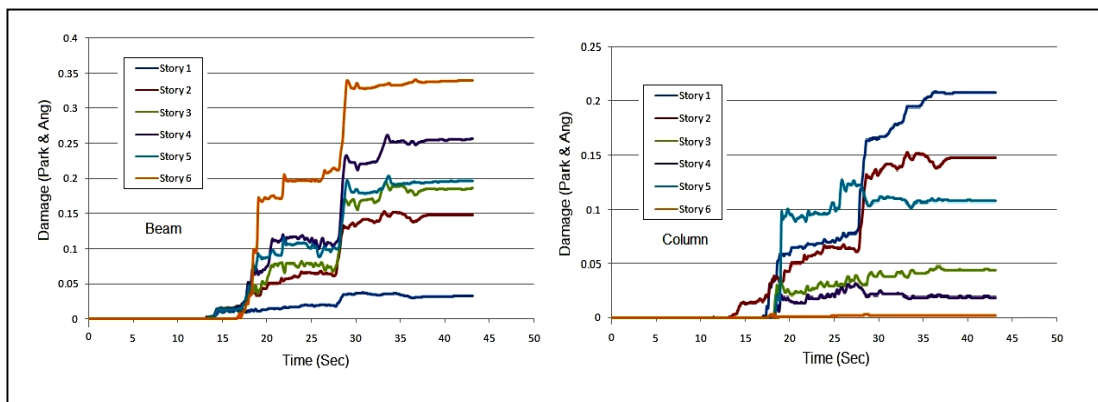
Figure 4.17: The process of beams and columns damage for six story building
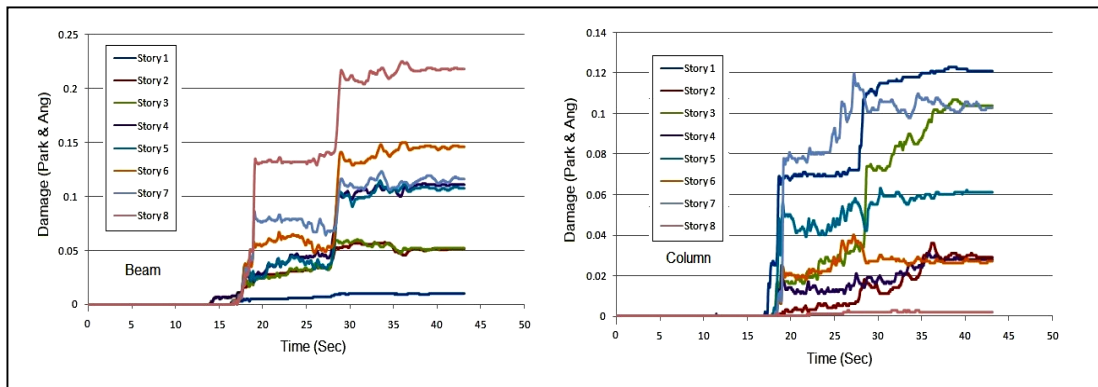
Figure 4.18: The process of beams and columns damage for eight story building

Figure 4.19 shows the maximum story displacement and story shear force for each sample buildings. The results show that the maximum displacement occurred in top story while the maximum shear force was observed in the first story.
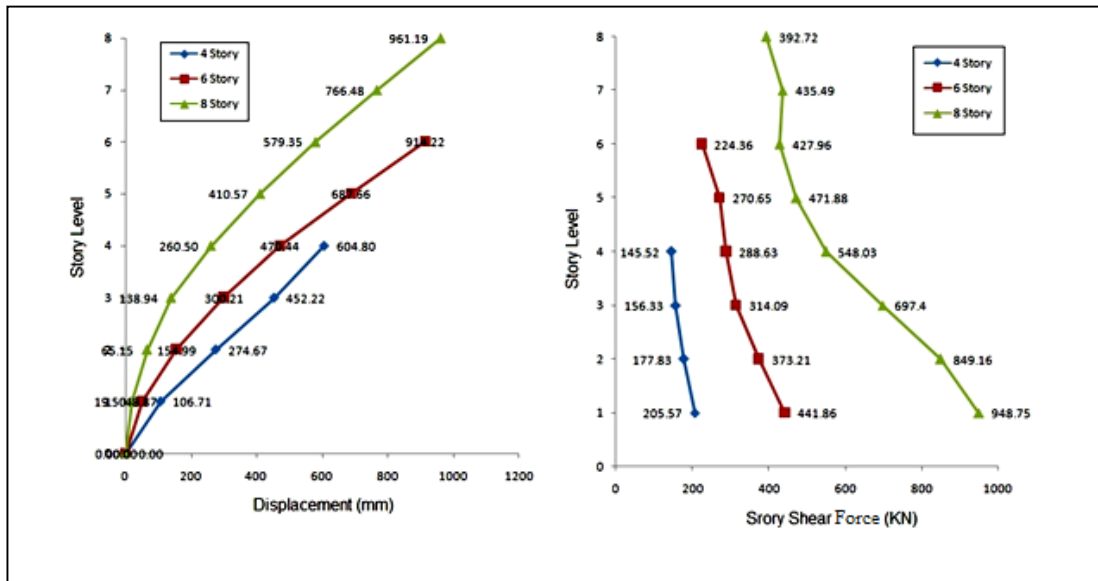
Figure 4.19: the maximum story displacement and story shear for four, six and eight story buildings

Moreover, the modal participation factor and relative modal weight for each sample buildings are shown in Figures 4.20 and 4.21, respectively. The results show that the most participation was occurred for the first mode.
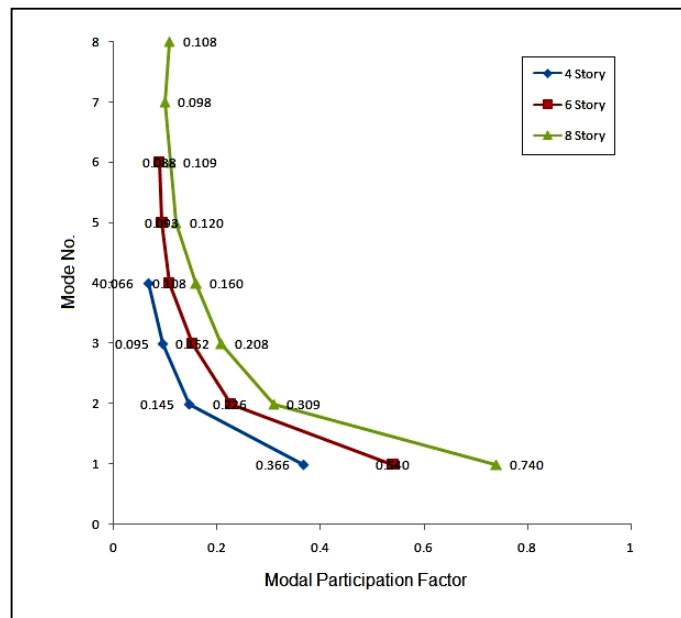
Figure 4.20: The modal participation factor for each level and each sample buildings
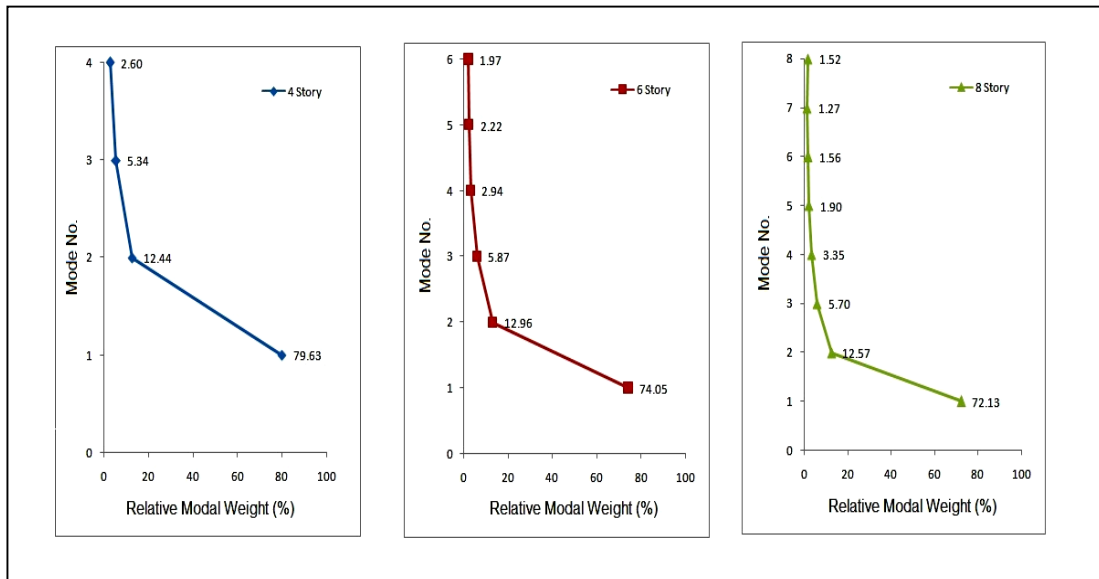
Figure 4.21: The relative modal weight (%) for four, six and eight story buildings

Moreover, the plastic hinge behavior for a beam and each type of column were evaluated. The beam hinge was selected from the exterior frame of each building, in the middle span, left side and in first level. Also for columns, in same frame and level, one of them in corner and another one in middle span were considered. Figures 4.22, 4.23 and 4.24 show the plastic hinge behavior of beam, corner column and middle column for four story building, respectively. The amount of obtained damage for beam, corner column and middle column were calculated as 0.54, 0.78 and 0.5, respectively.
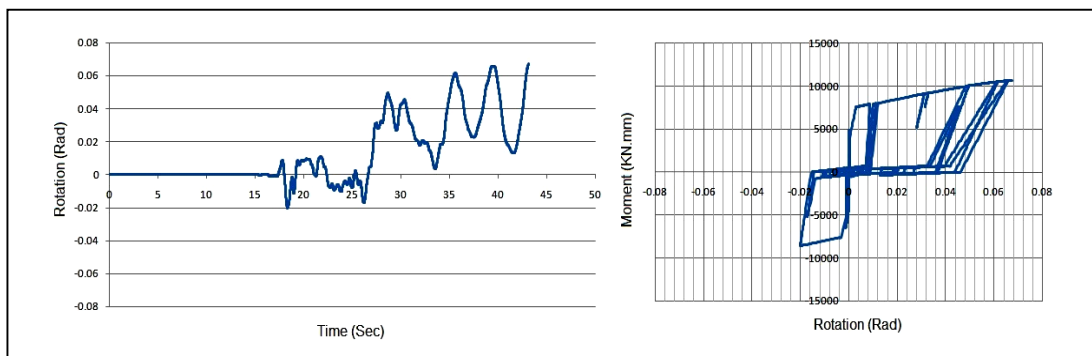
Figure 4.22: The plastic hinge behavior of beam for four story building

59
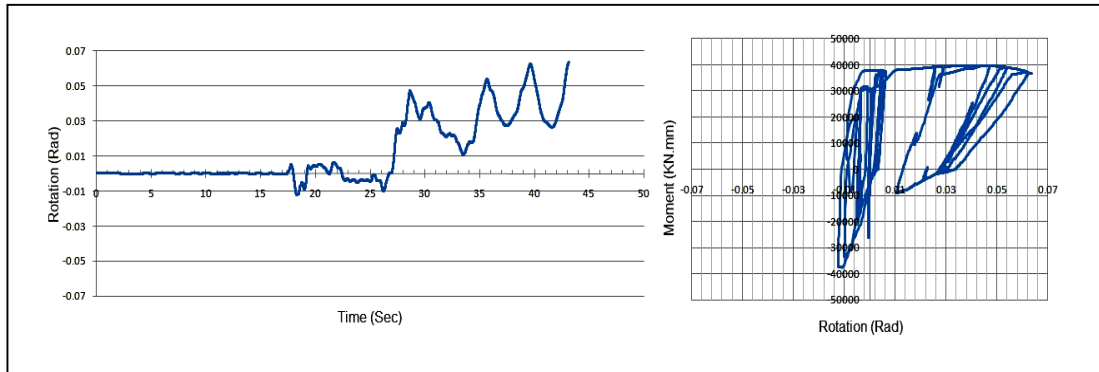
Figure 4.23: The plastic hinge behavior of corner column for four story building
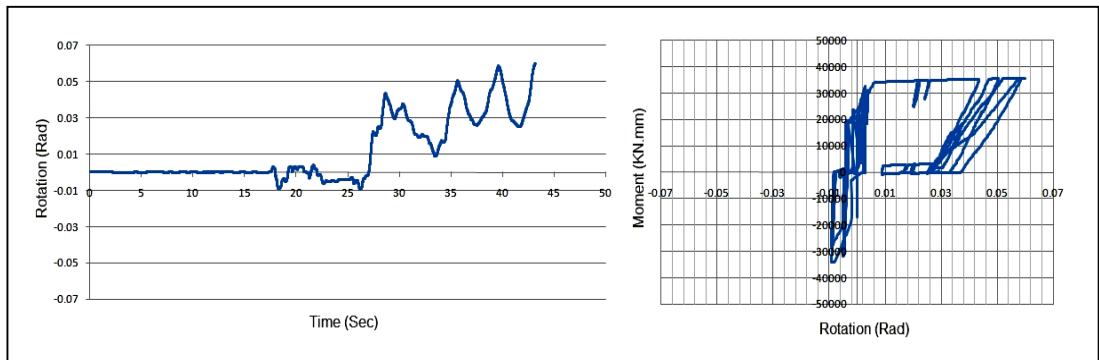
Figure 4.24: The plastic hinge behavior of middle column for four story building

Figures 4.25, 4.26 and 4.27 show the plastic hinge behavior of beam, corner column and middle column for six story building, respectively. The amount of obtained damage for beam, corner column and middle column were calculated as 0.2, 0.17 and 0.22, respectively.
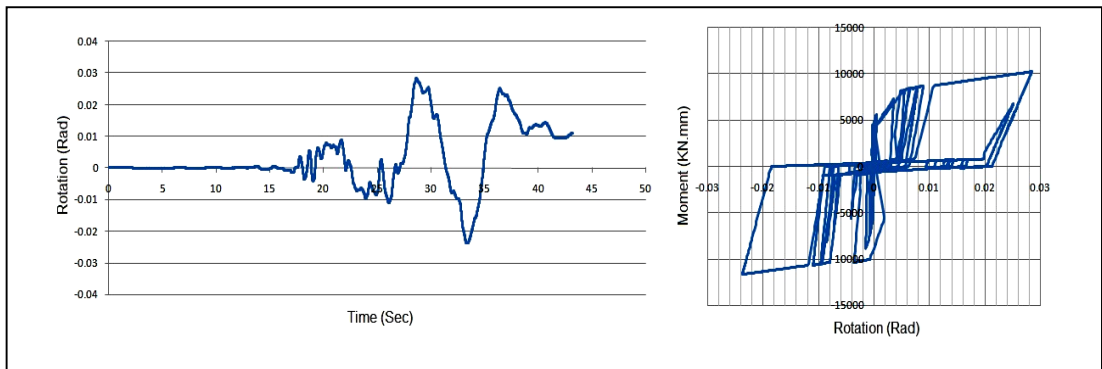
Figure 4.25: The plastic hinge behavior of beam for six story building
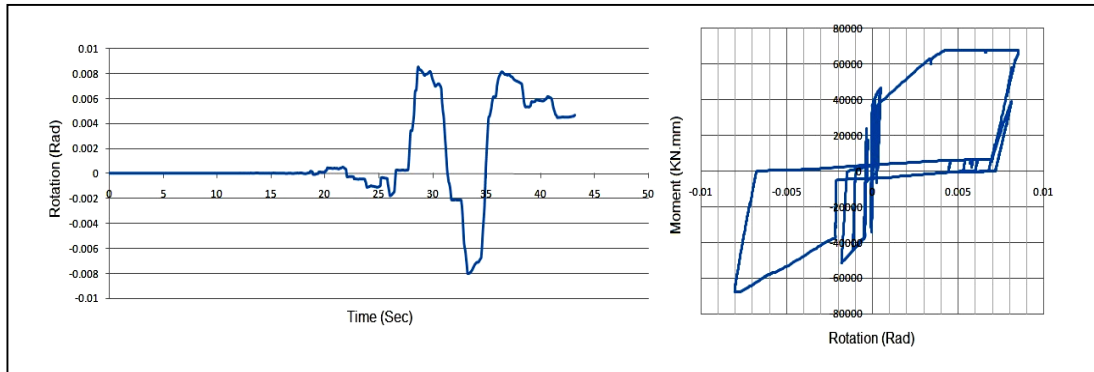
Figure 4.26: The plastic hinge behavior of corner column for six story building
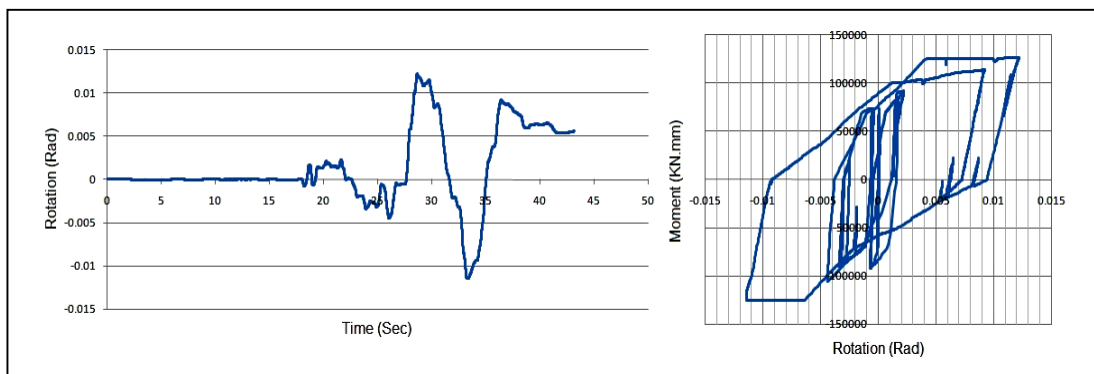
Figure 4.27: The plastic hinge behavior of middle column for six story building

Figures 4.28, 4.29 and 4.30 show the plastic hinge behavior of beam, corner column and middle column for eight story building, respectively. The amount of obtained damage for beam, corner column and middle column were calculated as 0.05, 0.07 and 0.13, respectively.
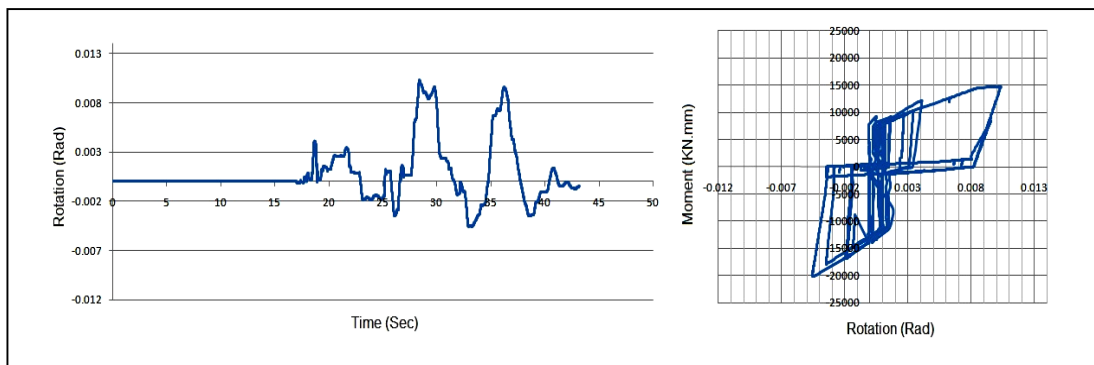
Figure 4.28: The plastic hinge behavior of beam for eight story building
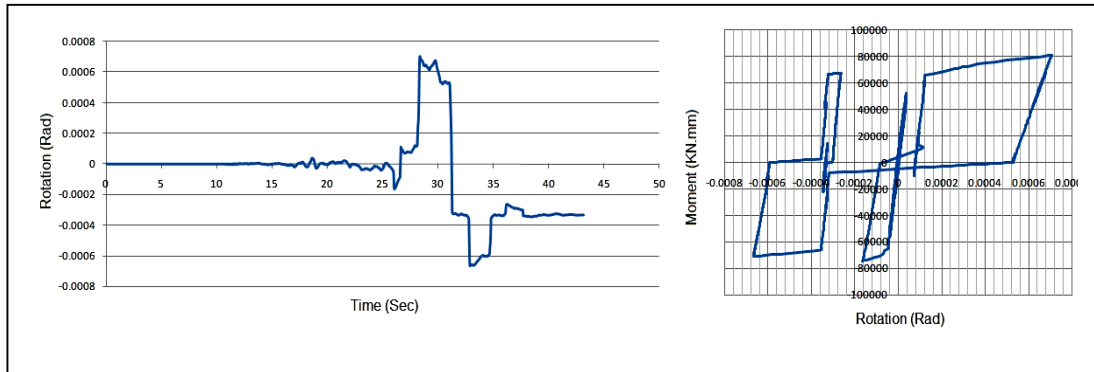
Figure 4.29: The plastic hinge behavior of corner column for eight story building
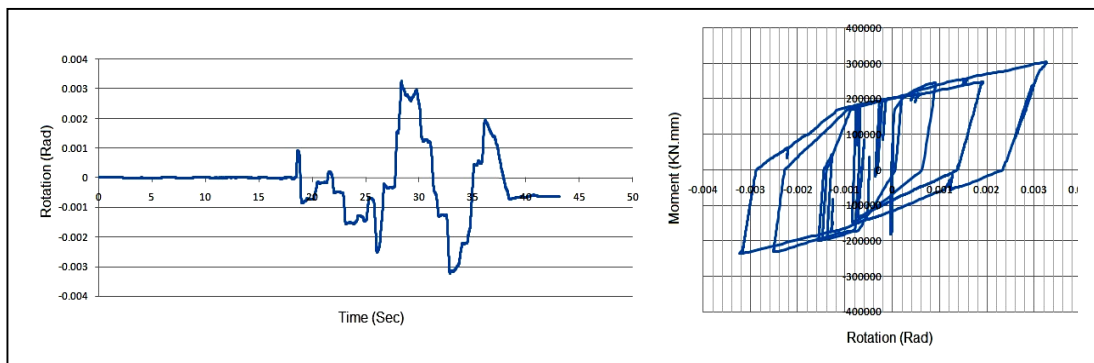
Figure 4.30: The plastic hinge behavior of middle column for eight story building

In order to compare the damage level criteria between FEMA 356 (2000) (Table 3.2) and obtained results, the IDA curves were drown based on maximum inter-story drift ratio then, the amount of damage criteria for each buildings was calculated. These curves are shown in Figures 4.31, 4.32 and 4.33 for four, six and eight story buildings, respectively. Based on obtained curves, two levels of damage, IO and collapse prevention (CP) are determined. The IO and CP levels were identified at the end of initial slope and close to zero slope in mean curve, respectively. Therefore, the damage criteria for IO level was obtained as same as criteria that was suggested by FEMA 356 (2000) equal to 1%, but for CP level, the damage criteria was obtained one percent more than suggested criteria by FEMA 356 (2000) equal to 5%. Also it should be considered that some of the records were not completely flattened because their energy was very low and they didn`t have any effect on damage levels.
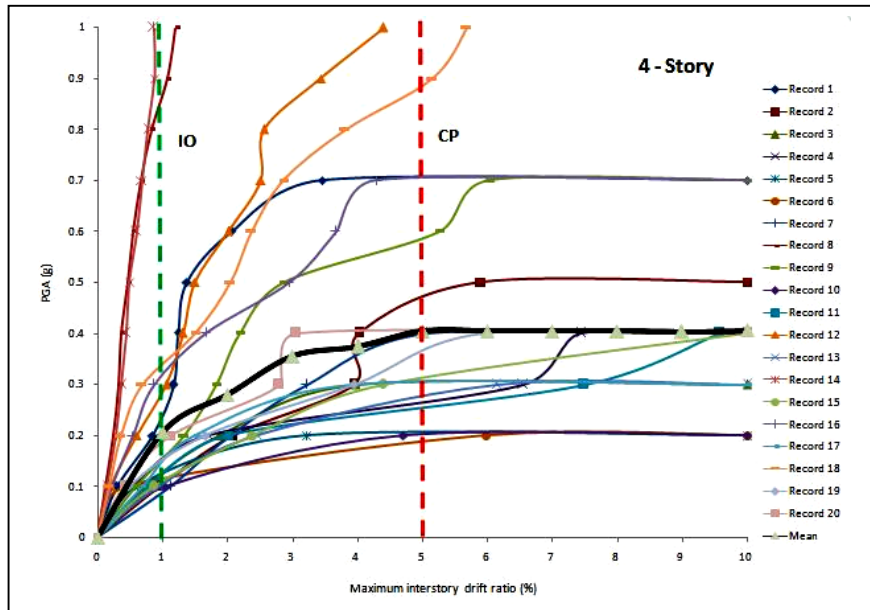
Figure 4.31: IDA curves and limit-state capacities for four story building
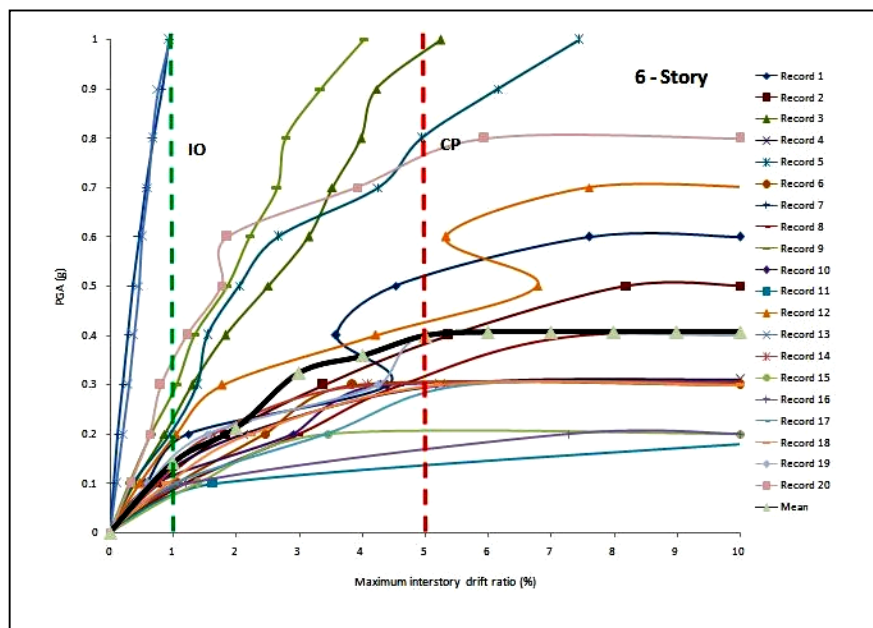
Figure 4.32: IDA curves and limit-state capacities for six story building
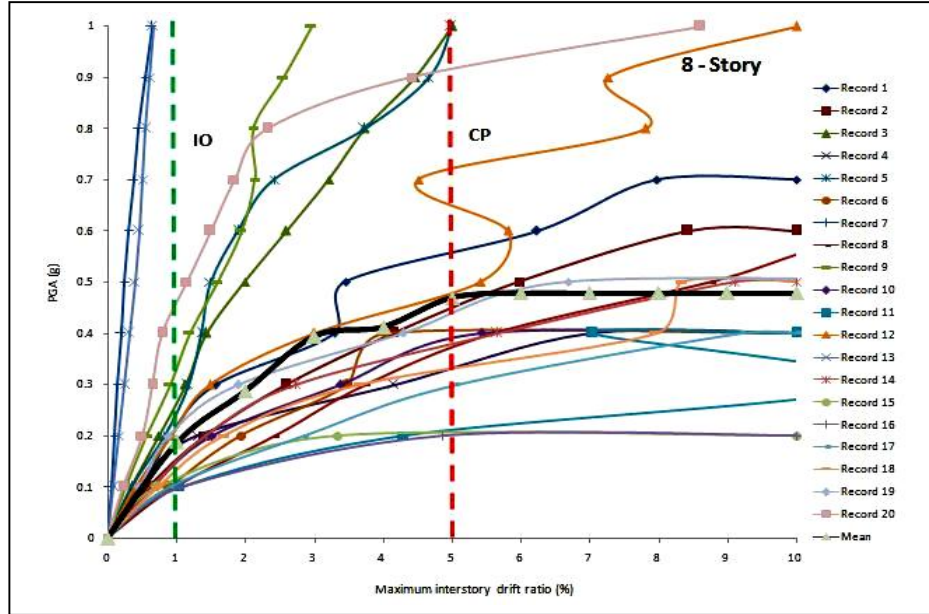
Figure 4.33: IDA curves and limit-state capacities for eight story building

4.4 P-Delta Effect

The P-delta arises due to the relative inter-story drifts and leads to add the overturning moments in the vertical elements. These moments are essentially produced based on gravity loads and add a geometric stiffness matrix to the element stiffness matrix (Wilson and Habibullah, 1987).

By considering a column between two story levels, which is shown in Figure 4.34 and calculating the moments for lower story level as following:

$$P_i \cdot h_i - (M_i + M_{i-1}) - N_i(U_i + U_{i-1}) = 0.0 \tag{4.4}$$

Deriving the additional gravity load shears at i^{th} story level, the P_i is given by:

$$P_i = \frac{N_i(U_i - U_{i-1})}{h_i} - \frac{N_{i+1}(U_{i+1} - U_i)}{h_{i+1}} \tag{4.5}$$

Therefore, for each component, the above equation can be written as:

$$\{P^*\} = [K_G] \cdot \{\Delta_u\} \tag{4.6}$$

where P_i is additional gravity load shear, h_i is the ith story height, h_{i+1} is the $(i+1)^{th}$ story height, M_{i-1} is lower moment of ith story level, M_i is upper moment of ith story level, U_{i-1} is lower displacement of ith story level, U_i is upper displacement

of ith story level, U_{i+1} is upper displacement of $(i+1)^{th}$ story level, N_i is i^{th} story level axial load, N_{i+1} is $(i+1)^{th}$ story level axial load, $[K_G]$ is stiffness matrix which is added to the element stiffness matrix and $\{\Delta_u\}$ is incremental vectors of story displacement.
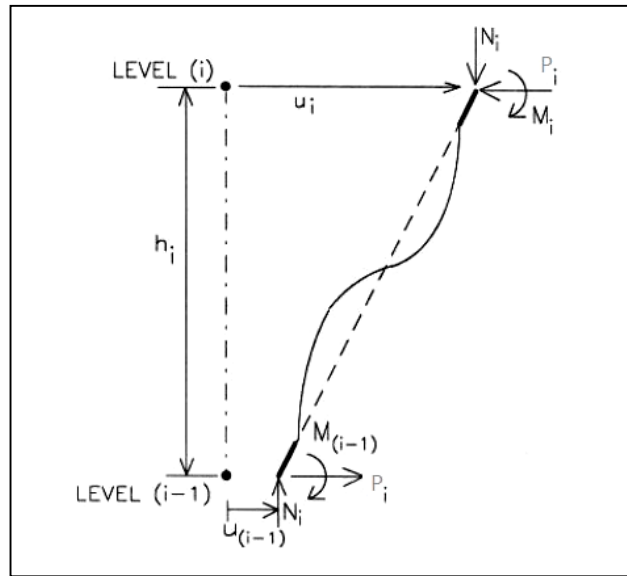
Figure 4.34: Performance of P-delta on a vertical element

By considering the significance of P-delta and how it can be affected on fragility curves, in this part, the fragility curves were drawn for without P-delta case. Figures 4.35, 4.36 and 4.37 show the comparison of fragility curves between P-delta effect case and without P-delta effect case for four, six and eight story buildings, respectively. Also the amount of mean and standard deviation which were used for drawing the fragility curves in case of without P-delta are tabulated in Table 4.9. The obtained results showed that by increasing the building height, the P-delta effect is increased. Also the similar trends are shown by increasing the damage levels.
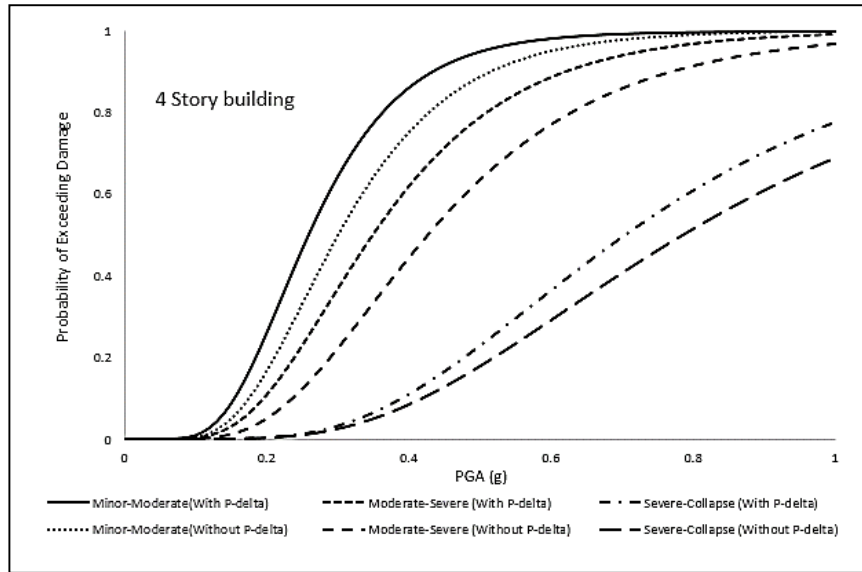
Figure 4.35: The fragility curves for four story building with and without P-delta effect cases
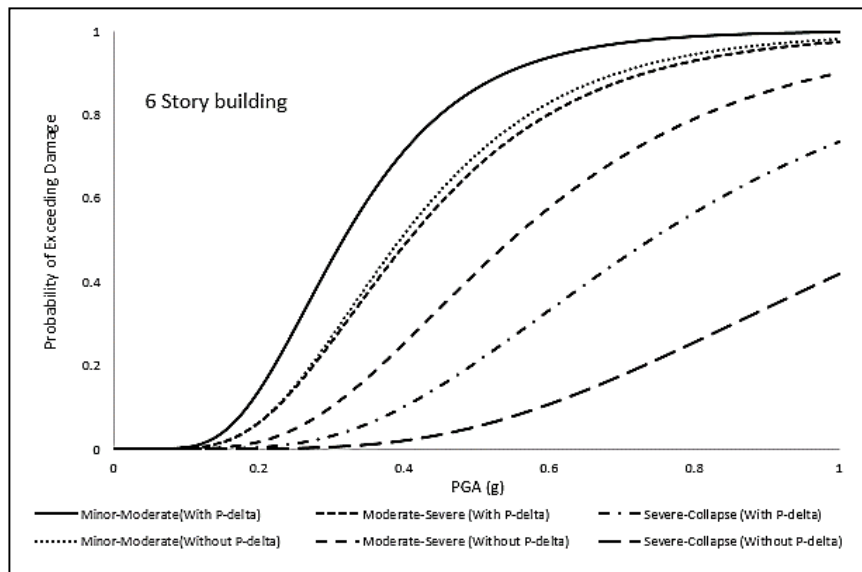
Figure 4.36: The fragility curves for six story building with and without P-delta effect cases
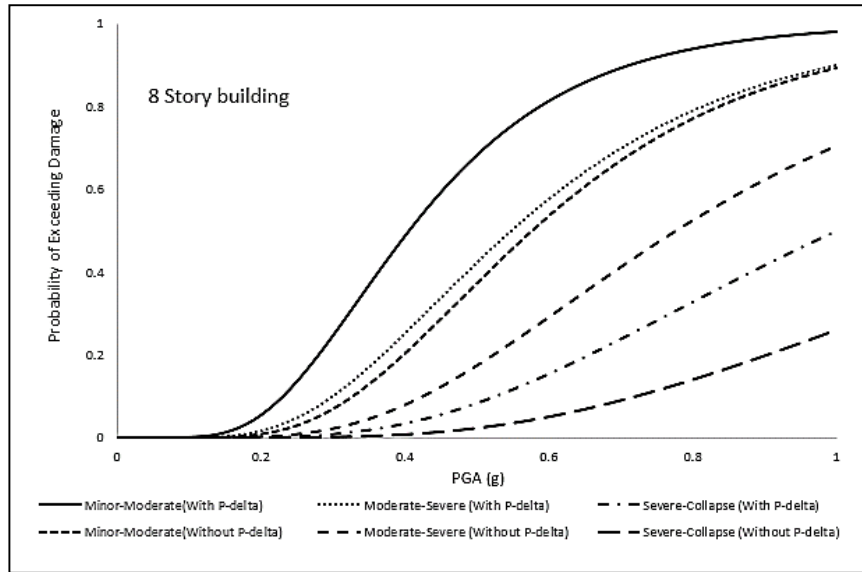
Figure 4.37: The fragility curves for eight story building with and without P-delta effect cases

Table 4.9: The used mean and standard deviation values for drawing the fragility curves for with and without P-delta cases

		With P-delta			Without P-delta		
	Level	Minor-Moderate	Moderate-Sever	Sever-Collapse	Minor-Moderate	Moderate-Sever	Sever-Collapse
Mean	4	0.28	0.39	0.78	0.33	0.48	0.89
	6	0.35	0.45	0.83	0.44	0.61	1.25
	8	0.45	0.61	1.13	0.64	0.87	1.59
Standard Deviation	4	0.64	0.67	0.89	0.65	0.70	0.94
	6	0.66	0.69	0.91	0.70	0.79	1.14
	8	0.71	0.79	1.07	0.82	0.93	1.33

4.5 2D model

In this section, the effect of considering the 2D models instead of 3D models on fragility curves was evaluated. For this aim, the weakest frames from each model were selected (Figures 3.3, 3.5 and 3.7) and the fragility curves were drawn for each frame. Figures 4.38, 4.39 and 4.40 show the comparison of fragility curves between 2D models and 3D models for four, six and eight story buildings, respectively. Also the amount of mean and standard deviation which were used for drawing the fragility curves are tabulated in Table 4.10. Comparison of these curves show that there are excessive difference between 2D models and 3D models. Also using 2D models instead of 3D models are inaccurate and unreliable. In fact, a 2D model cannot express all characteristics and features of a 3D model.
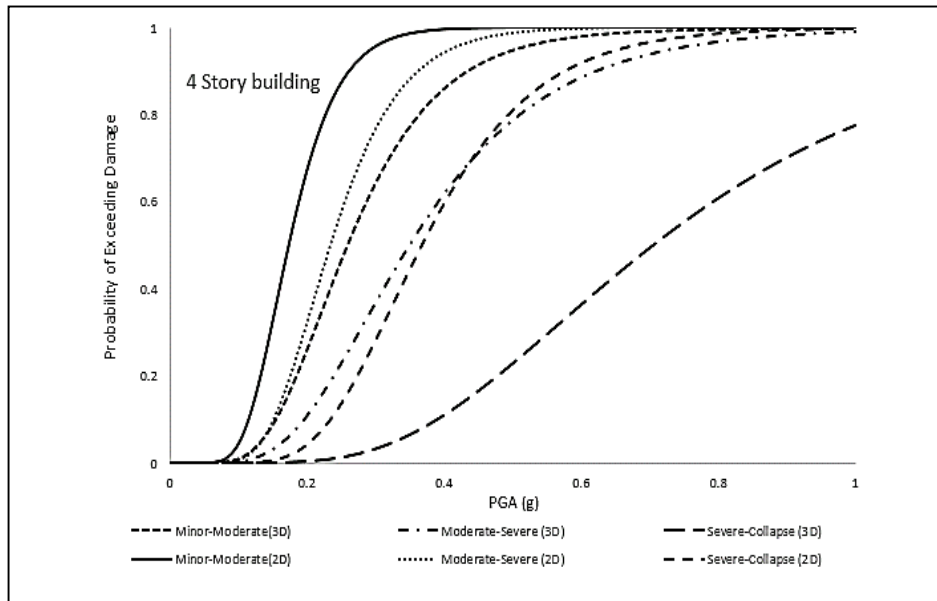
Figure 4.38: The fragility curves for 2D and 3D models of four story building
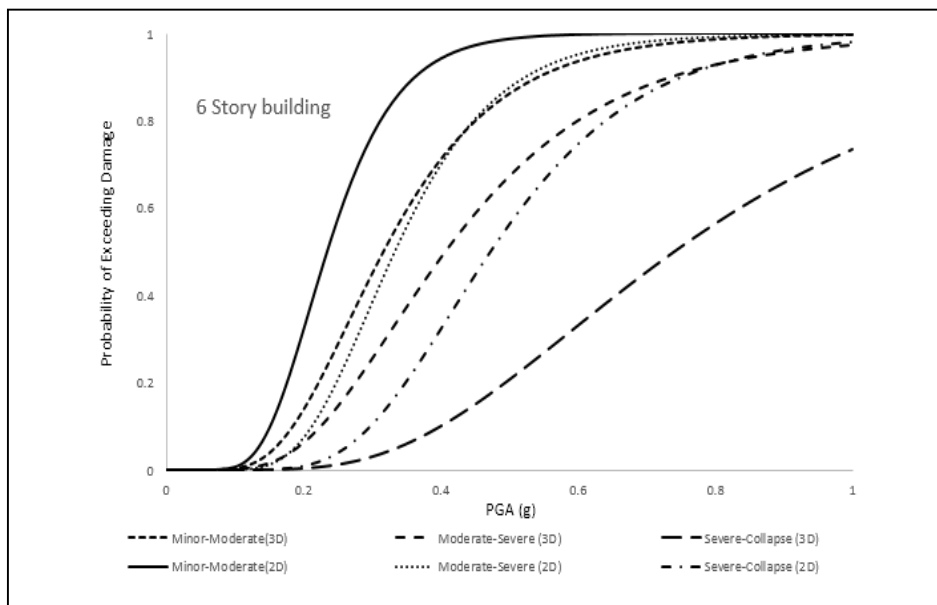
Figure 4.39: The fragility curves for 2D and 3D models of six story building
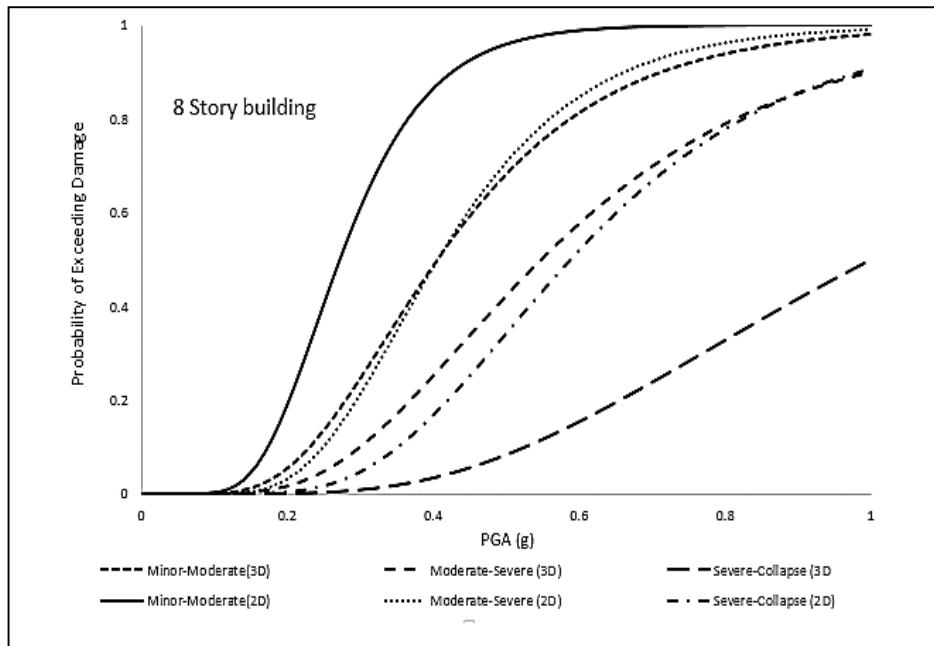
Figure 4.40: The fragility curves for 2D and 3D models of eight story building

Table 4.10: The used mean and standard deviation values for drawing the fragility curves for 2D and 3D models

	Level	3D model			2D model		
		Minor-Moderate	Moderate-Sever	Sever-Collapse	Minor-Moderate	Moderate-Sever	Sever-Collapse
Mean	4	0.28	0.39	0.78	0.18	0.25	0.39
	6	0.35	0.45	0.83	0.25	0.35	0.50
	8	0.45	0.61	1.13	0.29	0.44	0.64
Standard Deviation	4	0.64	0.67	0.89	0.69	0.71	0.78
	6	0.66	0.69	0.91	0.71	0.76	0.83
	8	0.71	0.79	1.07	0.72	0.77	0.86

4.6 Aftershock effect

Earthquakes are often composed of three parts including; foreshocks, main shocks and aftershocks. The data obtained from earthquakes history showed that the aftershocks may occur mostly after the strong main shocks. As an example, in China (May 12, 2008), five aftershocks were recorded (MW > 6.0) following the main shock with magnitude equal to 8.0. Since that the aftershocks often may occur in short intervals of time, therefore the repair of damaged buildings under the main shock in limited time is impossible and it increases the level of building damage and also causes collapse. On the other hand, all seismic codes only design the structures based on the main shock. Therefore considering the aftershocks effect should be taken into account.

Several researches showed that, when the distance of rupture for aftershock is smaller than main shock, the severity of aftershock is more than the main shock. As an example, in Chi-Chi earthquake, the distance of rupture for main shock and aftershock were equal to 10.8 km and 6.2 km, respectively, whereas the PGA of aftershock was 1.379 times more than main shock. Therefore, the ratio of PGA for aftershock to main shock is considered as a significant factor (Zhai et al., 2014; Zhang et al., 2013).

In this study, based on limited data for Famagusta city, five records were selected from Berkeley data base site (PEER) by considering the strike-slip mechanism of fault. For each record, the largest aftershock was considered. The information of this data is tabulated in Table 4.11. Since there are sequences between main shock and aftershock, therefore in nonlinear dynamic analysis process, 50 seconds gap was considered after the main shock in order to stop the vibration of building due to damping.

Table 4.11: The information of main shock and aftershock

Earth quake Name	Main shocks		Aftershocks	
	Event	PGA (g)	Event	PGA (g)
Chalfant Valley	20/07/1986 14:29	0.285	21/07/1986 14:42	0.447
Helena, Montana	31/10/1935 18:38	0.173	31/10/1935 19:18	0.041
Imperial Valley	15/10/1979 23:16	0.519	15/10/1979 23:19	0.238
Livermore	24/01/1980 19:00	0.229	27/01/1980 02:33	0.041
Superstitn Hills	24/11/1987 05:14	0.134	24/11/1987 13:16	0.207

4.6.1 Chalfant Valley earthquake

This earthquake has happened in southern of Mono County near Bishop and Chalfant, California and recorded from 54428-Zack Brothers Ranch station with main shock magnitude 5.77 Mw and epicentral distance equal to 10.54 km. The aftershock has happened thirteen minutes later and recorded from same station with magnitude 6.19 Mw and epicentral distance equal to 14.33 km. The ratio of PGA for aftershock to main shock is equal to 1.568. The acceleration of main shock along aftershock is shown in Figure 4.41. The amount of total damage (based on park and Ang damage index) under the main shock for four, six and eight story were obtained equal to 0.042, 0.029 and 0.013, respectively, whereas, these damages reached to 0.1, 0.067 and 0.036 after adding the aftershock. The plastic hinge performance of each member due to only main shock and main shock along aftershock cases for four, six and eight story

buildings are shown in figures 4.42-4.47, respectively. The hollow circle and X symbol show that the plastic hinge developed and cracking or yield in hinge, respectively. Also the imposed damage of all columns and beams caused by main shock versus main shock along aftershock are shown in figure 4.48.
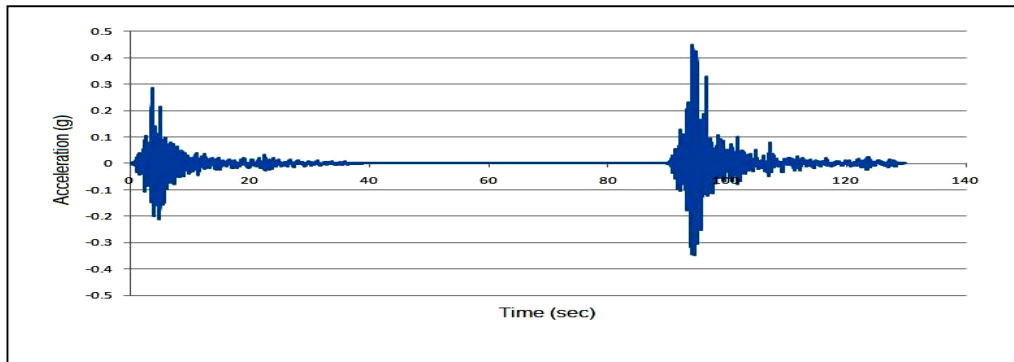
Figure 4.41: The acceleration of main shock along aftershock for Chalfant Valley earthquake
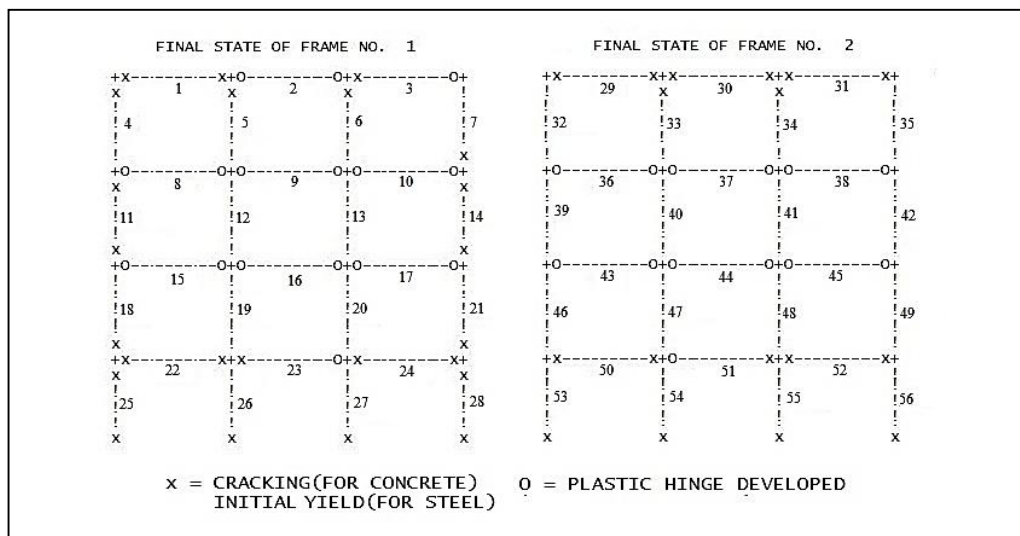
Figure 4.42: The plastic hinge performance for four story building under main shock
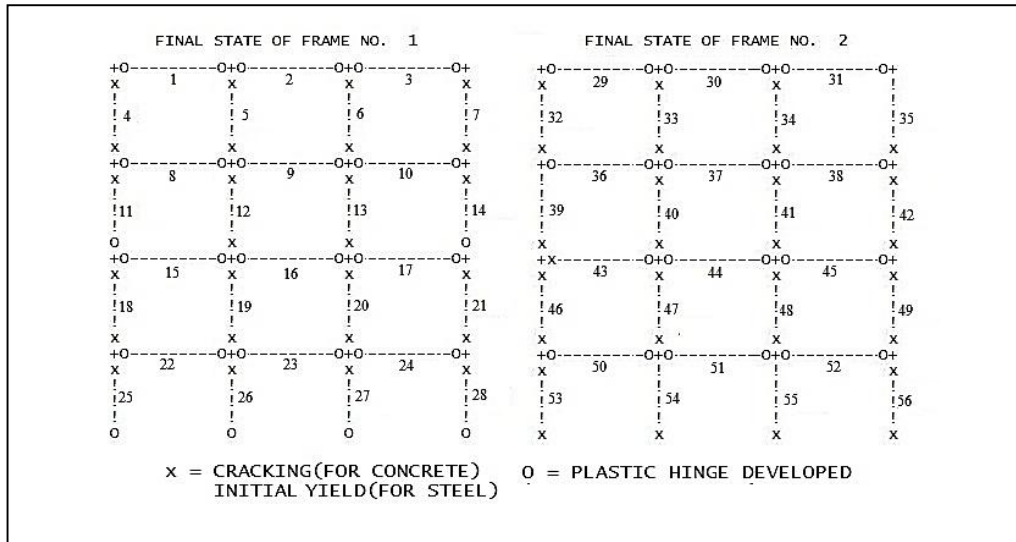
Figure 4.43: The plastic hinge performance for four story building under main shock along aftershock
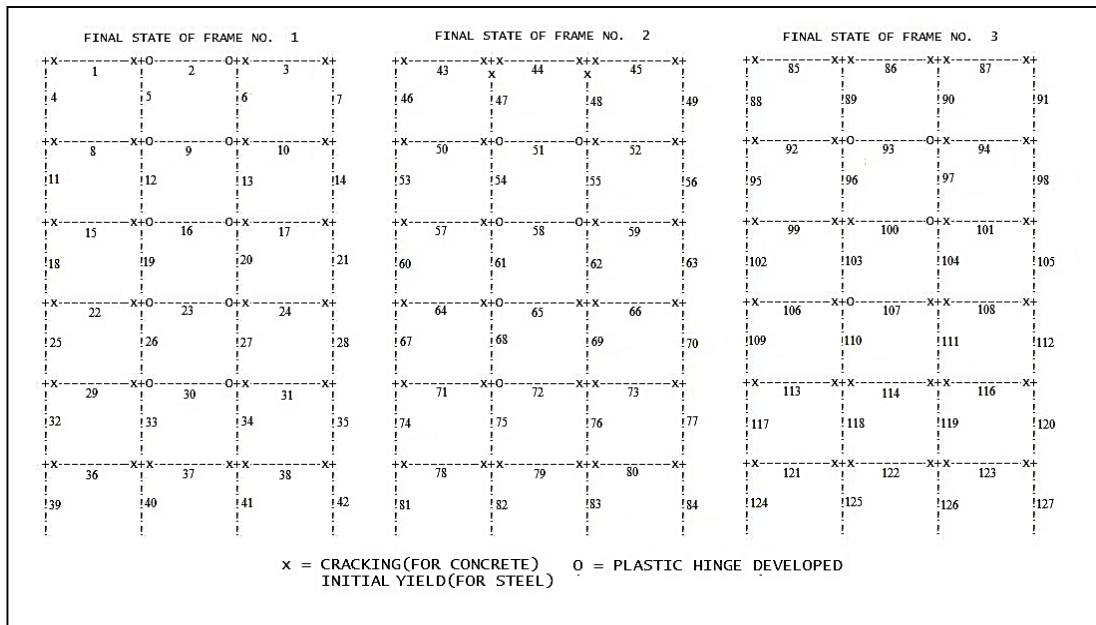
Figure 4.44: The plastic hinge performance for six story building under main shock
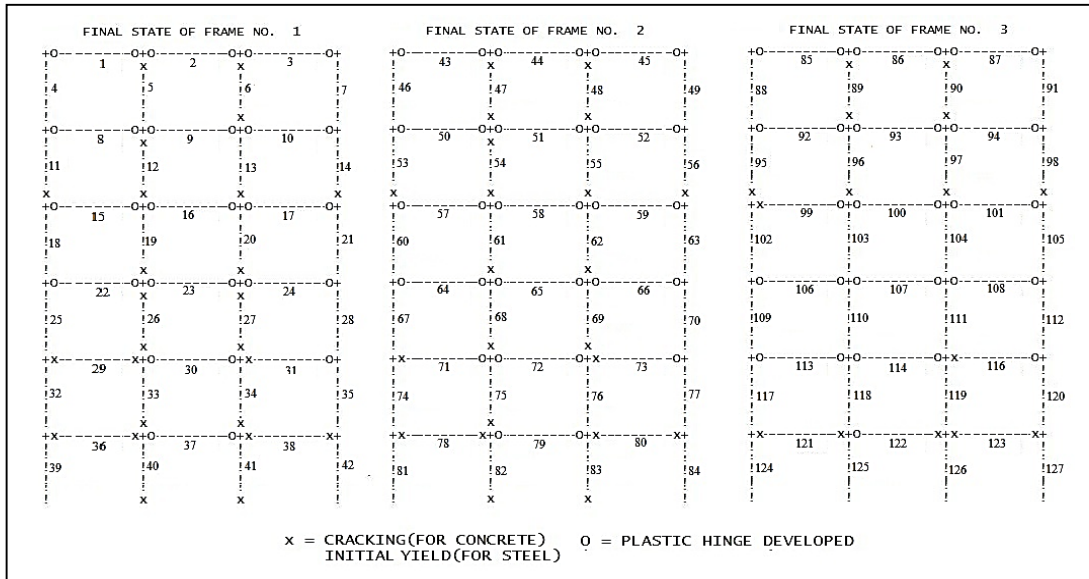
Figure 4.45: The plastic hinge performance for six story building under main shock along aftershock
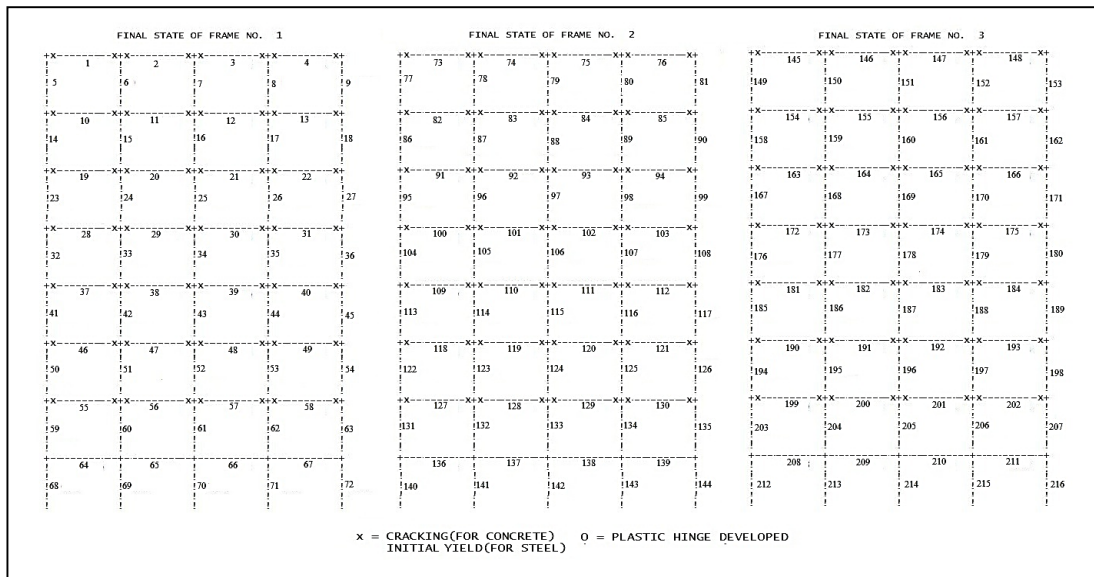
Figure 4.46: The plastic hinge performance for eight story building under main shock
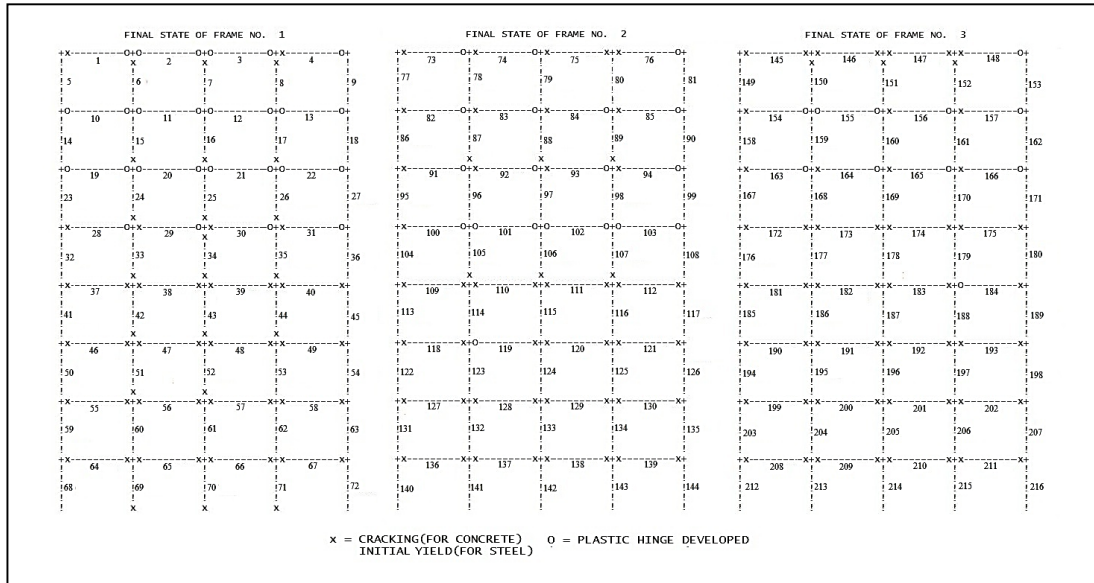
Figure 4.47: The plastic hinge performance for eight story building under main shock along aftershock
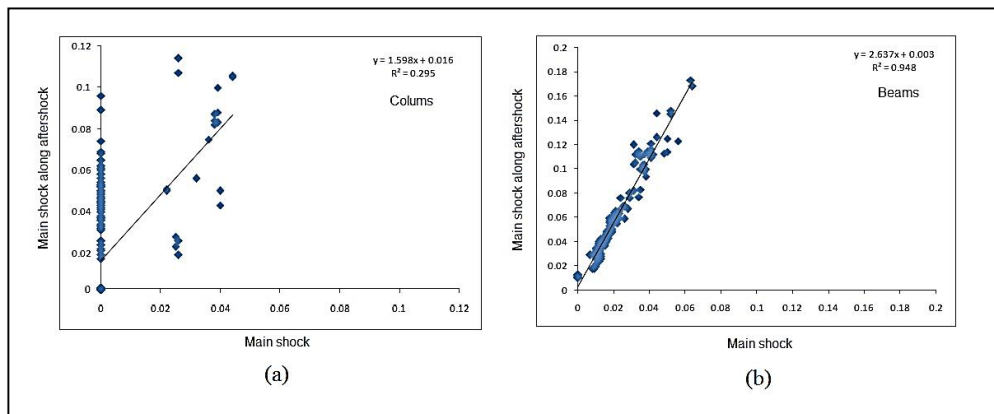
Figure 4.48: The imposed damage for main shock versus main shock along aftershock for (a) all columns and (b) all beams

4.6.2 Helena, Montana earthquake

This earthquake has happened in Montana, with an epicenter near Helena and recorded from 2022-Carroll College station with main shock magnitude 6.20 Mw and epicentral distance equal to 6.31 km. The aftershock has happened forty minutes later and recorded from same station with magnitude 6.00 Mw and epicentral distance equal to 6.31 km. The ratio of PGA for aftershock to main shock is equal to 0.237. The acceleration of main shock along aftershock is shown in Figure 4.49. The amounts of

total damage under the main shock for four, six and eight story buildings were obtained as 0.035, 0.025 and 0.013, respectively. Also the same damages were obtained for main shock along aftershock case.
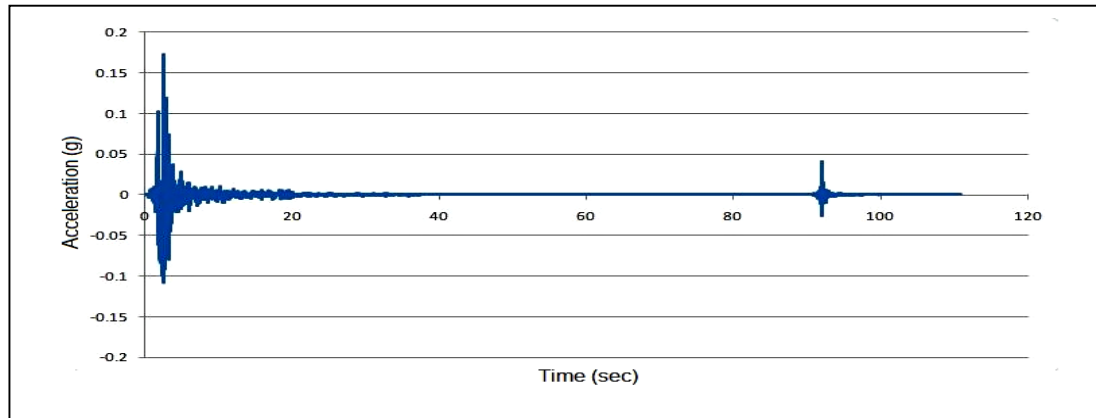
Figure 4.49: The acceleration of main shock along aftershock for Helena earthquake

4.6.3 Imperial Valley earthquake

This earthquake has happened in south of the Mexico–United States border and recorded from 952-El Centro Array #5 station with main shock magnitude 6.53 Mw and epicentral distance equal to 27.8 km. The aftershock has happened three minutes later and recorded from same station with magnitude 5.01 Mw and epicentral distance equal to 10.09 km. The ratio of PGA for aftershock to main shock is equal to 0.459. The acceleration of main shock along aftershock is shown in Figure 4.50. The amounts of total damage under the main shock for four, six and eight story buildings were obtained as 0.436, 0.182 and 0.105, respectively. Also the same damages were obtained for main shock along aftershock case.
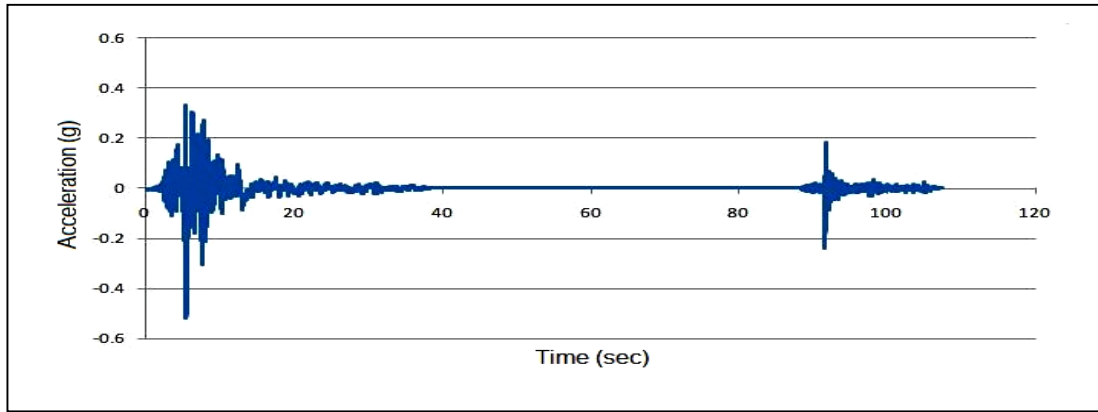
Figure 4.50: The acceleration of main shock along aftershock for Imperial Valley earthquake

4.6.4 Livermore earthquake

This earthquake has happened in North of Livermore Valley, California and recorded from 1265-Del Valle Dam (Toe) station with main shock magnitude 5.80 Mw and epicentral distance equal to 26.79 km. The aftershock has happened three days and seven hours and thirty three minutes later and recorded from same station with magnitude 5.42 Mw and epicentral distance equal to 13.05 km. The ratio of PGA for aftershock to main shock is equal to 0.179. The acceleration of main shock along aftershock is shown in Figure 4.51. The amounts of total damage under the main shock for four, six and eight story buildings were obtained as 0.047, 0.041 and 0.022, respectively. Also the same damages were obtained for main shock along aftershock case.

79
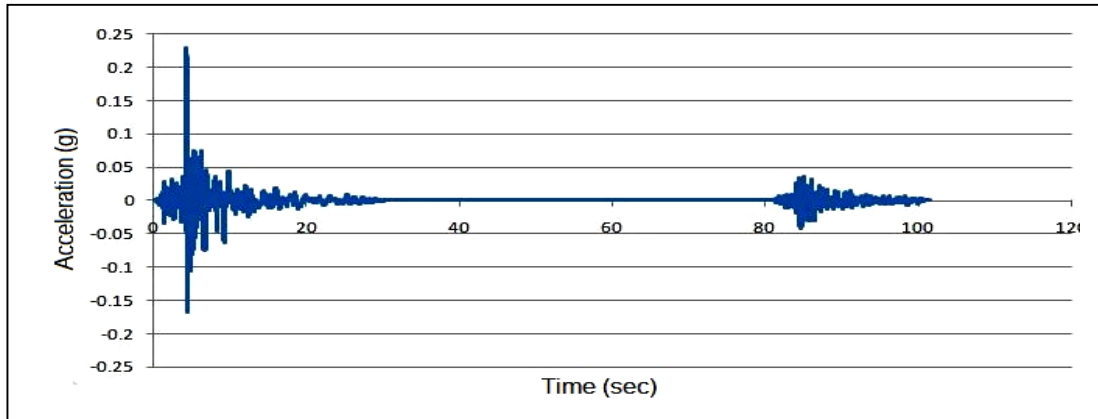
Figure 4.51: The acceleration of main shock along aftershock for Livermore earthquake

4.6.5 Superstitn Hills earthquake

This earthquake has happened in west of Westmorland, California and recorded from 5210-Wildlife Liquef. Array station with main shock magnitude 6.22 Mw and epicentral distance equal to 24.79 km. The aftershock has happened eight hours and two minutes later and recorded from same station with magnitude 6.54 Mw and epicentral distance equal to 29.41 km. The ratio of PGA for aftershock to main shock is equal to 1.545. The acceleration of main shock along aftershock is shown in Figure 4.52. The amount of total damage under the main shock for four, six and eight story buildings were obtained as 0.033, 0.027 and 0.022, respectively, whereas, these damages were reached to 0.265, 0.174 and 0.13 after adding the aftershock. The plastic hinge performance of each member due to only main shock and main shock along aftershock cases for four, six and eight story buildings are shown in figures 4.53-4.58, respectively. Also the imposed damage of all columns and beams caused by main shock versus main shock along aftershock are shown in figure 4.59.
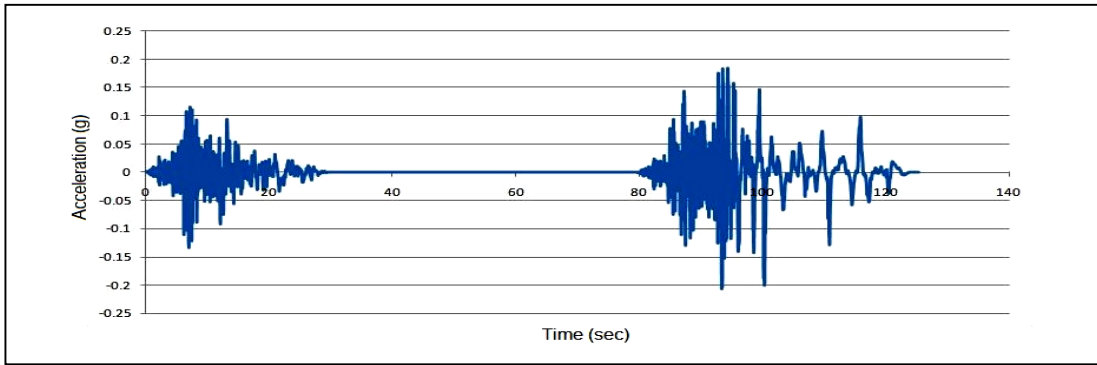
Figure 4.52: The acceleration of main shock along aftershock for Superstitn Hills
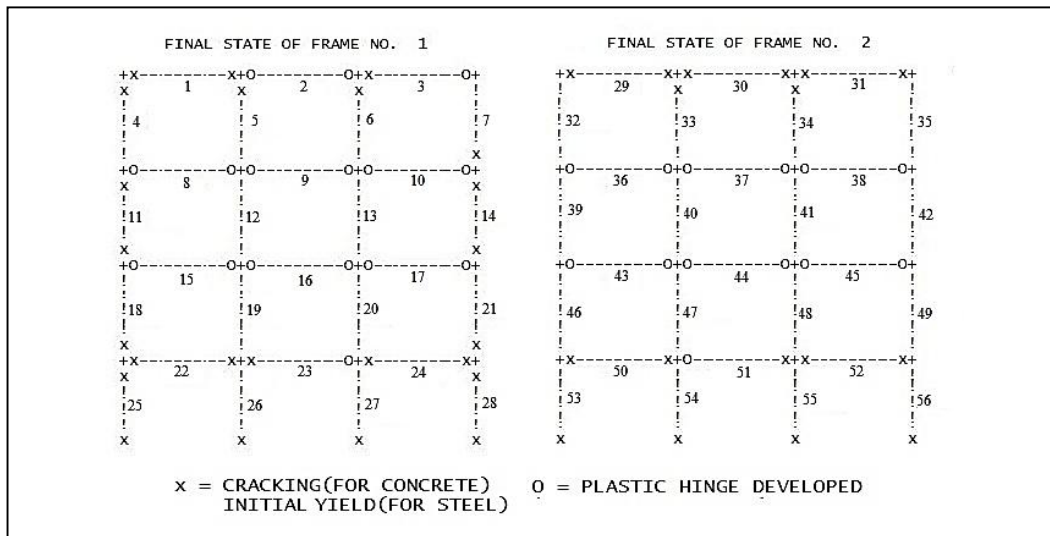
Figure 4.53: The plastic hinge performance for four story building under main shock
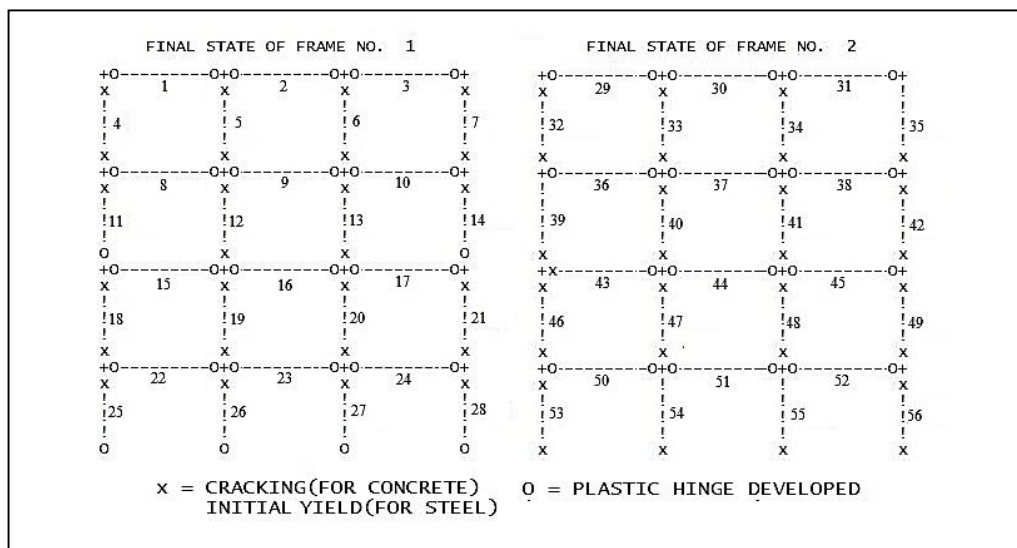
Figure 4.54: The plastic hinge performance for four story building under main shock along aftershock
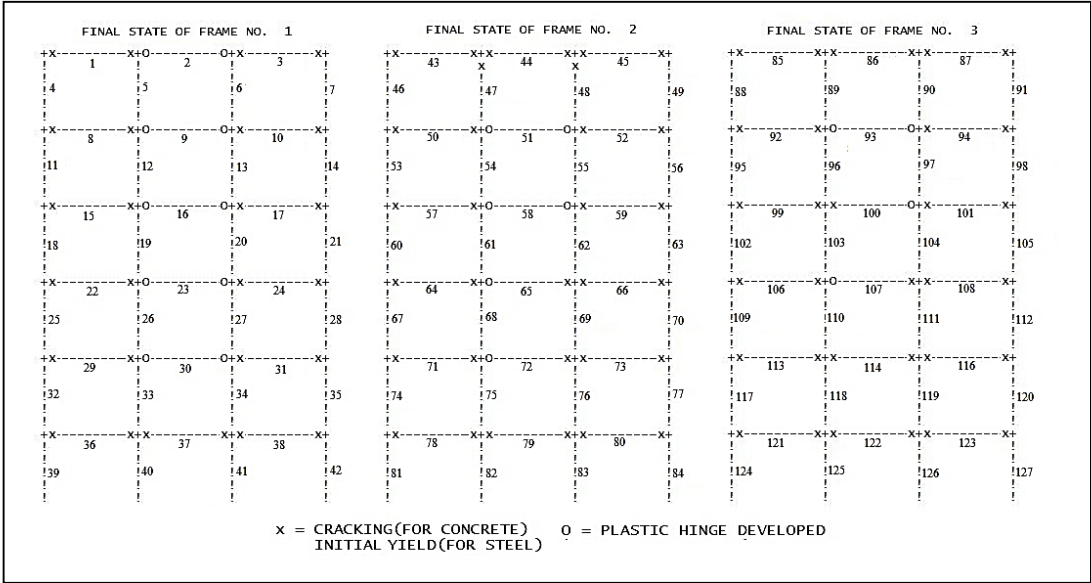
Figure 4.55: The plastic hinge performance for six story building under main shock
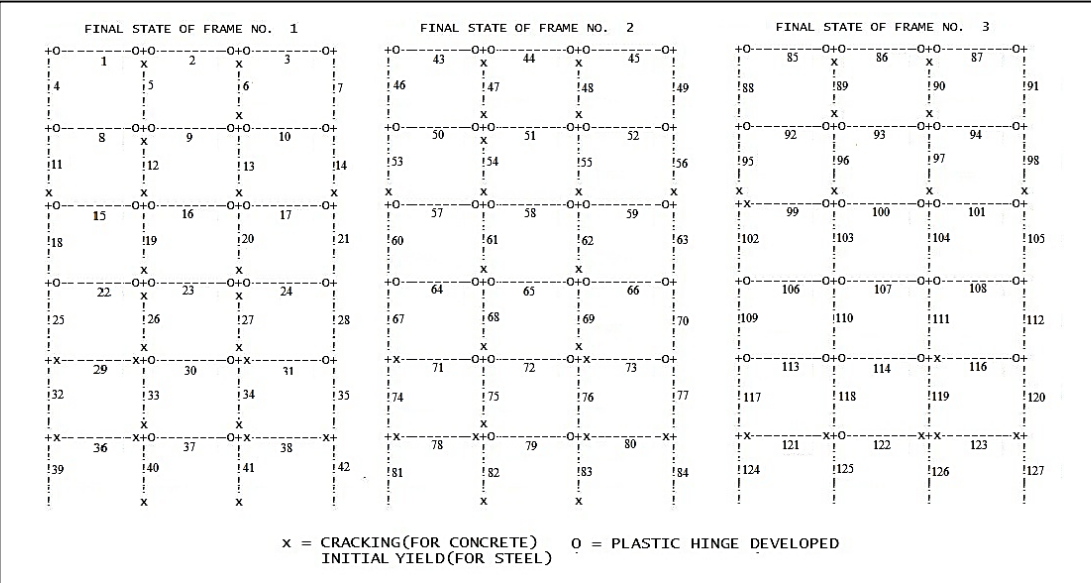
Figure 4.56: The plastic hinge performance for six story building under main shock along aftershock
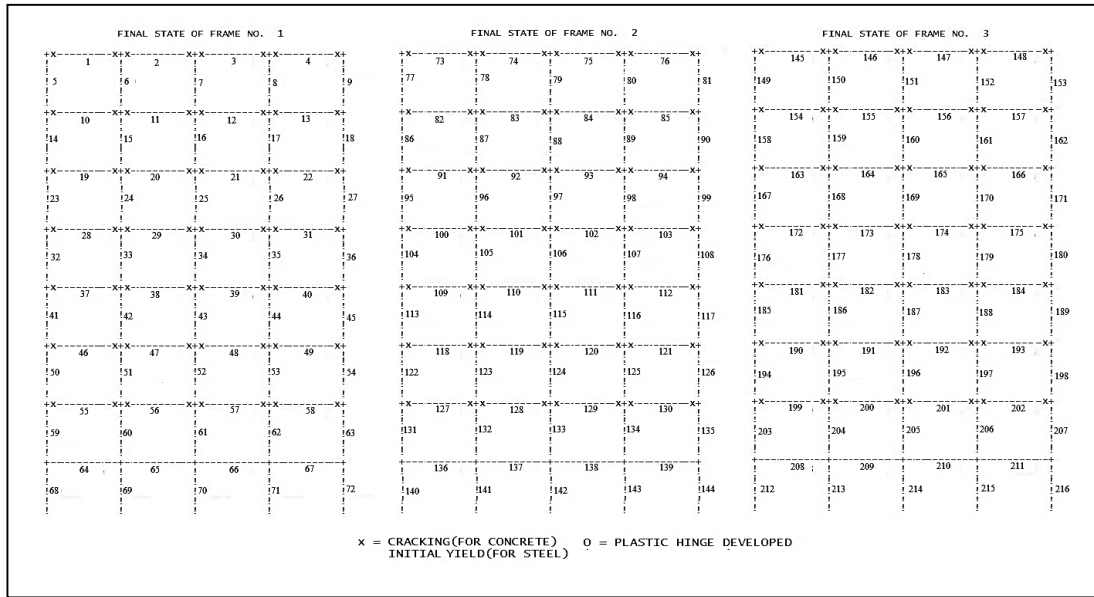
Figure 4.57: The plastic hinge performance for eight story building under main shock
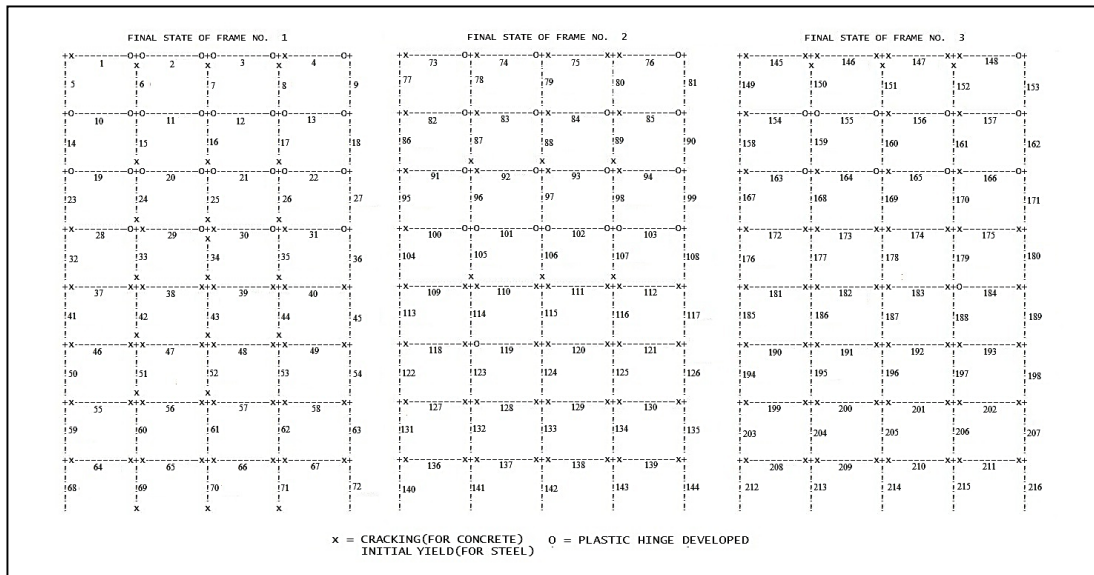
Figure 4.58: The plastic hinge performance for eight story building under main shock along aftershock

83
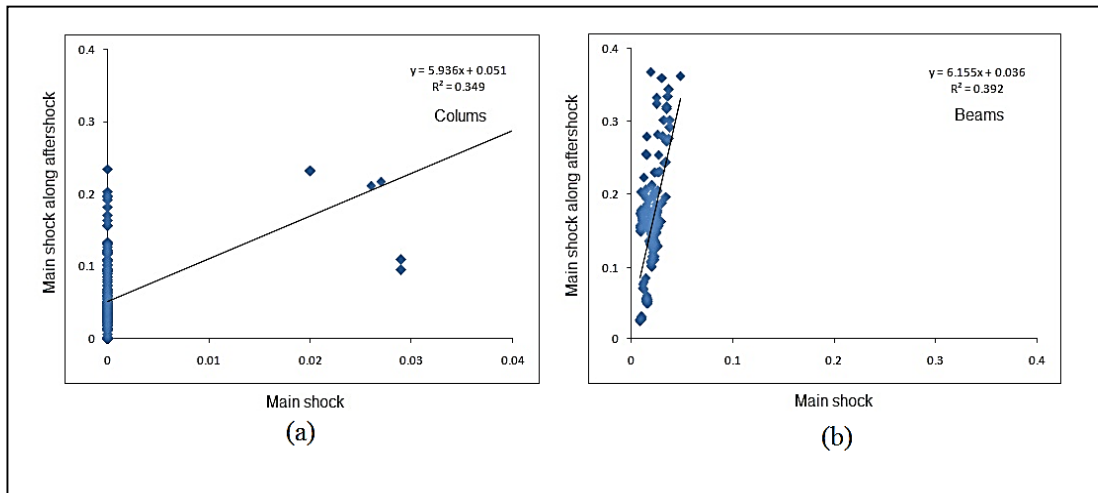
Figure 4.59: The imposed damage of main shock versus main shock along aftershock for (a) all columns and (b) all beams

Chapter 5

ANALYSIS AND RESULTS THROUGH ANN

5.1 Prediction of damage

In this chapter, ANN was used in order to predict the imposed damage of buildings under earthquake excitation. In fact, it can be applied as a rapid evaluation method. In this method, only parameters which are able to describe both the properties of building and ground motions characteristic should be considered. Therefore the selection of them should be taken into account.

5.1.1 Structural parameters

In this study, the structural parameters were selected without any relations to the engineering analysis, such as, top displacement, first mode period, inter-story drift, etc., and they were chosen based solely on the geometry of the structure. Therefore nine parameters were selected and defined as:

Building height / width ratio (*h/b*)

Length / width ratio in plan (*b/d*)

Number of stories (*N*)

Number of bays (*B*)

Maximum bay length (*M*)

Total moment of inertia for first story columns (I_C)

Total moment of inertia for first story beams (I_B)

Total bars area for first story columns (B_C)

Total bars area for first story beams (B_B)

Also, the ranges of each parameter are shown in Table 5.1.

Table 5.1: The range of structural parameters

Parameters	Range of parameters
h/b	1.476-1.958
b/d	0.730-0.885
N	4-8
B	3-4
M (m)	3-3.8
I_C (cm^4)	0.01155-0.1022
I_B (cm^4)	0.00135-0.004725
B_C (cm^2)	180.96-1507.96
B_B (cm^2)	79.02-381.92

5.1.2 Ground motion parameters

Since the earthquake is a complex phenomenon that is still not completely known, therefore the selection of effective ground motion parameters is not easy. In the recent century, many researches have been done in order to find the relation between ground motion parameters and building responses. Newmark et al. (1973) used PGV, PGA and PGD in order to draw the elastic response spectra. Extensive research has been conducted on the PGA/PGV ratio, for measuring the frequency content of the strong ground motions (Tso et al., 1992). In these studies, the best parameters among the various constraints were determined using mathematical function and regression

analysis. Riddell and Garcia (2001) used a set of 52 earthquake records, in order to establish the relationship between twenty-three intensity parameters of earthquake and four response variables including hysteretic energy, input energy, elastic and inelastic spectral ordinates. The results showed that no parameter could be singly satisfied over the entire frequency range. Indeed, they found that each ground acceleration, ground velocity and ground displacement indices were effective in the acceleration sensitive region, velocity sensitive region and displacement sensitive region, respectively.

In this study, a six story frame was selected and excited by 200 different ground motion records with various moment magnitudes ($5.2 \leq M \leq 8.3$), different source-to-site distances and strike-slip fault mechanism from the PEER source (PEER, 2013).

The distribution of dominant frequency for the records is shown in Figure 5.1. Also the proportion between PGA and effective time duration of records are presented in Figure 5.2. Figures 5.3 and 5.4 show the relationship between sites epicentral distances versus moment magnitude and 5-95% time duration, respectively.
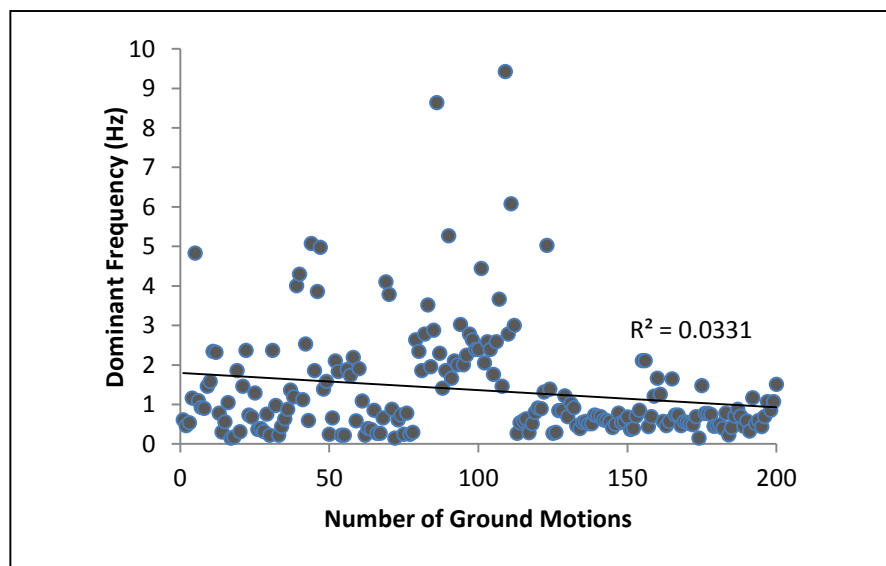
Figure 5.1: The dominant frequency values of records
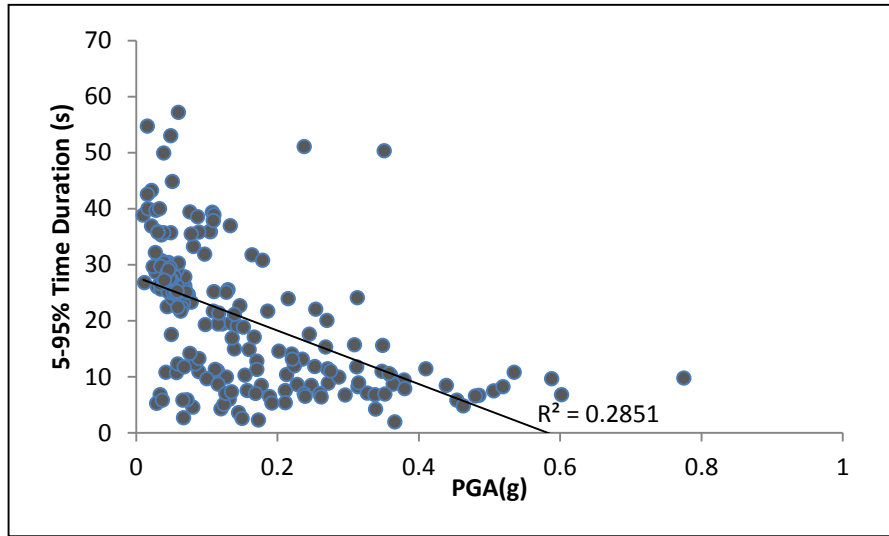
Figure 5.2: The effective time duration versus PGA
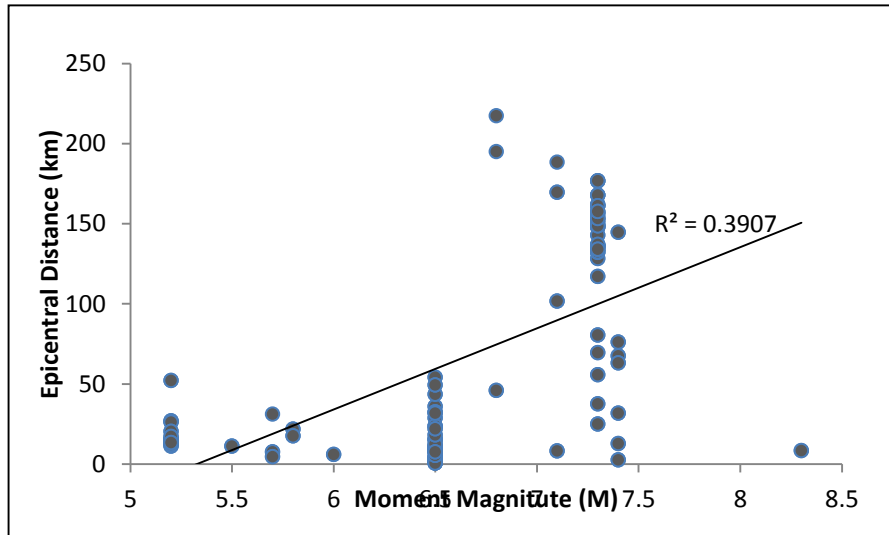
Figure 5.3: The epicentral distance values versus moment magnitude
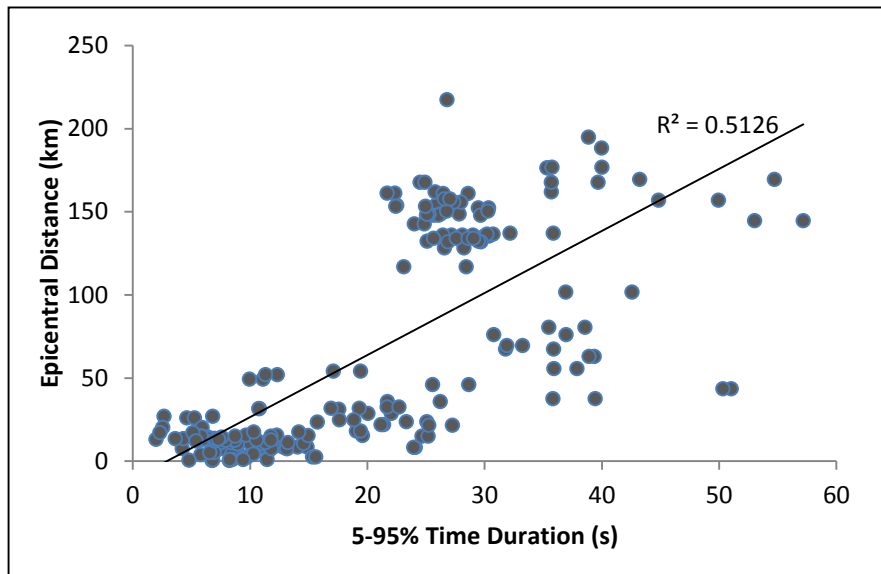
Figure 5.4: The epicenteral distance values versus the effective time duration

Therefore nine parameters of earthquake including; PGA, PGV, PGD, PGA/PGV, PGA/PGD, PGV/PGD, dominant frequency, effective time duration and fault line distance were selected as input data. The ranges of ground motion parameters are provided in Table 5.2. Also the amount of damage which is obtained based on nonlinear time history analysis of each record was considered as output.

Table 5.2: The ranges of ground motion parameters

Parameters	Definition	Range of parameters
PGA	Peak Ground Acceleration (g)	0.01-0.775
PGV	Peak Ground Velocity (cm/s)	1.1-109.8
PGD	Peak Ground Displacement (cm)	0.12-65.89
PGA/PGV	Ratio of PGA to PGV (g/cm.s^{-1})	0.002155-0.029773
PGA/PGD	Ratio of PGA to PGD (g/cm)	0.00211-0.558333
PGV/PGD	Ratio of PGV to PGD (s^{-1})	0.761548-20
D.F.	Dominant frequency (Hz)	0.146-9.4238
T.D.	5-95 % Time Duration (s)	1.98-57.17
E.D.	Epicentral Distance (km)	0.5- 217.4

In order to find a good relationship between input and output data and also find the more effective parameters of ground motion on the building performance, a MLP neural network was applied. In this network, all data was normalized between zero and one, then were shuffled and divided into three parts, i.e. 70 percent of total data for training process, 15 percent for validating process and 15 percent for testing process.

For finding the best fit of each data set, the RMSE, the mean square error (MSE) and the correlation coefficient (R) were considered (Darper and Smith, 1998). These criteria are described below:

Root Mean Square Error (RMSE):

RMSE is often used as a tool for measuring the difference between the predicted values and the actual values of one dataset. It is a good estimation for the standard deviation of a random set of the databases and is defined as:

$$RMSE = \sqrt{\frac{\sum_{i=1}^{n}(X_{pre}-X_{val})^2}{n}} \quad\quad\quad (4.7)$$

MSE is the mean square error and is calculated as the square of RMSE as follows:

$$MSE = RMSE^2 \quad\quad\quad (4.8)$$

Correlation Coefficient (R):

The correlation coefficient (R) is the measurement of the linear relationship degree between the two variables (predicted values and actual values). The range of correlation coefficient values change between +1 and -1 and is defined as:

$$R = \frac{\sum_{i=1}^{n}(X_i-\bar{X})*(Y_i-\bar{Y})}{\sqrt{\sum_{i=1}^{n}(X_i-\bar{X})^2*\sum_{i=1}^{n}(Y_i-\bar{Y})^2}} \quad\quad\quad (4.9)$$

where X_i is actual value, $\bar{X}$ is mean of actual values, Y_i is predicted value, $\bar{Y}$ is mean of predicted values and n is number of data set.

In this step, the network was trained based on all input data that are represented by nine neurons in input layer, optimum neurons in hidden layer and a neuron in output layer. The number of neurons in hidden layer was determined based on trial and error. Therefore twenty neurons were employed for this layer with tansig activation function. In training process, the network stopped at 19 iterations with gradient and MSE equal to 0.01871 and 0.00583, respectively. Also the best validation performance was 0.05820 and occurred at epoch 13. The values of RMSE, MSE, R, mean (μ) and standard deviation (σ) of errors are presented in Table 5.3. Figure 5.5 shows that the process of network training and error histogram for all data. The concentration of error bins around the zero line shows that the network was able to predict the damage values

with high accuracy. Moreover, the regression and fit function for train, validation, test and all data are shown in Figure 5.6.

Table 5.3: The RMSE, MSE, R, μ and σ values for each set of data

	Train Data	**Validation Data**	**Test Data**	**All Data**
RMSE	0.10920	0.24123	0.35997	0.19108
MSE	0.01192	0.05820	0.12958	0.03651
R	0.94892	0.81771	0.66528	0.85220
μ	-0.01521	0.04780	-0.02412	-0.00709
σ	0.10852	0.24049	0.36530	0.19143
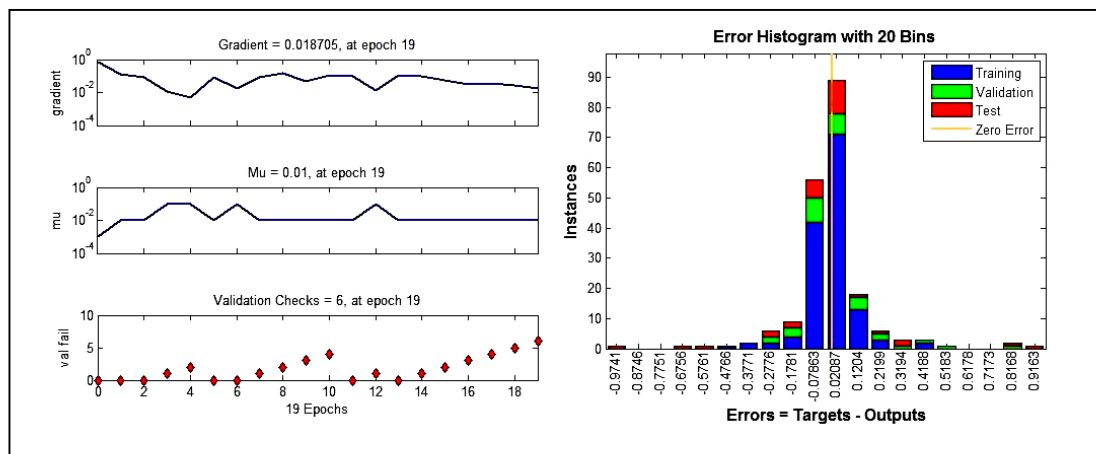
Figure 5.5: The network training process and error histogram
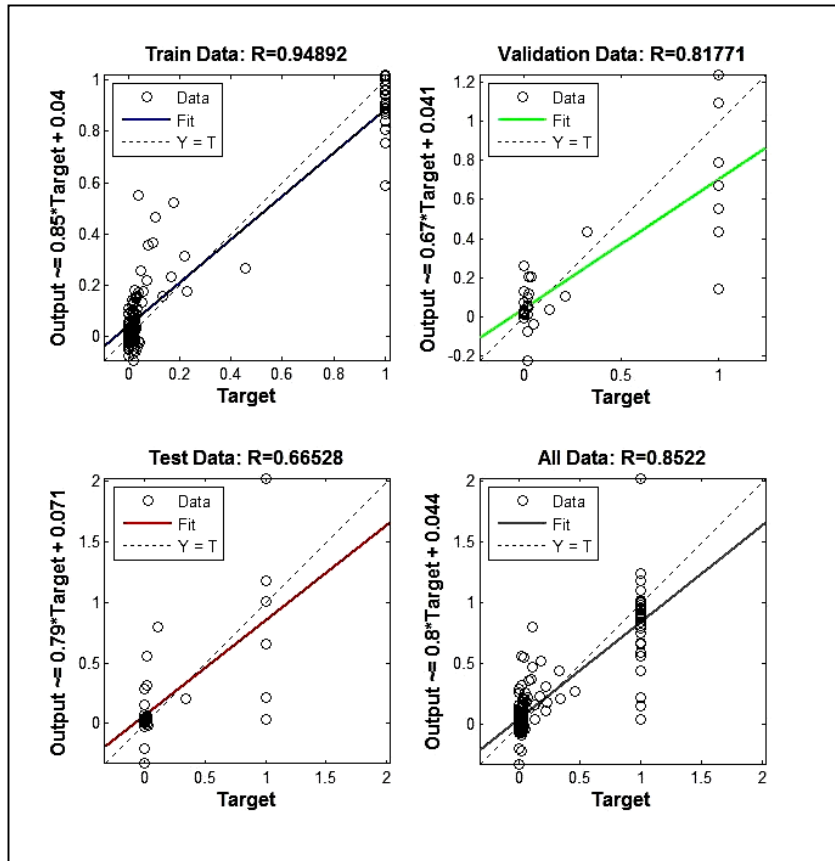
Figure 5.6: The regression and fit function for each set of data

In order to find the effective parameters of ground motion, the training process of network was repeated for nine times and in each time, one of the ground motion parameters was eliminated. Therefore, the number of neurons in input layer was reduced to eight. The results of this process are shown in Table 5.4.

Table 5.4: The RMSE, MSE, R, μ and σ values for all data.

Eliminated Parameter	RMSE	MSE	R	μ	σ
PGA	0.19337	0.03739	0.84401	0.00379	0.19382
PGV	0.23130	0.05350	0.80124	-0.08361	0.21620
PGD	0.20957	0.04392	0.82806	-0.01935	0.20920
PGA/PGV	0.23459	0.05503	0.77255	-0.01081	0.23493
PGA/PGD	0.21979	0.04831	0.82541	0.05024	0.21450
PGV/PGD	0.22133	0.04899	0.79408	0.01137	0.22159
Dominant Frequency	0.24655	0.06079	0.79006	-0.10129	0.22535
Effective Time Duration	0.19903	0.03961	0.83377	0.00186	0.19952
Fault line Distance	0.19532	0.03815	0.84128	-0.01292	0.19538

Based on extracted results (see Table 5.4), the minimum values of R were obtained for PGA/PGV, dominant frequency, PGV/PGD and PGV cases, respectively which is expressing that the network was sensitive to these parameters. Therefore the network was run based on these four parameters as input data (four neurons in input layer), ten hidden layer neurons (optimum neurons) and a neuron in output layer. In training process, the network stopped at 25 iterations with gradient and MSE equal to 0.00431 and 0.0332, respectively. Also the best validation performance was 0.01136 and

occurred at epoch 19. The values of RMSE, MSE, R, μ and σ are presented in Table 5.5. Moreover, Figure 5.7 shows the fitting function and regression for train, validation, test and all data.

Table 5.5: The RMSE, MSE, R, μ and σ values for each set of data.

	Train Data	Validation Data	Test Data	All Data
RMSE	0.18401	0.10659	0.27995	0.19277
MSE	0.03386	0.01136	0.07837	0.037161
R	0.87230	0.90892	0.65085	0.84514
μ	-0.00065	0.000099	-0.02014	-0.00346
σ	0.18467	0.10841	0.28400	0.19323
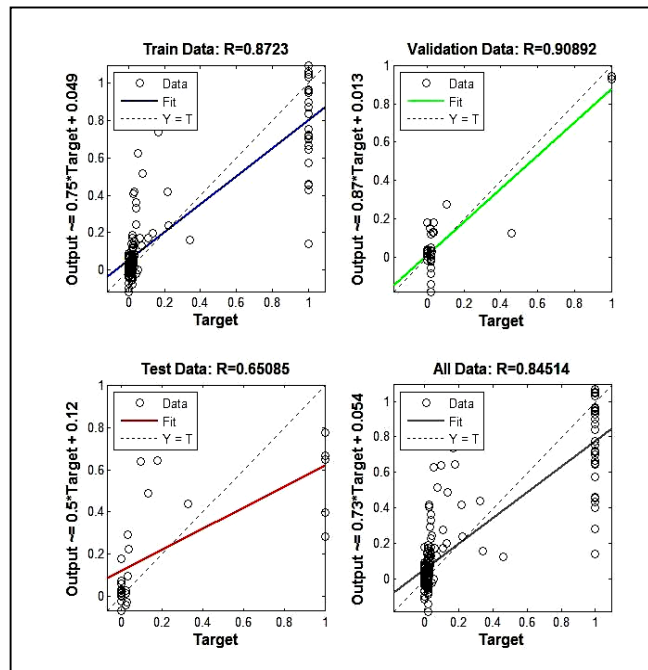
Figure 5.7: The regression and fit function for each set of data

The value of R obtained from two networks consist of all input data (nine parameters) and four sensitive data (four parameters) were obtained equal to 0.85220 and 0.84514, respectively which is showing around 0.8% difference between them. Also it should be considered that whereas the sample frame was in intermediate period region, the velocity controlled responses is more effective among the earthquake parameters. Therefore for buildings in this period range, it is suggested to use the above effective parameters which are sufficiently enough for evaluation of vulnerability instead of considering more ground motion characteristics.

Thus, in this study, the ground motion parameters has been selected based on above obtained results of previous section including; PGV, PGA/PGV, PGV/PGD and dominant frequency. The ranges of these parameters are tabulated in Table 5.6.

Table 5.6: The range of ground motion parameters

Parameters	Range of parameters
PGV	3.385-245.3
PGA/PGV	0.004-0.03
PGV/PGD	1.036-12.008
D.F.	0.22-1.929

5.1.3 Data generation, training and testing of ANN

In this section, again MLP neural network were employed to predict the vulnerability of sample buildings. For this aim, twenty suitable ground motion records were selected which had most correlation with design spectrum and scaled to ten different level of PGA. Then each scaled records applied to each sample. Therefore,

based on this process, 600 input data were generated. In this network, three layers were used including thirteen neurons in input layer, optimum neurons in hidden layer and a neuron in output layer which is representing the imposed damage values of sample buildings. Then the data were normalized and presented to the network. Also, the linear normalization method was used in order to change the input parameters range between zero and one using the equation 4.10 as:

$$S_x = \frac{(x - x_{min})}{(x_{max} - x_{min})} \qquad (4.10)$$
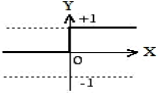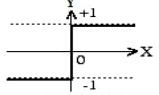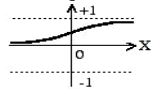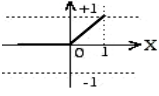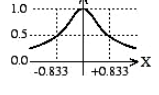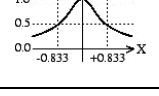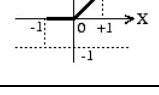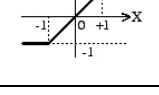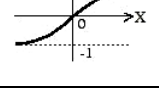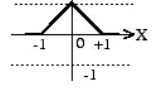
where S_x is the normalized value, x is variable, x_{min} is minimum value of all data and x_{max} is maximum value of all data.

All normalized data were shuffled and divided to three sets for training, validating and testing process. The number of neurons and type of activation function in hidden layer are very important parameters for network training process. In common networks, linear activation function was applied in output layer. However, for the hidden layer, different functions can be used depending on dataset. In this study, ten activation functions were examined and based on minimum error of test data, the best function was selected. The formulation and shape of these functions are shown in Table 5.7. The number of hidden layer neurons and suitable activation function were obtained based on minimum test error as following equation:

$$Error\ (\%) = \left(\frac{\sum_{i=1}^{k} |O_i - T_i|}{m * n}\right) * 100 \qquad (4.11)$$

where O_i is the output of the neural network, T_i is the desired output, k is the number of testing or training samples, m is the number of testing or training segments and n is the number of neural network outputs for the testing or the training procedures (Ozbay et al., 2006).

Table 5.7: Activation functions properties (Cortes and Vapnik (1995))

Function name	Formula	Graph
Hard-limit transfer function	$f(x) = \begin{cases} 0, & x < 0 \\ 1, & x \geq 0 \end{cases}$	
Symmetric hard-limit transfer function	$f(x) = \begin{cases} -1, & x < 0 \\ 1, & x \geq 0 \end{cases}$	
Log-sigmoid transfer function	$f(x) = \dfrac{1}{(1 + exp(-x))}$	
Positive linear transfer function	$f(x) = \begin{cases} 0, & x < 0 \\ x, & x \geq 0 \end{cases}$	
Radial basis transfer function	$f(x) = exp(-x^2)$	
Normalized radial basis transfer function	$f(x) = \dfrac{exp(-x^2)}{sum(exp(-x^2))}$	
Saturating linear transfer function	$f(x) = \begin{cases} 0, & x < 0 \\ x, & 0 < x \leq 1 \\ 1, & x \geq 1 \end{cases}$	
Symmetric Saturating linear transfer function	$f(x) = \begin{cases} -1, & x < -1 \\ x, & -1 < x \leq 1 \\ 1, & x \geq 1 \end{cases}$	
Hyperbolic tangent sigmoid transfer function	$f(x) = \dfrac{2}{(1 + exp(-2x))} - 1$	
Triangular basis transfer function	$f(x) = \begin{cases} 0, & x < -1 \\ 1 - |x|, & -1 < x \leq 1 \\ 0, & x \geq 1 \end{cases}$	

Based on equation 4.11, for each function, the error values of test data were calculated and the optimum number of hidden layer neurons was obtained. For

different number of neurons, the test error values of each activation function are shown

in Figure 5.8.
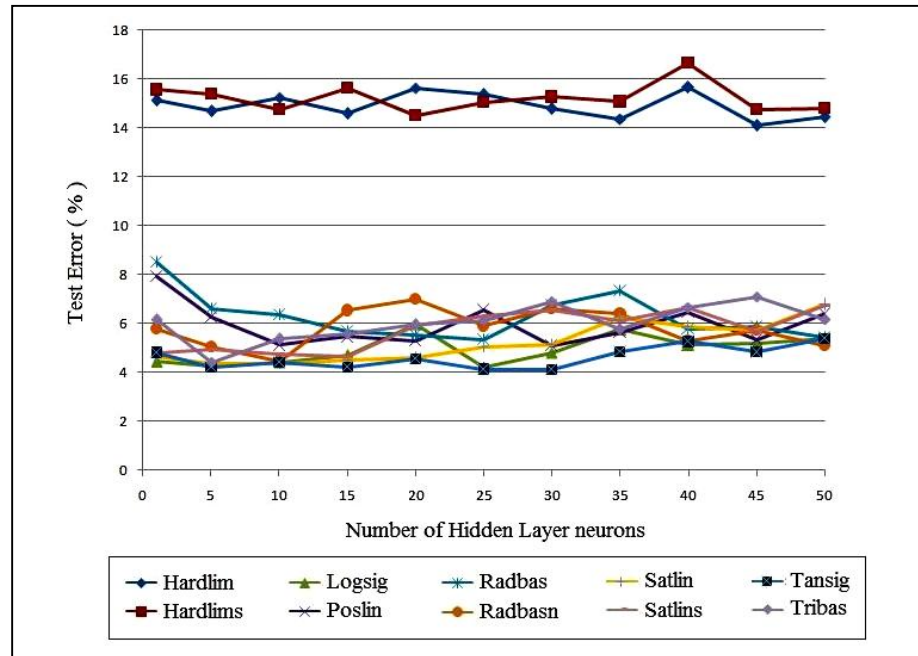
Figure 5.8: Number of hidden neurons versus test error

Moreover, the optimum number of hidden layer neurons and the test error values

for each activation function are shown in Table 5.8. The results showed that hyperbolic

tangent sigmoid function with thirty neurons (minimum test error) was the best

activation function for this set of data.

Table 5.8: The optimum number of neurons and test error values for different activation functions

Function	Optimum Number of hidden neurons	Test Error (%)
Hard-limit transfer function	45	14.10
Symmetric hard-limit transfer function	20	14.50
Log-sigmoid transfer function	25	4.21
Positive linear transfer function	30	5.09
Radial basis transfer function	25	5.33
Normalized radial basis transfer function	10	4.46
Saturating linear transfer function	10	4.37
Symmetric Saturating linear transfer function	15	4.67
Hyperbolic tangent sigmoid transfer function	**30**	**4.13**
Triangular basis transfer function	15	4.41

In training process, the networks stopped after 41 iterations with MSE and Gradient equal to 0.0121 and 0.00518, respectively. The best validation performance was 0.040328 at epoch 35. The values of RMSE, MSE, R, μ and σ are presented in Table 5.9. Also the weight matrix and bias terms of each network layer were represented in appendix C.

Table 5.9: The RMSE, MSE, R, μ and σ values for each set of data

	Train Data	Validation Data	Test Data	All Data
RMSE	0.11950	0.20082	0.20921	0.15037
MSE	0.01428	0.040328	0.04377	0.02261
R	0.96290	0.90163	0.88393	0.94116
μ	-0.005615	-0.03355	-0.05502	-0.01722
σ	0.11951	0.19910	0.20298	0.14951

Figure 5.9 shows the error histogram for all data. The concentration of error bins around the zero line shows that the network is able to predict the damage values with high accuracy. Moreover, the regression and fit function for train, validation, test and all data are shown in Figure 5.10.
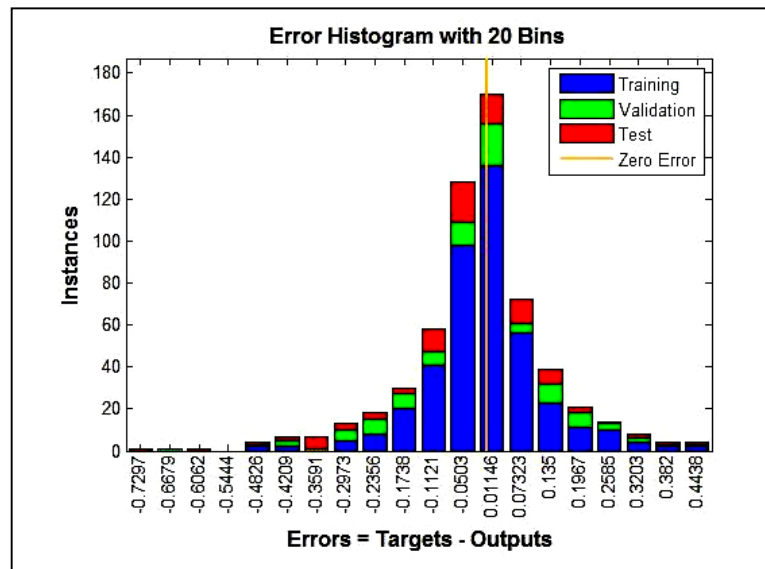
Figure 5.9: The error histogram for all data
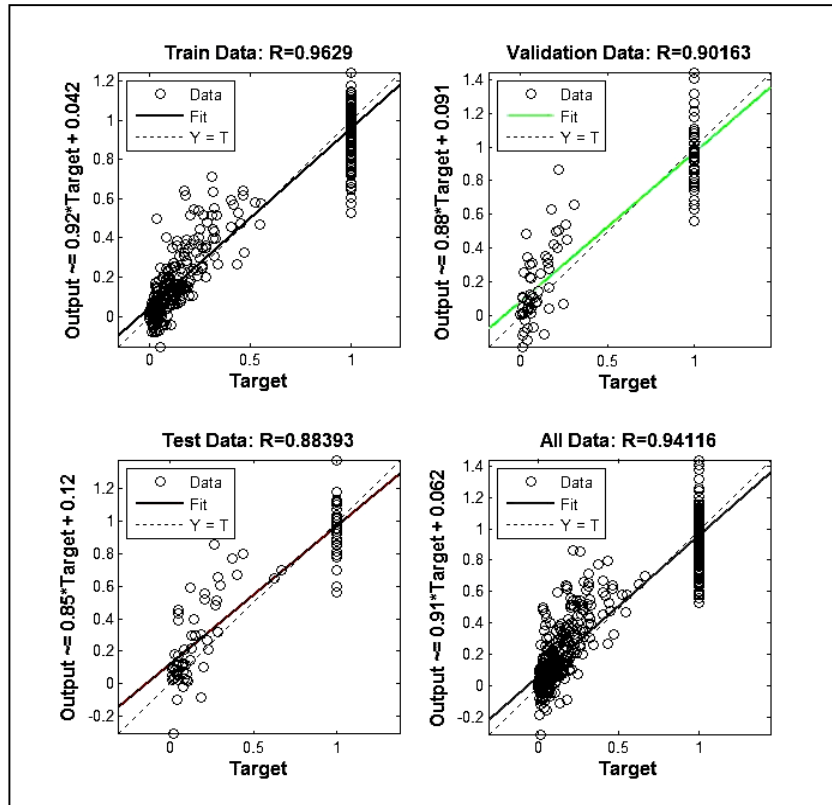
Figure 5.10: The regression and fit function for each set of data

Therefore, using the obtained results of ANN, the amount of damage was predicted and the fragility curves were drawn. Figures 5.11, 5.12 and 5.13 represent the fragility curves for different limit states and each story building which compared to real fragility curves, respectively. Also, the amounts of mean and standard deviation of log-normal cumulative distribution function which were used for drawing the fragility curves are shown in Table 5.10.
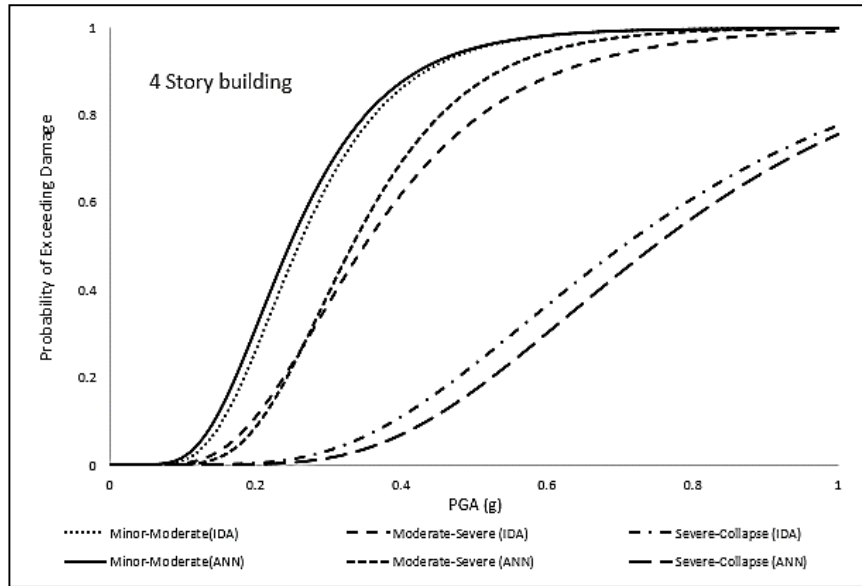
Figure 5.11: Comparison of the generated fragility curves by analysis and ANN
methods for four story building
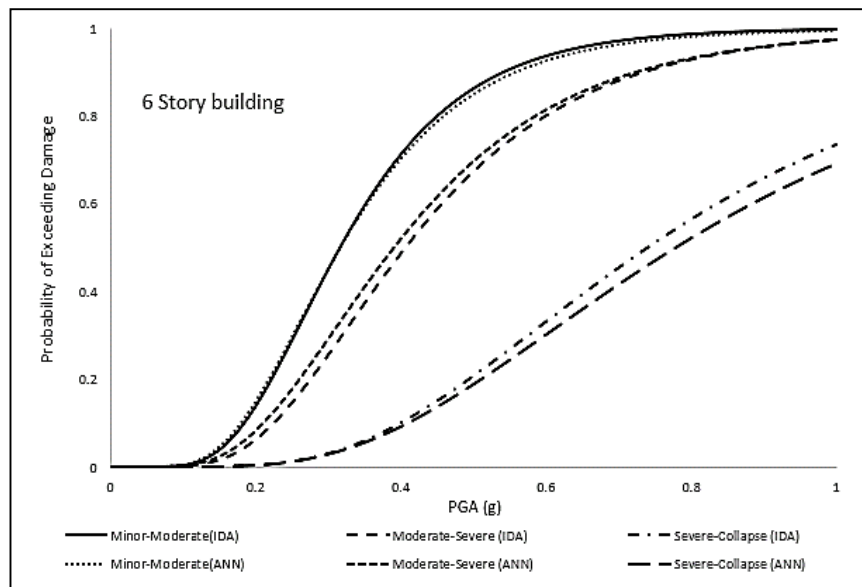
Figure 5.12: Comparison of the generated fragility curves by analysis and ANN
methods for six story building
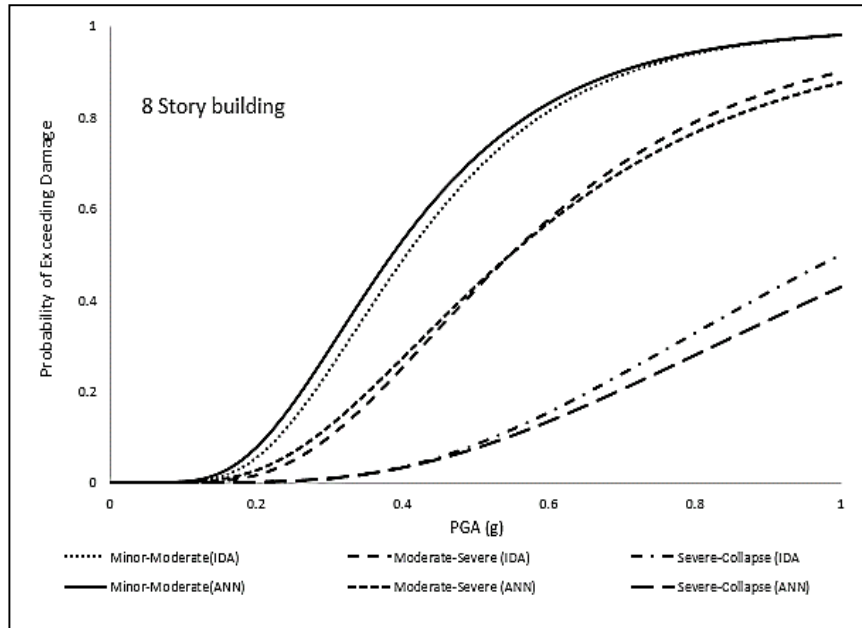
Figure 5.13: Comparison of the generated fragility curves by analysis and ANN methods for eight story building

Table 5.10: The used mean and standard deviation values for drawing the fragility curves for analysis and ANN methods

		Analysis (IDA)			ANN		
	Level	Minor-Moderate	Moderate-Sever	Sever-Collapse	Minor-Moderate	Moderate-Sever	Sever-Collapse
Mean	4	0.28	0.39	0.78	0.27	0.36	0.82
	6	0.35	0.45	0.83	0.35	0.44	0.88
	8	0.45	0.61	1.13	0.43	0.63	1.29
Standard Deviation	4	0.64	0.67	0.89	0.60	0.74	0.93
	6	0.66	0.69	0.91	0.64	0.65	0.93
	8	0.71	0.79	1.07	0.67	0.75	1.19

Also this network was used for prediction of other nonlinear dynamic responses of sample buildings. In this case, two responses of nonlinear analysis including; the top displacement and the base shear force were selected as output parameters of network. Again the network was trained for each of them and the forecast data was compared to actual data. The results showed that the network was able to predict these parameters with high precision. The comparison of actual value with forecast value and the regression of each data set for the top displacement and the base shear force data are shown in Figures 5.14-5.17, respectively.
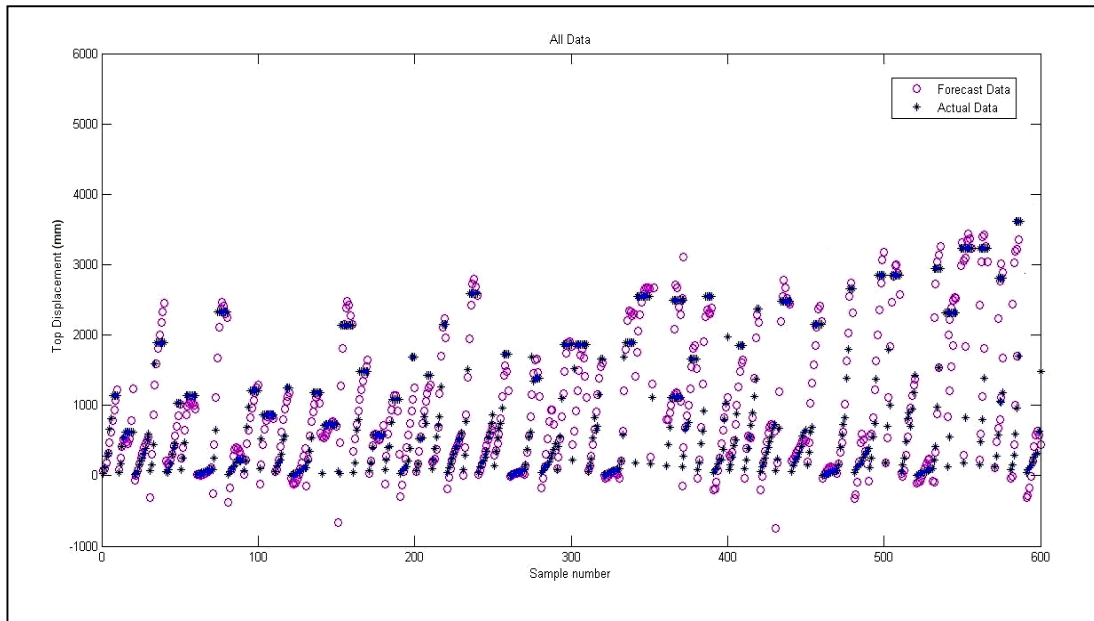
Figure 5.14: Comparison of actual and forecast values for the top displacement data
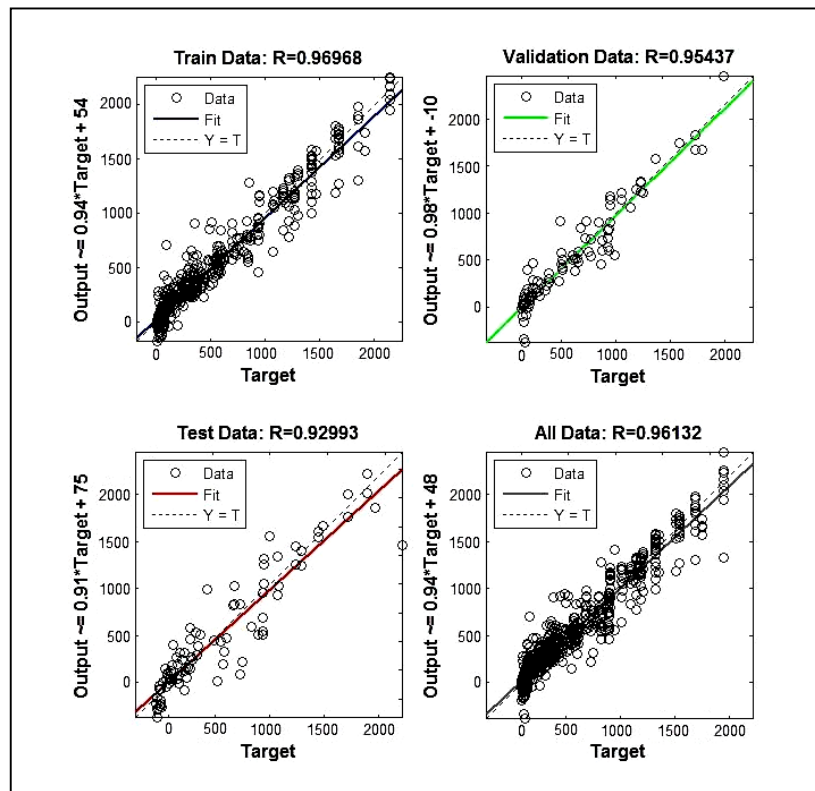
Figure 5.15: The regression and fit function for the top displacement data
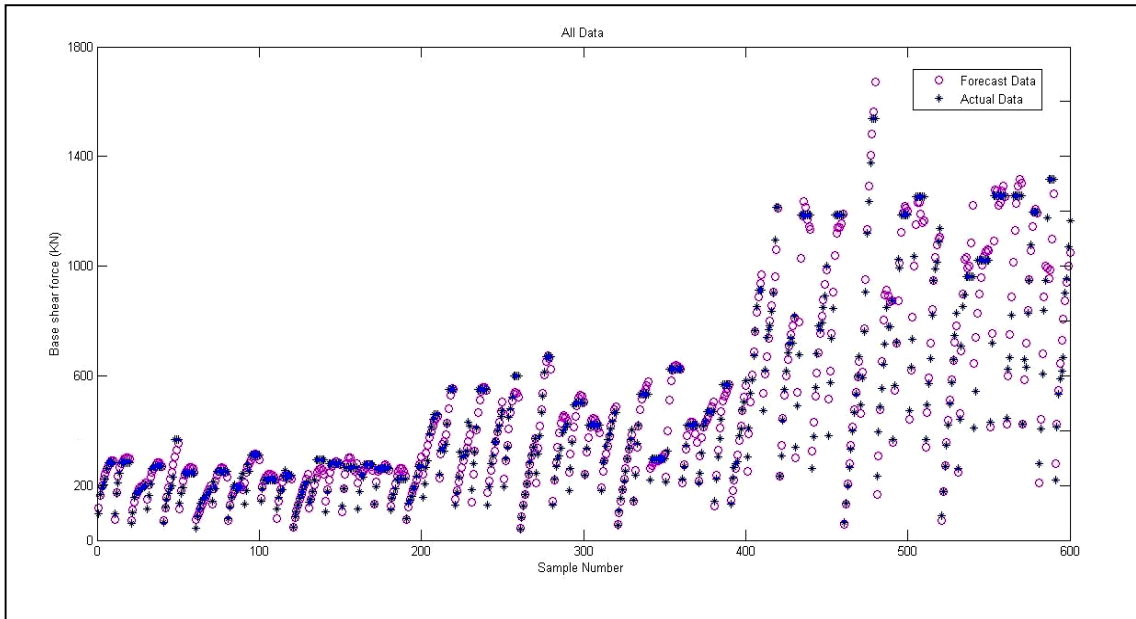
Figure 5.16: Comparison of actual and forecast values for the base shear force data
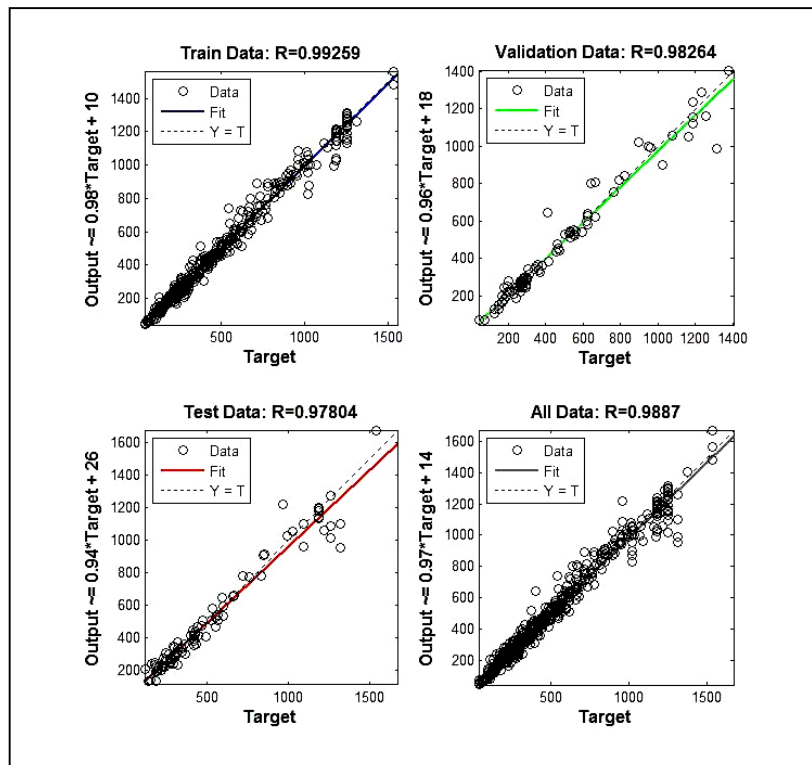
Figure 5.17: The regression and fit function for the base shear force data

5.2 Classification of damage

For classification of the imposed global damage, the SVM was used and classify the damage to three classes including; Repairable (Economic), Beyond Repair (Not Economic) and Loss of Building (Collapse). Indeed, this machine specified the discriminator (hyperplane) for each class with maximum margin between classes based on feature space of input data. For generation of discriminator, the kernel trick was used in SVM. In this study, four common kernel tricks were applied in SVM in order to find the best kernel function including; Linear Kernel Function, Polynomial Kernel Function, Gaussian Kernel Function and Sigmoid Kernel Function as presented in Table 5.11.

Table 5.11: Properties of kernel functions (Cortes and Vapnik (1995))

Kernel function	Expression	Comment
Linear	$K(x_i, x_j) = r + \alpha . x_i^T . x_j$	$\alpha > 0$
Polynomial	$K(x_i, x_j) = (r + \alpha . x_i^T . x_j)^p$	$\alpha > 0$
Gaussian	$K(x_i, x_j) = exp(-\frac{1}{2\sigma^2}\|x_i - x_j\|^2)$	$\sigma \neq 0$
Sigmoid	$K(x_i, x_j) = tanh(\beta_0 + \beta_1 . x_i^T . x_j)$	$\beta_1 > 0$

x_i, x_j are input vectors and r, α, σ, β_0 and β_1 are kernel parameters.

Therefore, the optimal hyperplane decision function is expressed as the following:

$$y = sign \left(\sum_{i=1}^{n} \alpha_i . y_i . K(x_i, x) + b \right). \tag{4.12}$$

5.2.1 Data generation

As mentioned in section 4.7.3, again the same data set which was obtained based on nonlinear time history analysis was used with the exception that in the output data,

the three classes based on the Park & Ang damage definition (see Table 3.4) was considered. The sample number of each class is shown in Figure 5.18.
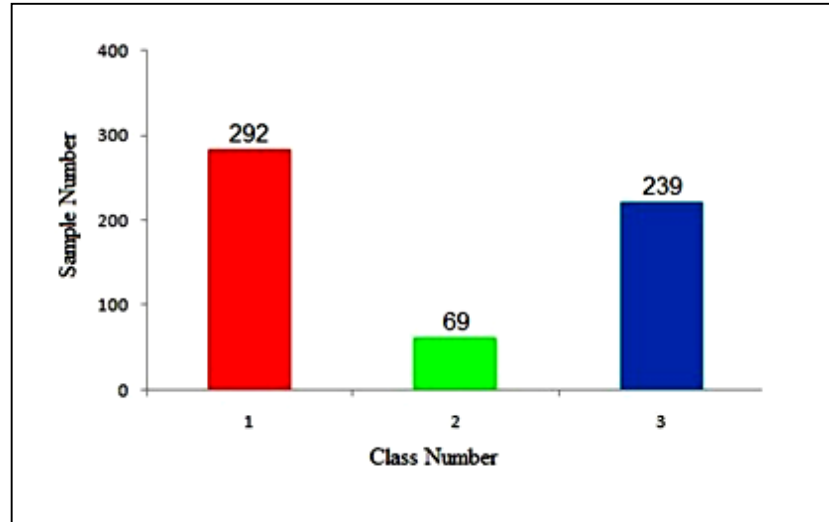
Figure 5.18: Distribution of data used in this study

In order to find the best kernel function, the total accuracy prediction scores of the test data were calculated. Also, the kernel parameters (p, r, α, σ, β_0 and β_1) and penalty factor (c) should be determined to reach the maximum margin between classes and the minimum classification error between real and predicted data. The amounts of p, r, α, β_0 and β_1 were obtained using trial and error. Also for the two remaining parameters (c and σ), the grid-search method was applied and the best values were selected automatically using Libsvm-3.17 (Chang and Lin, 2013) in the Matlab software. The results showed that 122, 129, 135 and 133 class labels from the total of 180 test-data class labels were correctly predicted for linear, polynomial (5 degree), gaussian and sigmoid functions, respectively. The total accuracy values of test data versus different kernel functions are shown in Figure 5.19. Therefore the gaussian function was chosen as an efficient kernel trick function.
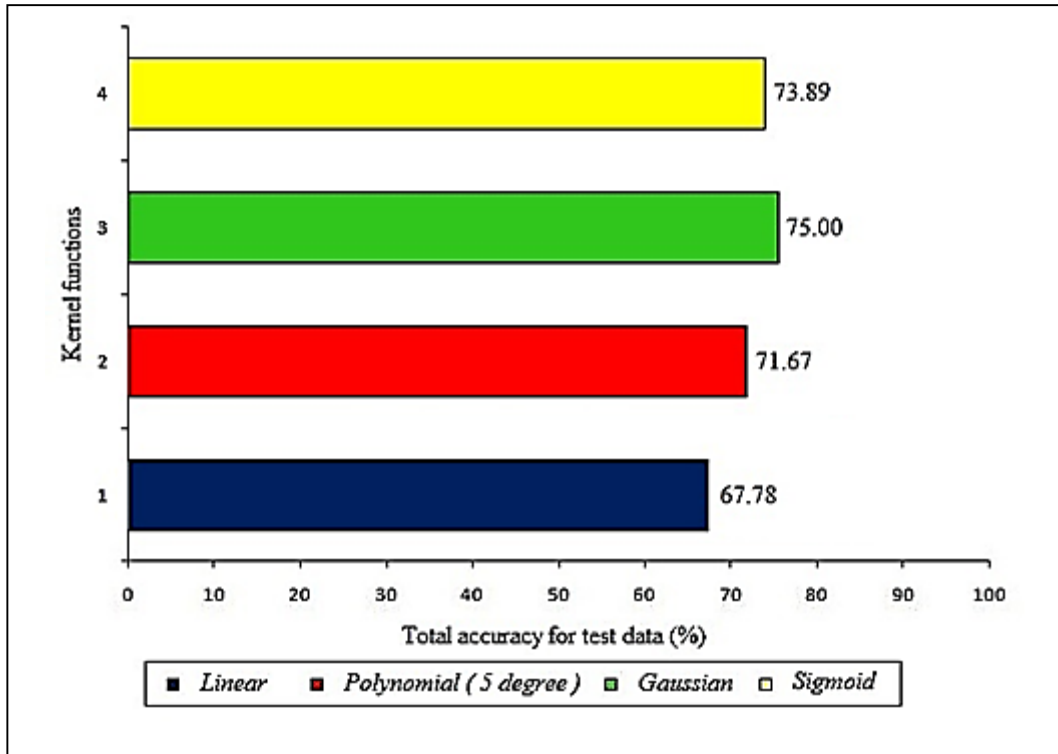
Figure 5.19: The total accuracy of test data for different kernel functions

5.2.2 M-SVM model

After determining the best activation function (Gaussian function), a set of normalized data which include 600 input data and each data containing thirteen elements were shuffled and then applied to this machine that 70% and 30% of the total data were used for training and testing process, respectively. Figure 5.20 shows the comparison of actual classes and predicted classes of the imposed global damage for train data, test data and all data of M-SVM. In this Figure, the hollow circles and stars are indicating the actual classes and predicted classes, respectively which if the classification be correctly done, then the hollow circles and stars will overlap together. The obtained results showed that the M-SVM has predicted the classes No. 1 and No. 3 with high precision. However, for class No. 2, this performance was poor. Because the number of data for this class compared to classes No. 1 and No. 3 was low,

110

therefore for this class, the M-SVM could not determine the proper margins based on feature of input data.

Figure 5.20: Comparison of the actual and predicted classes for train data, test data and all data of M-SVM

Also for evaluation of the obtained results from classified data, the confusion matrix is used and is defined as an error matrix or a contingency table to determine the performance of network. Each element of this matrix expresses the number of actual classes versus predicted classes. The structure of confusion matrix is shown in Figure 5.21.

$$
\begin{array}{ccc}
& \textit{Predicted} & \textit{Predicted} \\
& \textit{Class +} & \textit{Class -} & \textit{Total}
\end{array}
$$

$$
\begin{array}{cccc}
\textbf{\textit{Actual Class +}} & TP & FP & N \\
\textbf{\textit{Actual Class -}} & FN & TN & P \\
\textbf{\textit{Total}} & N & P &
\end{array}
$$

Figure 5.21: Sample of confusion matrix

whereas *TP* is a true positive observation, *TN* is a true negative observation. *FN* is a false negative since observation is an actual negative (-) but the classifier label is positive (+) and *FP* is a false positive since observation is an actual positive (+), nonetheless, the classifier label is negative (-). For assessment of this matrix, some parameters can be used which are shown in Table 5.12.

Table 5.12: Properties of parameters used for evaluation of confusion matrix

Name	Definition	Function
Sensitivity or Recall (SEN)	The rate of true positive	$SEN = \dfrac{TP}{TP + FN}$
Specificity (SPC)	The rate of true negative	$SPC = \dfrac{TN}{FP + TN}$
Precision (PRE)	The fraction of observations classified as positive that are actually positive	$PRE = \dfrac{TP}{TP + FP}$
Accuracy (ACC)	The proportion of the total number of predictions that are correct	$ACC = \dfrac{TP + TN}{TP + TN + FP + FN}$
Error	The proportion of the total number of predictions that are incorrect	$Error = \dfrac{FP + FN}{TP + TN + FP + FN}$
NPV	The negative predictive values	$NPV = \dfrac{TN}{TN + FN}$
PPV	The positive predictive values	$PPV = \dfrac{TP}{TP + FP}$

The confusion matrix for the train data, test data and all data of M-SVM are given

as below:

$$\text{Confusion matrix for the train data} = \begin{bmatrix} 188 & 5 & 19 \\ 19 & 14 & 19 \\ 19 & 3 & 134 \end{bmatrix}$$

113

Total accuracy= 80.00%, C=03.668, σ =17.910

$$\text{Confusion matrix for the test data} = \begin{bmatrix} 69 & 3 & 8 \\ 6 & 3 & 8 \\ 18 & 2 & 63 \end{bmatrix}$$

Total accuracy= 75.00%, C=13.4543, σ =22.242

$$\text{Confusion matrix for the all data} = \begin{bmatrix} 254 & 12 & 26 \\ 25 & 18 & 26 \\ 35 & 10 & 194 \end{bmatrix}$$

Total accuracy= 77.67%, C=2.3784, σ =14.424

Based on extracted confusion matrices, the amounts of SEN, SPC, PRE, ACC, Error, NPV and PPV for each class and each set of data are presented in Table 5.13. The obtained results from these parameters showed that the performance of class No. 1 and No. 3 are very close and their PRE's are equal to 86.99 % and 81.17 %, respectively. Also, the low value of PRE for class No. 2 represents inaccuracies for classification of this class.

Table 5.13: The SEN, SPC, PRE, ACC, Error, NPV and PPV values for each class

	Train Data			Test Data			All Data		
	Class 1	Class 2	Class 3	Class 1	Class 2	Class 3	Class 1	Class 2	Class 3
SEN (%)	83.19	63.64	77.91	74.19	37.50	79.75	80.89	45.00	78.86
SPC (%)	87.63	90.45	91.13	87.36	91.62	80.20	86.71	90.89	87.29
PRE (%)	88.68	26.92	85.90	86.25	17.65	75.90	86.99	26.09	81.17
ACC (%)	85.24	89.05	85.71	80.56	89.14	80.00	83.67	87.83	83.83
Error (%)	14.76	10.95	14.29	19.44	10.86	20.00	16.33	12.17	16.17
NPV (%)	81.73	97.83	85.61	76.00	96.84	83.51	80.52	95.86	85.60
PPV (%)	88.68	26.92	85.90	86.25	17.65	75.90	86.99	26.09	81.17

5.2.3 MM-SVM model

For generation of MM-SVM, a one-layer feed-forward MLP neural network (Chiddarwar and Babu, 2010; Yilmaz and Kaynar, 2011) was used at first level, then the output of this network was applied to M-SVM in form of input data. This combined ANN was named MM-SVM and is shown in Figure 5.22.
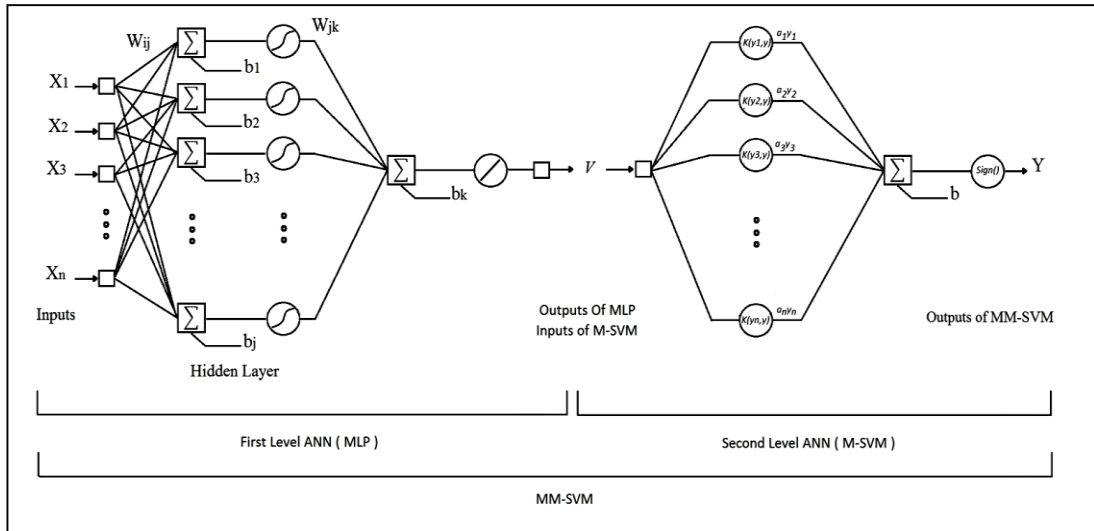
Figure 5.22: The architecture of combined MLP with M-SVM (MM-SVM)

At the first level of MM-SVM, 600 input data was applied to MLP neural network. For training process, the Levenberg–Marquardt back propagation algorithm was employed to update the weights and bias terms of the MLP network. Therefore, using this network led to a change in the primal data space from the thirteen dimensions to one dimension. The MLP network consists of thirteen neurons in the input layer, optimum neurons in the hidden layer and one neuron in the output layer. The gaussian and linear activation functions were used for the hidden layer and the output layer of the MLP network, respectively. In addition, the number of hidden layer neurons was determined based on the minimum test error and is obtained equal to thirty.

In the training process of MLP, the network stopped after 85 iterations with MSE and gradient equal to 0.0520 and 0.0266, respectively. In addition, the best validation performance was 0.19188 at epoch 79. The values of RMSE, MSE, R, μ and σ are presented in Table 5.14.

Table 5.14: The RMSE, MSE, R, μ and σ values for each set of data

	Train Data	Validation Data	Test Data	All Data
RMSE	0.23761	0.43804	0.37704	0.29938
MSE	0.05646	0.19188	0.14216	0.089627
R	0.96675	0.88962	0.93072	0.945832
μ	-0.015535	-0.065719	-0.043856	-0.0075951
σ	0.23739	0.43551	0.37658	0.29953

As seen in Table 5.14, the RMSE and MSE variables in validating cases are greater than variables in training and testing cases. Also the amount of Rs ranged between 0.88962 and 0.96675. Figure 5.23 compares the real output values and the predicted values of all data. The most variation of errors for all data set were determined between -0.5 and +0.5 which successfully represents the network damage prediction values with high accuracy. The regression and fit function for the train, validation, test and all data are shown in Figure 5.24. The high value of R (around 0.95) indicates a good relationship between predicted values and actual values for the total response in the MLP model. Moreover, the histogram of error for all data is presented in Figure 5.25. The concentration of the bins error around the zero line with mean -0.0075951 and standard deviation 0.29953 for all set of data represents a good performance of this network.
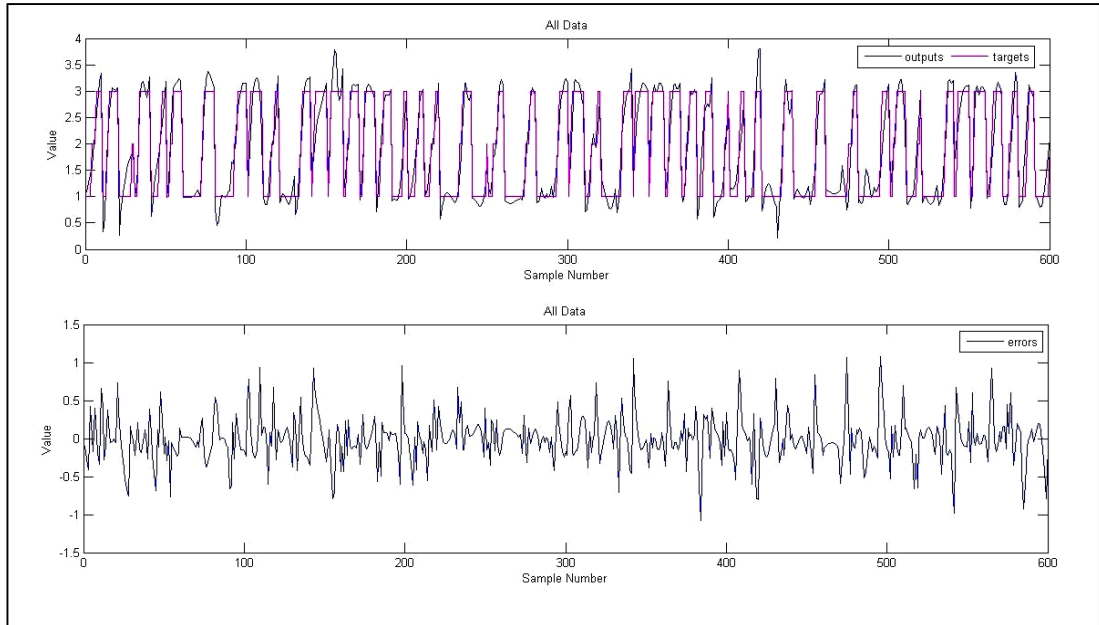
Figure 5.23: Comparing the real and predicted values
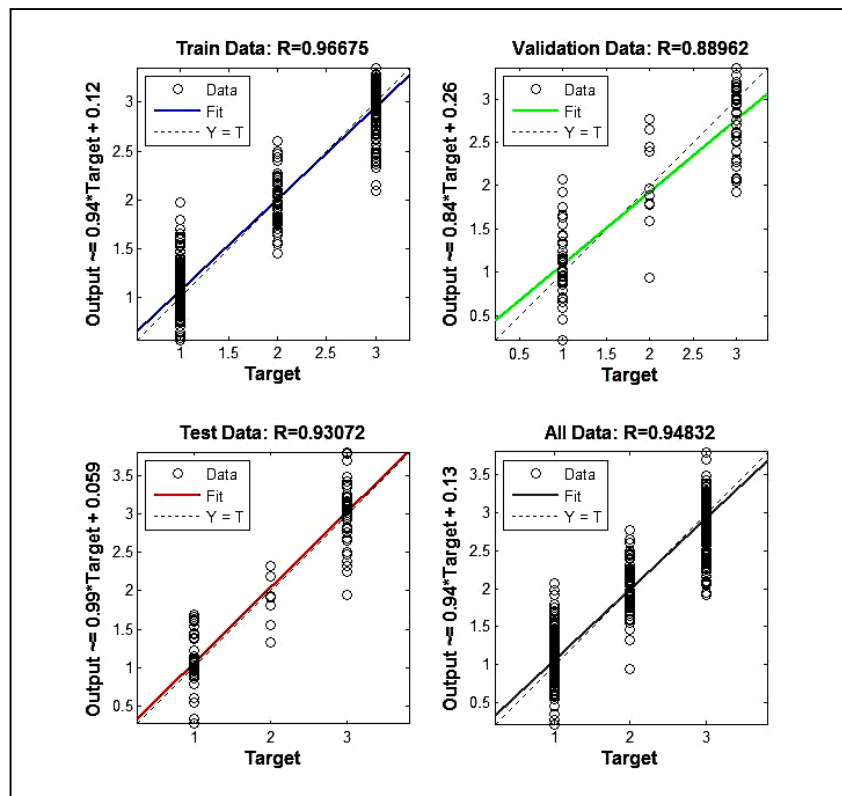
Figure 5.24: The regression and fit function for each set of data

118
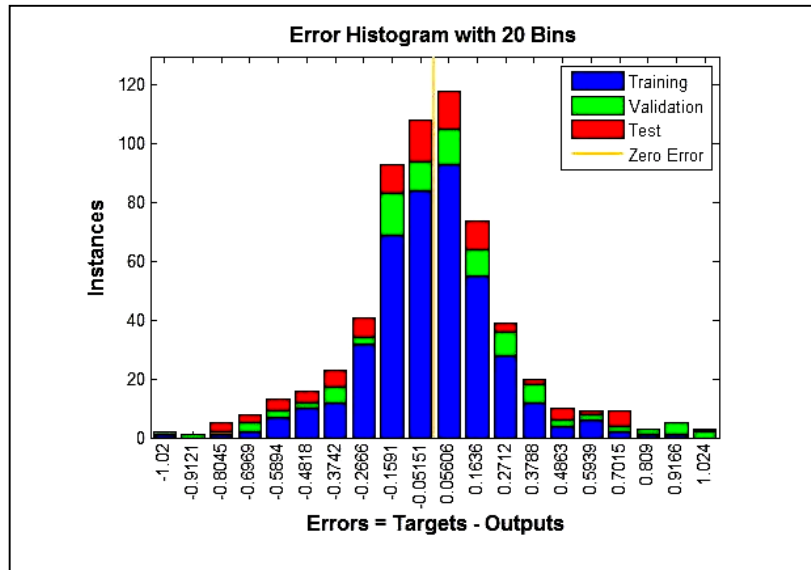
Figure 5.25: The error histogram for all data

At the second level of MM-SVM, the obtained outputs of the first level (MLP network) were applied to the M-SVM as input data. This set includes 600 input data and each data consists of only one element. Figure 5.26 shows the comparison of the actual classes and the predicted classes of the imposed global damage for the train data, test data and all data of MM-SVM. For all classes, the results showed that the MM-SVM has predicted the classification of global damage with high accuracy compared to M-SVM. Indeed, the reduction in feature space of input data and creating high relation between the input and output data by the MLP neural network led to determining more precisely of margins for each class by the M-SVM.
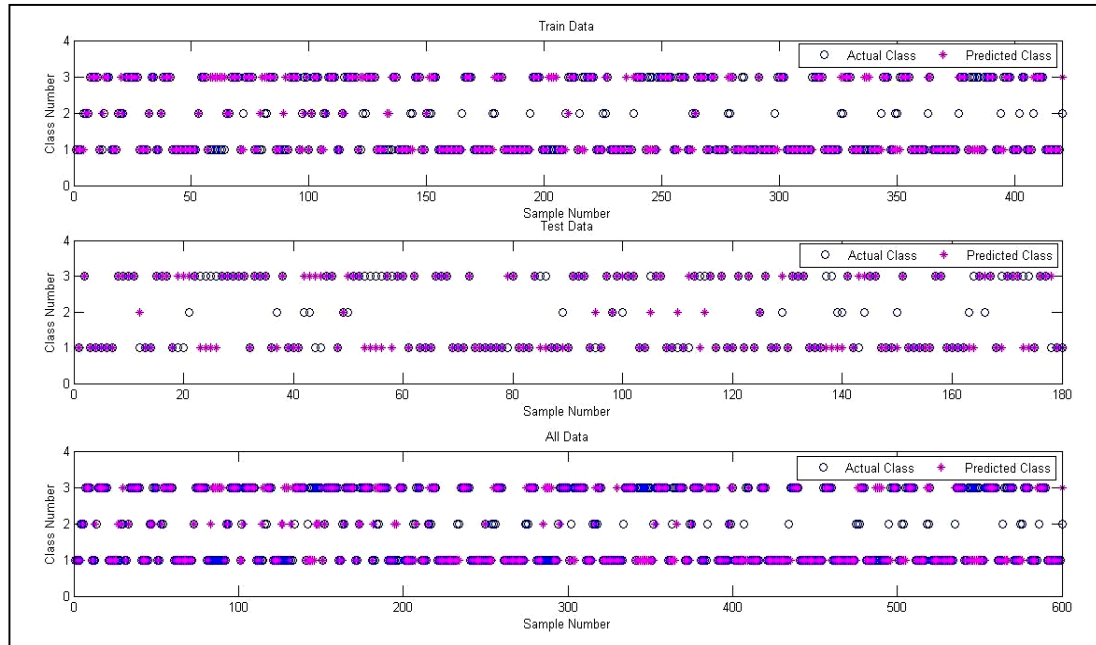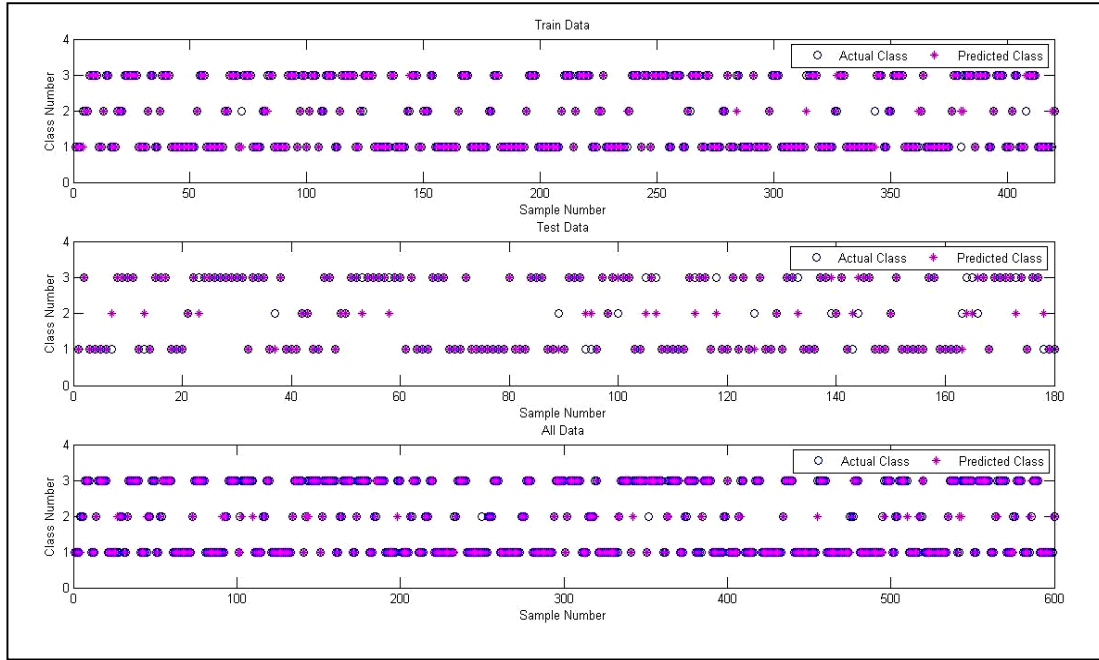
Figure 5.26: Comparison of the actual and predicted classes for train data, test data and all data of MM-SVM

The confusion matrix for the train data, test data and all date of M-SVM are given as below:

$$\text{Confusion matrix for the train data} \ = \begin{bmatrix} 208 & 4 & 0 \\ 3 & 44 & 5 \\ 0 & 4 & 152 \end{bmatrix}$$

Total accuracy= 96.19 %, C=5.6569, σ =0.7071

$$\text{Confusion matrix for the test data} \ = \begin{bmatrix} 74 & 6 & 0 \\ 4 & 9 & 4 \\ 0 & 11 & 72 \end{bmatrix}$$

Total accuracy= 86.11 %, C=1.17678, σ =0.2973

$$\text{Confusion matrix for the all data} = \begin{bmatrix} 282 & 10 & 0 \\ 7 & 53 & 9 \\ 0 & 14 & 225 \end{bmatrix}$$

Total accuracy= 93.33 %, C=181.0193, σ =0.0526

Based on extracted confusion matrices from MM-SVM, the amounts of SEN, SPC, PRE, ACC, Error, NPV and PPV for each class and each set of data are presented in Table 5.15. The maximum and minimum of error were obtained equal to 13.89% and

120

1.67% for class No. 2 and class No. 1, respectively. Also for all data, the PRE values for class No. 1, class No. 2 and class No. 3 were extracted equal to 96.58%, 76.81% and 94.14% respectively.

Table 5.15: The SEN, SPC, PRE, ACC, Error, NPV and PPV values for each class

	Train Data			Test Data			All Data		
	Class 1	Class 2	Class 3	Class 1	Class 2	Class 3	Class 1	Class 2	Class 3
SEN (%)	98.58	84.62	96.82	94.87	34.62	94.74	97.58	68.83	96.15
SPC (%)	98.09	97.83	98.48	94.12	94.81	89.42	96.78	96.94	96.17
PRE (%)	98.11	84.62	97.44	92.50	52.94	86.75	96.58	76.81	94.14
ACC (%)	98.33	96.19	97.86	94.44	86.11	91.67	97.17	93.33	96.17
Error (%)	1.67	3.81	2.14	5.56	13.89	8.33	2.83	6.67	3.83
NPV (%)	98.56	97.83	98.11	96.00	89.57	95.88	97.73	95.48	97.51
PPV (%)	98.11	84.62	97.44	92.50	52.94	86.75	96.58	76.81	94.14

The above obtained results for all three classes showed that the MM-SVM model to be highly suited to classification of global damage for R/C wide-beam buildings and provide reference for future seismic assessment of this building's type.

5.3 Case study (Kutup building)

In this section, an existing R/C slab column frame with wide beams and rectangular columns was considered as the case study. This building is constructed in Famagusta city and still in use as a residential building. This building is shown in Figure 5.27. It has seven floors which the height of the first and the second stories are 2.9m and 3.6m,

respectively. Also the rest of stories heights are 2.85m. The building dimensions are 14.4m and 16.75m in X and Y directions, respectively. For beams and columns, different sections were used in each story. The plans and details of model are mentioned in appendix D. For nonlinear time history analysis, IDARC software was used. In modeling, the amount of the live load and dead load were considered 200 kg/m^2 and 500 kg/m^2, respectively. The compressive strength of concrete, yield and ultimate strength of steel were considered as 15MPa, 220MPa and 300MPa, respectively. Whereas the first mode period in Y direction is more that X direction, the building was excited only in weaker direction.
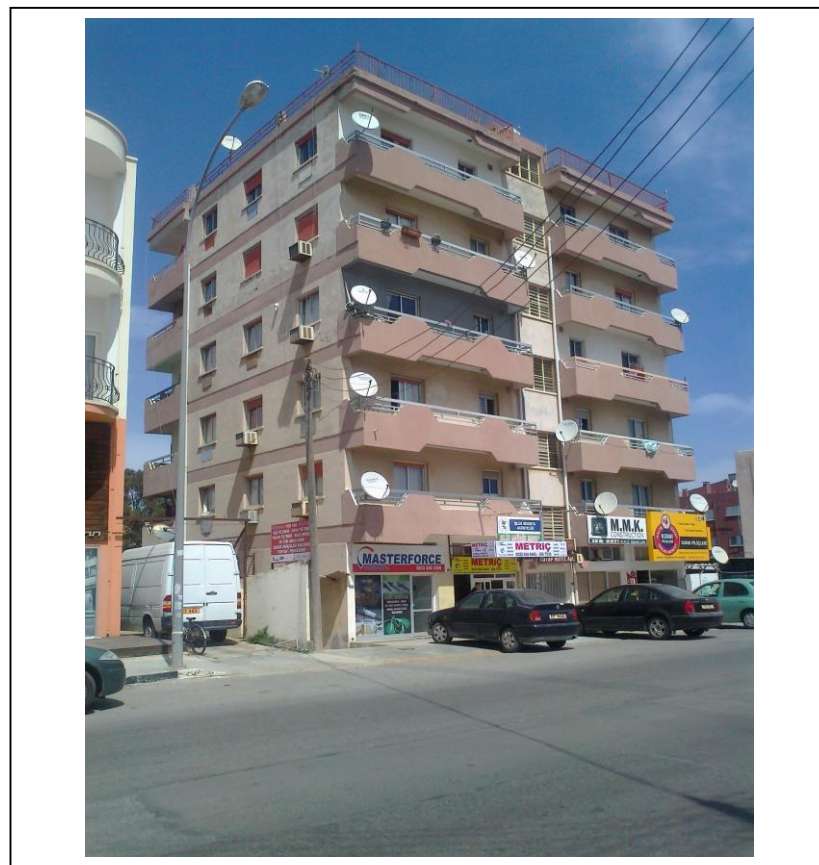
Figure 5.27: The Kutup Building (case study)

5.3.1 Classical method (IDA)

Based on proposed mythology that presented and mentioned in Figure 3.11, the fragility curves were derived for three different damage levels using the Park & Ang limit states criteria (Table 3.3). Furthermore, the log-normal cumulative distribution function were applied as probability function. Figure 5.28 illustrates the obtained fragility curves for each limit states.
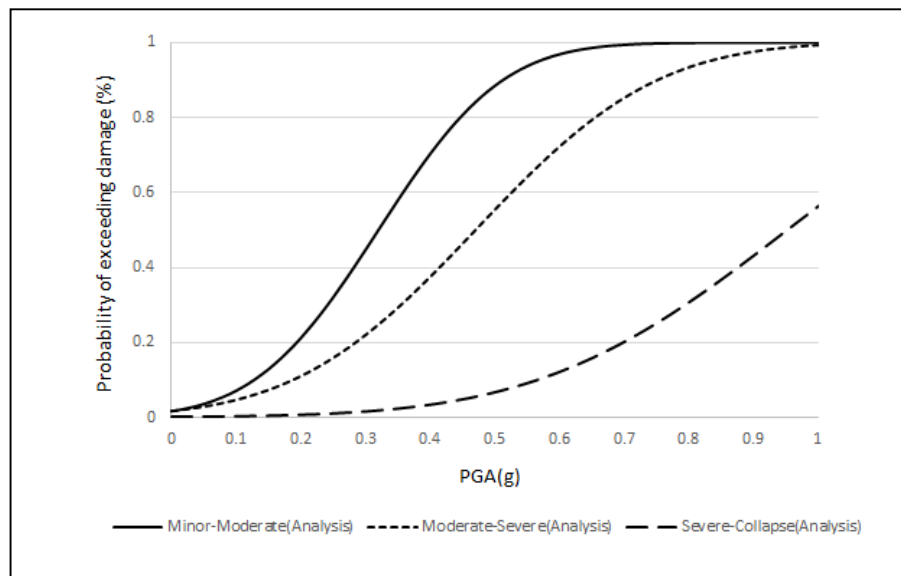
Figure 5.28: The fragility curves for case study building (classical method)

5.3.1 Neural network Method (ANN)

Before running the ANN analysis, the input data should be prepared for MLP neural network. This data consists of building dimension and geometry of the structural elements. Table 5.16 shows the amount of these parameters. Also for ground motion indices, the same values were considered. For training of MLP neural network, 70% and 30% of all obtained data from nonlinear time history analysis of four, six and eight story models were considered and used for train and validation progress, respectively.

Table 5.16: The amount of structural parameters

Parameters	Value of parameters
h/b	1.44
b/d	0.86
N	7
B	5
M (m)	3.6
I_C (m^4)	0.0349
I_B (m^4)	0.00495
B_C (cm^2)	494.74
B_B (cm^2)	222.8

In training process, the network stopped at 24 iterations with gradient and MSE equal to 0.0133 and 0.0377, respectively. Also the best validation performance was 0.0537 and occurred at epoch 18. Figure 5.29 shows the process of network training and error histogram for all data. The regression and fit function for train, validation, and all data are shown in Figure 5.30.
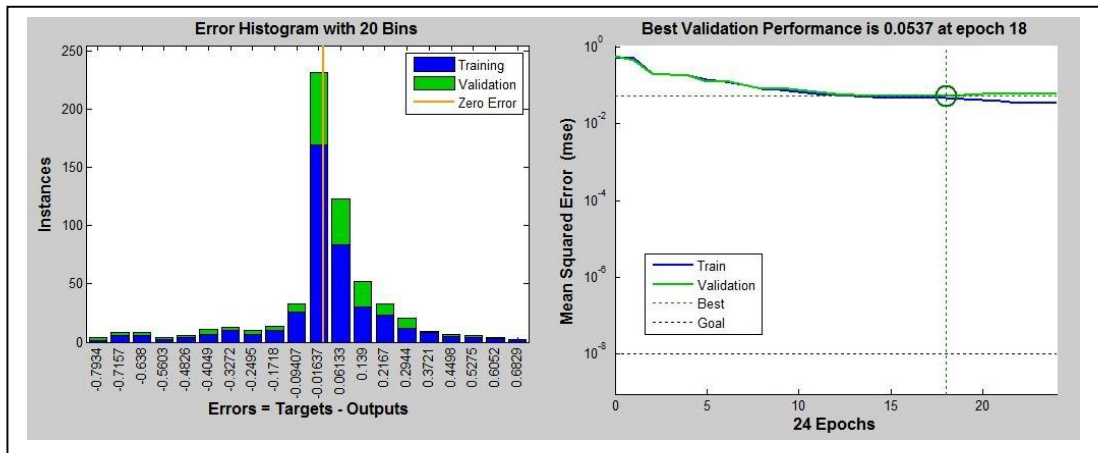
Figure 5.29: The network training process and error histogram
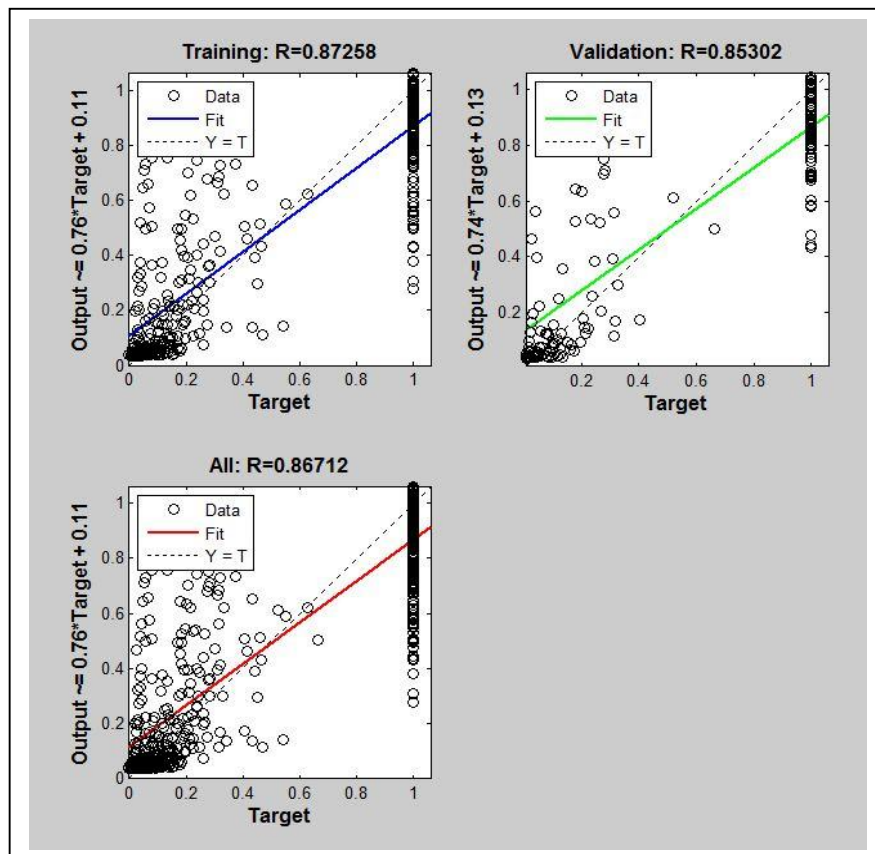
Figure 5.30: The regression and fit function for each set of data

After training of the network, the test data (input data from case study) was applied to network for test progress. The amounts of error between classical method and ANN are shown in Figure 5.31. Also by using the obtained results from ANN, the fragility curves were drawn. Figure 5.32 shows the obtained fragility curves for each limit state. Also the compared fragility curves based on classical method and ANN are shown in Figure 5.33.

Figure 5.31: The error value for test data
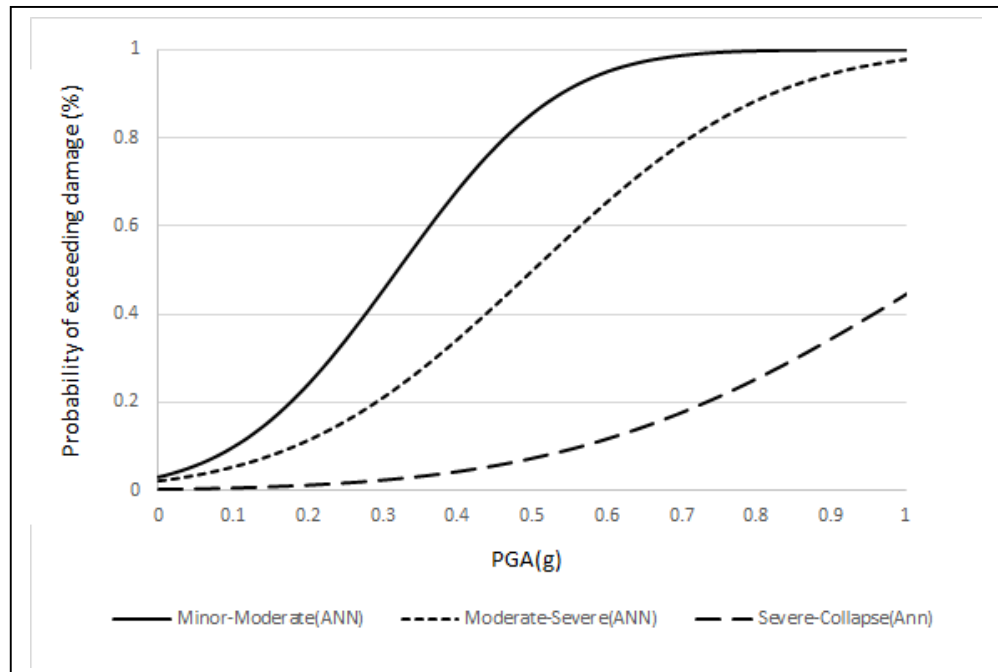
Figure 5.32: The fragility curves for case study building (ANN method)
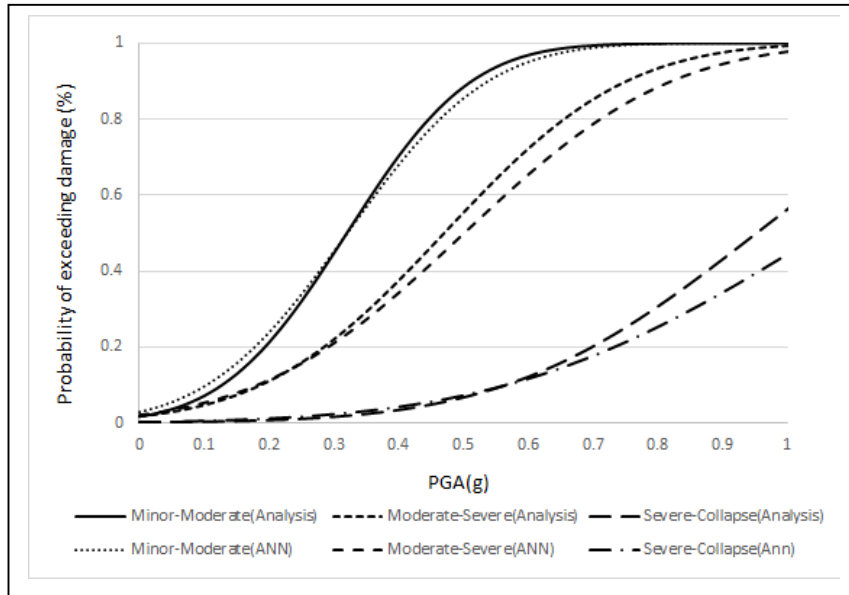
Figure 5.33: Comparison of the generated fragility curves by analysis and ANN methods for case study building

\

Chapter 6

DISCUSSION

In this study, the obtained fragility curves from incremental nonlinear time history analysis for these sample buildings represented that the vulnerability for four story building was more than six and eight story buildings. Also, the obtained responses due to Duzce-Turkey record with PGA equal to 0.5g showed that the first failure was happened in beams and then continued in columns. Furthermore, the amounts of damages for upper level beams were more than lower level beams and this process was inversed for story columns. The story displacement and the story shear were increased and decreased with number of levels, respectively. Also the analysis showed that the modal participation factor in first mode is much higher than other modes which represents the first mode is dominant. Furthermore, the relative modal weight for sample buildings in first mode was changing between 70% and 80%. In the following, the process of plastic hinges for one beam and two columns with different section areas were drawn and showed that although the first plastic hinges occurred in beams and then expanded in columns (The principle of the weak beam - strong column), but the amount of dissipated energy in beams were much less than columns.

In order to determine the limit states for this type of buildings and compare with the values which are suggested by FEMA 356 (2000), the global damage was calculated based on maximum inter-story drift damage index and the IDA curves were drawn for each sample. The obtained results showed that the damage criteria for IO and CP were 1% and 5%, respectively which is one percent more than FEMA 356

(2000) in CP damage level and it indicates that these type of buildings have more deformation in comparison with normal buildings.

According to this deformation, the effect of P-delta for this type of buildings is significant. Therefore, in section 4.4, the effect of P-delta in fragility curves was evaluated and the obtained curves showed that this effect was increased with number of story and performance levels. Table 6.1 shows the RMSE values for with and without P-delta effect cases. Based on this table, the RMSE values ranged between 7% up to 28%.

Table 6.1: The difference between with and without P-delta effect cases by RMSE for each building (%)

Story No.	Minor - Moderate	Moderate - Severe	Severe - Collapse
4	6.87	10.05	12.19
6	10.95	16.17	20.16
8	19.41	20.13	28.29

In section 4.5, the effect of 2D models on fragility curves were compared with 3D models. Whereas the IDARC software can model 2D and also 3D models, but only can analyze in one direction, therefore many researches were performed on frame models instead of 3D models. Always there is a question whether a 2D model can express almost all features of a 3D model. For this purpose, 2D models were selected and the obtained fragility curves were compared with 3D models. Table 6.2 shows the RMSE values for 2D and 3D cases. Based on this table, the 2D models have less capacity than the 3D models. Also, the RMSE values between 2D and 3D curves ranged between 15% up to 30%. In fact, a 2D model can be used as a convenient

alternative for a 3D model when all the frames of 3D model were equal in terms of size, dimension and loading (neglect torsion effect).

Table 6.2: The difference between 2D and 3D models by RMSE for each building (%)

Story No.	Minor - Moderate	Moderate - Severe	Severe - Collapse
4	16.73	19.11	37.59
6	14.34	11.94	27.89
8	20.34	17.94	29.76

In section 4.6, the effect of aftershock was evaluated. Whereas, this effect has been ignored almost in all codes and also there is not enough time to repair the damaged structural members after the main shock, therefore the aftershocks effect should be taken into account. In this study, based on lack of data for Famagusta region, only five earthquakes which contain the aftershocks effect were evaluated. By considering the PGA ratio of aftershock to main shock as an index, the results showed that for low ratios, the damage values had not changed. Whereas, for ratios around 1.5, the amount of damages under aftershock was significant. Table 6.3 shows the amount of global damage for main shock and aftershock cases. The obtained damage values of this data with aftershock effect showed that the damage is between 2 to 8 times more than only main shocks. Also it should be considered that the amount of damage under main shocks were less than 0.1 and it cannot be generalized to all levels of damage.

Table 6.3: The global damage under main shock and main shock along aftershock cases

Earth quake Name	Level	Damage		Increasing proportion
		Main shocks	**Aftershocks**	
Chalfant Valley	4	0.042	0.10	2.38
	6	0.029	0.067	2.31
	8	0.013	0.036	2.78
Superstitn Hills	4	0.033	0.265	8.03
	6	0.027	0.174	6.40
	8	0.022	0.13	5.90

In section 5.1, the ANNs were used in order to predict and classify the building damage. In fact, the main aim was to generate the new method for rapid evaluation of buildings vulnerability without any analysis. At the first, a MLP neural network was applied to determine the effective ground motion parameters. As follows, with considering thirteen structural and ground motion parameters, the network was trained and the amount of damages were obtained for each samples and led to drawn fragility curves. Table 6.4 shows the RMSE values for ANN and classical method (IDA). Comparing the obtained curves from ANN and IDA curves showed that the RMSE values were changed between 2% to 4% which is expressing the high performance of network.

Table 6.4: The difference between classical analysis and ANN methods by RMSE for each building (%)

Story No.	Minor - Moderate	Moderate - Severe	Severe - Collapse
4	2.04	4.28	4.01
6	0.68	1.90	2.70
8	2.42	1.71	3.26

Also the MLP network was applied for prediction of the top displacement and the base shear force of samples and the regression value of all data were obtained around 96% and 99 %, respectively which represent high accuracy in predicting of these parameters.

In section 5.2, the classification of building global damage was done using SVM. Whereas, the percentage of input data for class No. 1, class No. 2 and class No. 3 were equal to 48.67%, 11.5% and 39.83% of all data, respectively, the M-SVM model showed a weak performance for classification of class with minimum members (class No. 2). In fact, the SVM couldn't realize the suitable margins for this class. Whereas, the MM-SVM model was able to predict 44, 9 and 53 class label from the set of 52, 17 and 69 considered class label of the train, test and all data cases for class No. 2. Indeed, using of the MLP model in first level of MM-SVM led to a reduction in the dispersion and complication of feature space for input data and based on this reason, in the second phase, the M-SVM was able to determine the margins for each class with high precision. Table 6.5 compares the ACC-value for M-SVM and MM-SVM models. The results showed that the MM-SVM classifier improves the performance in terms of recognition rate and error rate significantly compared to M-SVM model for one classification task of global damages.

Table 6.5: Comparing the ACC-value for M-SVM and MM-SVM

Data Set	M-SVM (%)	MM-SVM (%)	Improvement (%)
Train data	80.00	96.19	16.19
Test data	75.00	86.11	11.11
All data	77.67	93.33	15.66

In section 5.3, in order to verify the presented methodology in this thesis, a case study model was considered and evaluated. In training process, the MLP network did not have any experience of test data. The RMSE values for these two methods are shown in Table 6.6.

Table 6.6: The difference between classical method and ANN by RMSE for case study building (%)

Damage Level	Minor-Moderate	Moderate-Severe	Severe-Collapse
	1.848	3.984	4.282

Table 6.6 shows that the amounts of RMSE between classical method and ANN for Minor-Moderate, Moderate-Severe and Severe-Collapse levels are 1.848%, 3.984% and 4.282%, respectively which presents an increasing trend. Also these results show that the presented methodology in this research can be used with high precision.

Chapter 7

CONCLUSION

In this study, two main objectives were pursued. First, evaluation of seismic vulnerability of wide-beam R/C buildings which were built in the Mediterranean area and also available and still in used in North Cyprus. Second, using ANNs as an alternative and rapid evaluation method for prediction and classification of imposed damages with high precision. The following conclusions were obtained from this investigation:

- Using obtained fragility curves, the vulnerability of buildings decreases with the number of stories.

- The process of damage assessment showed that the first failure was occurred in beams and then continued in columns. Furthermore, the amounts of damages for the upper level beams were more than lower level beams and this process was inversed for columns.

- The modal participation factor for the first mode was much than the other modes which represents the first model is dominant. Also, the relative modal weight for four, six and eight story buildings were obtained around 79.5%, 74% and 72%, respectively.

- By considering maximum inter-story drift as damage index, the obtained IDA curves showed that the damage criteria for IO and CP damage levels were obtained equal to 1% and 5%, respectively which is 1% more than FEMA 356 (2000) criteria for CP damage level.

- The fragility curves for without considering the P-delta effect case showed that this factor is impressive for this type of buildings. Also, the RMSE values represented the difference around 6% up to 28% between with and without P-delta effect cases.

- Comparison the fragility curves for 2D and 3D models showed that the 2D models cannot be used as suitable alternative for 3D models. Also, the RMSE values represented the difference around 15% up to 30% between 2D and 3D cases.

- For high PGA ratio (around 1.5) of main shock to aftershock showed that the effect of aftershocks is significant. The obtained damage values for this range of PGA ratio represented that the increasing of damage between 2 up to 8 times more than single main shocks. Also in this study, it should be considered that the amount of damage under main shocks were less than 0.1 and it cannot be generalized to all levels of damage.

- The effective ground motion parameters were identified based on ANNs. The observed result from ANNs showed that the minimum values of R were obtained for PGA/PGV, dominant frequency, PGV/PGD and PGV parameters, respectively which indicated the network is sensitive to these indices. Moreover, the ineffective parameters consist of PGA, fault line distance, effective time duration, PGA/PGD and PGD, respectively. Also it should be considered that since the sample frame was in intermediate period region, the velocity controlled responses are more effective among the earthquake parameters. The amount of obtained R from two networks consist of all input data (nine parameters) and four sensitive data (four parameters) were obtained equal to 0.85220 and 0.84514, respectively which is shown that around 0.8% difference between them. Therefore for buildings in this period range, it is suggested to use these effective parameters which are sufficiently enough for evaluation of vulnerability instead of considering more ground motion characteristics.

- For training the network, ten different activation functions were examined in order to reach the optimum number of hidden layer neurons and the best function for network training process. The results showed that among these functions, hyperbolic tangent sigmoid activation function with thirty neurons in hidden layer had higher accuracy. Also, for this type of data, using hard-limit transfer function and symmetric hard-limit transfer function are not recommended.

- For prediction of the damage values, the MLP neural network was used with thirteen neurons in input layer, thirty neurons in hidden layer and a neuron in output layer. The amounts of R were obtained around 96%, 90%, 88% and 94% for train, validation, test and all data, respectively.

- Comparison of damage predicted by IDA and ANN showed that this network is a more efficient and time saving way for vulnerability evaluation of R/C wide-beam buildings only using limited parameters of structural geometric and ground motion characteristic. In addition, the high performance of network represented the selected parameters are able to establish a good relation between the structural and ground motion parameters (input data) and damage values (output data).

- The MLP network also was applied for prediction of the top displacement and the base shear force of sample buildings. The results showed that the network was very efficient and it was predicted these parameters with high precision.

- For classification of the imposed seismic damage under earthquake loads two networks were used. In order to find the best kernel trick, four different kernel functions were applied including; linear function, polynomial function (5 degree), Gaussian function and sigmoid function and these functions were evaluated using maximum accuracy of test data. The results showed that the Gaussian function had the maximum accuracy and it was employed as an efficient kernel trick function.

- Comparing the classification results of the M-SVM and MM-SVM showed that the total accuracy of MM-SVM is more than M-SVM. Also for class No. 2 (class with the lowest member), the obtained values of PRE indicated that the MM-SVM was predicted the label of this class with high efficiency towards the M-SVM. Thus, the MM-SVM was identified as an efficient network for classification of the imposed global damage under earthquake loads and it can be used for similar R/C buildings solely by selecting the structural geometric and ground motion parameters. In addition, this method of damage classification can be used by the insurance companies because it is easy and fast.

-Comparison between obtained fragility curves by classical method and ANN for case study model showed that using neural network for predicting the damage level of buildings can be applied as an alternative method with fast, easy and high accuracy capability instead of classical method. Also it should be considered that a good and available database, an appropriate ANN with compatible structure and another effective parameters have crucial roles in this process.

REFERENCES

Aboutaha, R.S., & Machado, R.I. (1999). Seismic resistance of steel-tubed high-strength reinforced-concrete columns. *Journal of Structural Engineering*, 125(5), 485-494.

ACI-ASCE Committee 352. (1991). Recommendations for design of beam-column joints in monolithic reinforced concrete structures. American Concrete Institute, Farmington Hills, MI.

ACI Committee 318-83. (1983). Building code requirements for structural concrete (ACI318-83) and commentary (ACI318R- 83). American Concrete Institute, Farmington Hills, MI.

ACI Committee 318-89. (1989). Building code requirements for structural concrete (ACI318-89) and commentary (ACI318R- 89). American Concrete Institute, Farmington Hills, MI.

ACI Committee 318-95. (1995). Building code requirements for structural concrete (ACI318-95) and commentary (ACI318R- 95). American Concrete Institute, Farmington Hills, MI.

ACI Committee 318-99. (1999). Building code requirements for structural concrete (ACI318-99) and commentary (ACI318R- 99). American Concrete Institute, Farmington Hills, MI.

ACI Committee 318-05. (2005). Building code requirements for structural concrete (ACI318-05) and commentary (ACI318R- 05). American Concrete Institute, Farmington Hills, MI.

ACI Committee 318-08. (2008). Building code requirements for structural concrete (ACI318-08) and commentary (ACI318R- 08). American Concrete Institute, Farmington Hills, MI.

Adeli, H., & Panakkat, A. (2009). A probabilistic neural network for earthquake magnitude prediction. *Journal of Neural Networks*, 22, 1018-1024.

Allahabadi, R., & Powell, G.H. (1988). DRAIN-2DX User Guide. Technical Re No. UCB/EERC-88-06, Earthquake Engineering Research Center, Univ. of California, Berkeley, CA.

Arjun, R.C., & Kumar A. (2011). Neural network estimation of duration of strong ground motion using Japanese earthquake records. *Soil Dynamics and Earthquake Engineering*, 31, 866-872.

Arslan, H. M. (2010). An evaluation of effective design parameters on earthquake performance of R/C buildings using neural networks. *Journal of Engineering Structure,* 32, 1888-1898.

Babaleku, M., & Pojani, N. (2008). Fragility evaluation of existing typified school buildings in Albania. *Journal of Acta Geodaetica et Geophysica Hungarica*, 43, 309-325.

Banon, H., & Veneziano, D. (1982). Seismic safety of reinforced members and structures. *Earthquake Engineering and Structural Dynamics*, 10(2), 179-193.

Borghi, A., Aoudia, A., Riva, E.M. R., & Barzaghi, R. (2009). GPS monitoring and earthquake prediction: A success story towards a useful integration. *Journal of Tectonophysics.* 465(1-4), 177-189.

Buratti, N., Ferracuti, B., & Savoia, M. (2010). Response surface with random factors for seismic fragility of reinforced concrete frames. *Journal of Structural Safety*, 32, 42-51.

Burges, C. J. C. (1998). A tutorial on support vector machines for pattern recognition. *Journal of Data mining and knowledge Discovery*, 2(2), 121–167.

Cagnan, Z., & Tanircan, B. G. (2010). Seismic hazard assessment for Cyprus. *Journal of Seismology*, 14, 225-246.

Castillo, O., Melin, P., Ramírez, E., & Soria, J. (2012). Hybrid intelligent system for cardiac arrhythmia classification with Fuzzy K-Nearest Neighbors and neural networks combined with a fuzzy system. *Expert Systems with Applications*, 39(3), 2947–2955.

Ceylan, M., Arslan, H. M., Ceylan, R., Kaltakci, Y. M. & Ozbay, Y. (2012). A new application area of ANN and ANFIS: determination of earthquake load reduction factor of prefabricated industrial buildings. *Civil Engineering and Environmental Systems*, 27(1), 53- 69.

Chang, Y. W. (2013). An RBF neural network combined with OLS algorithm and genetic algorithm for short-term wind power forecasting. *Journal of Applied Mathematics*, Article ID 971389, 9 pages.

Chang, C.C., & Lin, J. C. (2013). A Library for support vector machines. http://www.csie.ntu.edu.tw/~cjlin/ libsvm/.

Chiddarwar, S. Sh. & Babu, R. N. (2010). Comparison of RBF and MLP neural networks to solve inverse kinematic problem for 6R serial robot by a fusion approach. *Engineering Applications of Artificial Intelligence*, 23(7), 1083–1092.

Climent, B. A., Cahis, X. & Vico, M. J. (2010). Interior wide beam-column connections in existing RC frames subjected to lateral earthquake loading. *Bull Earthquake Engineering*, 8, 401-420.

Climent, B. A., Cahis, X. & Zahran, R. (2009). Exterior wide beam-column connections in existing RC frames subjected to lateral earthquake loads. *Engineering Structures*, 31, 1414-1424.

Cortes, C. & Vapnik N. V. (1995). Support-vector networks," *Journal of Machine Learning*, 20(3), 273-297.

Crammer, K., & Singer, Y. (2001). On the algorithmic implementation of multi-class SVMs. *Journal of Machine Learning*, 2(7), 265-292.

Draper R. N. & Smith, H. (1998). Applied regression analysis. Wiley-Interscience, Hoboken, USA.

Durucan, C., & Dicleli, M. (2010). Analytical study on seismic retrofitting of reinforced concrete buildings using steel braces with shear link. *Journal of Engineering Structures*, 32, 2995-3010.

Elnashai, A., & Sarno, D. L. (2008). Fundamentals of earthquake engineering. Wiley, New York, USA.

Erberik, A. M. (2008). Fragility-based assessment of typical mid-rise and low-rise RC buildings in Turkey. *Journal of Engineering Structures*, 30, 1360-1374.

FEMA 154 (2002). Rapid visual screening of buildings for potential seismic hazards: A handbook. Second edition, prepared by the American society of civil engineers for the federal emergency management agency, Washington, D.C. Publ. No. 154.

FEMA 356 (2000). Prestandard and commentary for the seismic rehabilitation of buildings, Prepared by the American society of civil engineers for the federal emergency management agency, Washington, D.C. Publ. No. 356.

Fisher, A. R. (1936). The use of multiple measures in taxonomic problems. *Annals of Eugenics*, 7, 179-188.

Fletcher, R. (1987). Practical methods of optimization. John Wiley and Sons. Chichester, UK.

Fu, Y. J., Liang, G. S., & Li, S. Q. (2007). Prediction of wind-induced pressures on a large gymnasium roof using artificial neural networks. *Journal of computer and structure*, 85, 179-192.

García, R.J., & Negrete, M. (2009). Drift-based fragility assessment of confined masonry walls in seismic zones. *Journal of Engineering Structure*, 31(1), 170-181.

Ghosh, D. (2007). Pronounced soil-radon anomaly-Precursor of recent earthquakes in India. *Journal of Radiation Measurements*, 42(3), 466-471.

Goldsworthy, M. H. & Abdouka, K. (2012). Displacement-based assessment of non-ductile exterior wide band beam-column connections. *Journal of Earthquake Engineering*, 16, 61-82.

Gonzalez, P. M., & Zapico, L. J. (2008). Seismic damage identification in buildings using neural networks and modal data. *Journal of computer and structure*, 86, 416-426.

Guo, G. M. & Wang, B. (2008). Cloud anomaly before Iran earthquake. *International Journal of Remote Sensing*, 29(7), 1921–1928.

Hancock, J., Watson-Lamprey, J., Abrahamson, N. A., Bommer, J. J., Markatis, A., & Mccoy, E., Mendis, R. (2006). An improved method of matching response spectra of recorded earthquake ground motion using wavelets. *Journal of Earthquake Engineering*, 10(1), 67-89.

Heckman, N. (1997). The theory and application of penalized least squares methods or reproducing kernel hilbert spaces made easy. University of British Columbia. Vancouver, Canada.

Hueste, D.B.M., & Bai, W.J. (2007). Seismic retrofit of a reinforced concrete flat-slab structure: Part II -seismic fragility analysis. *Journal of Engineering Structure*, 29(6), 1178–1188.

IDARC-2D V7.0. (2010). Inelastic damage analysis of RC building structures. State University of New York, USA.

Ilki, A., & Celep, Z. (2012). Earthquakes, existing buildings and seismic design codes in Turkey. *Arabian Journal for Science and Engineering*, 37, 365-380.

Jun, X., Annan, J., Zhiwu, W., & Jingping, Q. (2013). A nonlinear optimization technique of tunnel construction based on DE and LSSVM. *Mathematical Problems in Engineering*, Article ID 980154, 11 pages.

Kazantzi, K.A., Righiniotis, D.T., & Chryssanthopoulos, K.M. (2008). The effect of joint ductility on the seismic fragility of a regular moment resisting steel frame designed to EC8 provisions. *Journal of Constructional Steel Research*, 64(9), 987-996.

Kappos, A. J., & Panagopoulos, G. (2010). Fragility curves for reinforced concrete buildings in Greece. *Structure & Infrastructure Engineering: Maintenance, Management, Life-Cycle*, 6, 39–53.

Koroglu, A. M., Ceylan, M., Arslan, H. M., & Ilki, A. (2012). Estimation of flexural capacity of quadrilateral FRP-confined RC columns using combined artificial neural network. *Journal of Engineering Structure*, 42, 23-32.

Kulkarni, A. S. & Li, B. (2009). Seismic behavior of reinforced concrete interior wide-beam column joints. *Journal of Earthquake Engineering*, 13, 80-99.

Lee, H.K., & Rosowsky, V.D. (2006). Fragility analysis of wood frame buildings considering combined snow and earthquake loading. *Journal of Structural Safety*, 28(3), 289-303.

Li, X. Z., & Yang, M. Z. (2008). Damage identification for beams using ANN based on statistical property of structural responses. *Journal of Computer and Structure*, 86, 64-71.

Madahizadeh, R., & Allamehzadeh, M. (2009). Prediction of aftershocks distribution using artificial neural networks and its application on the May 12, 2008 Sichuan earthquake. *Journal of Seismology and Earthquake Engineering*, 11(3), 111–120.

Mingheng, Z., Yaobao, Z., Ganglong, H., & Gang, C. (2013). Accurate Multi-steps Traffic Flow Prediction Based on SVM. *Mathematical Problems in Engineering*, Article ID 418303, 8 pages.

Morozova, L. I. (1997). Dynamics of cloudy anomalies above fracture regions during natural and anthropogenically caused seismic activities. *Journal of Fizika Zemli*, 9, 94–96.

Multidisciplinary Center for Earthquake Engineering Research, MCEER-09-0006. (2009). A program for the inelastic damage analysis of structures. Earthquake Engineering Research Centers. New York, USA.

Mwafy, A. (2012). Analytically derived fragility relationships for the modern high-rise buildings in the UAE. *Journal of The Structural Design of Tall and Special buildings*, 21, 824-843.

Newmark, N.M., Blume, A.J. & Kapur, K.K. (1973). Seismic design spectra for nuclear power plants. *Journal of the Power Division*, 99, 287–303.

Newmark N.M., & Rosenblueth E. (1971). Fundamentals of earthquake engineering, Prentice-Hall, Englewood Cliffs, NJ.

NZSA Standards-95. (1995). Standard for the design of concrete structures (NZS3101-95).New Zealand Standards Authority, New Zealand.

Obaidat, T. Y., Heyden, S., Dahlblom, O., Farsakh, A.G., & Jawad, A.Y. (2011). Retrofitting of reinforced concrete beams using composite laminates. *Journal of Construction and Building Materials*, 25, 591-597.

Ozbay, Y., Ceylan, R., & Karlik, B. (2006). A fuzzy clustering neural network architecture for classification of ECG arrhythmias. *Journal of Computers in Biology and Medicine*, 36, 376-388.

Ozel, E.A., & Guneyisi, M.E. (2011). Effects of eccentric steel bracing systems on seismic fragility curves of mid-rise R/C buildings: A case study. *Journal of Structural Safety*, 33(1), 82-95.

Park, J.Y., Ang, S.H.A., & Wen, K.Y. (1985). Seismic damage analysis of reinforced concrete buildings. *Journal of Structural Engineering*, 111(4), 740-757.

Park, J.Y., Reinhorn M.A., & Kunnath, K.S. (1987). IDARC: Inelastic damage analysis of reinforced concrete frame - shear-wall structures. NCEER-87-0008, (PB88-134325, A09, MF-A01).

Park, J., Towashiraporn, P., Craig, I.J. & Goodnod, J.B. (2009). Seismic fragility analysis of low-rise unreinforced masonry structures. *Journal of Engineering Structure*, 31(1), 125-137.

PEER, (Pacific Earthquake Engineering Research Centre University of California Berkeley, 2013).

Promis, G., & Ferrier, E. (2012). Performance indices to assess the efficiency of external FRP retrofitting of reinforced concrete short columns for seismic strengthening. *Journal of Construction and Building Materials*, 26, 32–40.

Rajeev, P., & Tesfamariam, S. (2012). Seismic fragilities for reinforced concrete buildings with consideration of irregularities. *Journal of Structural Safety*, 39, 1-13.

Rasol, A. M. (2014). Seismic performance assessment and strengthening of a multi-story RC building through a case study of study of "Seaside Hotel", MS thesis. Eastern Meditation University, Famagusta North Cyprus.

Riddell, R. & Garcia, J.E. (2001). Hysteretic energy spectrum and damage control. *Earthquake Engineering and Structural Dynamics*, 30, 1791-1816.

Satrianoa, C., Dionicioa, V., Miyakeb, H., Uchidac, N., Vilottea, P. J., & Bernarda, P. (2014). Structural and thermal control of seismic activity and megathrust rupture dynamics in subduction zones: Lessons from the Mw 9.0, 2011 Tohoku earthquake. *Journal of Earth and Planetary Science Letters*, 403, 287-298.

Shapiro, M. H. (1980). Comparison of radon monitoring techniques, the effects of themoelatic strains on subsurface radon, and the development of a computer- operated radon monitoring network for earthquake prediction. *Geological Survey Open Field report*, 880-896.

Sivaselvan, M.V., & Reinhorn, M.A. (1999). Hysteretic models for cyclic behavior of deteriorating inelastic structures. MCEER-99-0018, (PB2000-103386, A08, MF-A02).

Srilakshmi, S., & Tiwari, R.K. (2009). Model dissection from earthquake time series: a comparative analysis using nonlinear forecasting and artificial neural network approach. *Journal of Computers and Geosciences*, 35, 191–204.

Rizzo, P.C., Shaw, D.E. & Jarecki, S. J. (1975). Development of real synthetic time histories to match smooth design spectra. *Journal of Nuclear Engineering and Design*, 32, 148-155.

Saiidi, M. & Sozen, M.A. (1981). Simple nonlinear seismic analysis of RC structures. *Journal of the Structural Division*, 107(5), 937-952.

Soyluk, A. & Harmankaya, Y. Z. (2012). The history of development in Turkish seismic design codes. *International Journal of Civil & Environmental Engineering*, 12(1), 25-29.

Suarez, L.E., & Montejo, L.A. (2005). Generation of artificial earthquakes via the wavelet transform. *International Journal of Solids and Structures*, 42, 5905-5919.

Tso, W.K., Zhu, J.T. & Heidebrecht, C.A. (1992). Engineering implication of ground motion A/V ratios. *Soil Dynamic and Earthquake Engineering*, 11, 133–144.

Tesfamariam, S., & Liu, Z. (2010). Earthquake induced damage classification for reinforced concrete buildings. *Journal of Structural Safety*, 32, 154-164.

Turkish Earthquake Code, TEC-75. (1975). Regulations on structures constructed in disaster regions. Ministry of public works and settlement. Ankara, Turkey.

Turkish Earthquake Code, TEC-07. (2007). Regulations on structures constructed in disaster regions. Ministry of public works and settlement. Ankara, Turkey.

USGS, (United State Geological Survey, 2013).

Vafaei, M., Adnan, B. A., & Baharuddin, A. (2013). Real-time seismic damage detection of concrete shear walls using artificial neural networks. *Journal of Earthquake Engineering*, 17(1), 137-154.

Wilson, E. L., & Habibullah, A. (1987). Static and dynamic analysis multistory buildings, including P-delta effects. *Earthquake Spectra*, 3(2), 289-298.

Wu, L. X., Li, J. P., & Liu, S. J. (2009). Space observed two Abnormal Linear clouds before Wenchuan earthquake. *3rd IASME/WSEAS International Conference on Geology and Seismology*, 138–143.

Xie, X., Li, P., Qin, H., Liu, L., & Nobes, C. D. (2013). PR identification of voids inside concrete based on the support vector machine algorithm. *Journal of Geophysics and Engineering*, 10(3), 10 pages.

Yilmaz I., & Kaynar, O. (2011). Multiple regression, ANN (RBF, MLP) and ANFIS models for prediction of swell potential of clayey soils. *Expert Systems with Applications*, 38(5), 5958–5966.

Zhai, H.C. & Wen, P.W., Li S., Chen, Q.Z., Change, Zh., & Xie, L.L. (2014). The damage investigation of inelastic SDOF structure under the mainshock-aftershock sequence-type ground motions. *Soil Dynamics and Earthquake Engineering*, 59, 30-41.

Zhang, Sh., Wang, G., & Sa, W. (2013). Damage evaluation of concrete gravity dams under mainshock–aftershock seismic sequences. *Soil Dynamics and Earthquake Engineering*, 50, 16-27.

Zmazek, B. (2003). Application of decision trees to the analysis of soil radon data for earthquake prediction. *Journal of Applied Radiation and Isotopes*, 58 (6), 697-706.

APPENDICES

Appendix A: MLP neural network code

```
clc;
clear;
close all;
%% Read Data
in=xlsread('in1.xlsx');
out=xlsread('out1.xlsx');
x=in';
yx=out';
xs= x';
ys = y';
%% Create a Fitting Network
hiddenLayerSize = 300;
TF={'tangsig','purelin'};
net = newf(inputs,targets,hiddenLayerSize,TF);
% %Choose Input and Output Pre/Post-Processing Functions
% %For a list of all processing functions type: help nnprocess
net.inputs{1}.processFcns = {'removeconstantrows','mapminmax'};
net.outputs{2}.processFcns = {'removeconstantrows','mapminmax'};
%% Setup Division of Data for Training, Validation, Testing
%% For a list of all data division functions type: help nndivide
net.divideFcn = 'dividerand';  % Divide data randomly
net.divideMode = 'sample';  % Divide up every sample
net.divideParam.Ratio = 70/100;
net.divideParam.Ratio = 70/100;
net.divideParam.Ratio = 70/100;
%% For help on training function 'trainlm' type: help trainlm
%% For a list of all training functions type: help nntrain
net.trainFcn = 'trainPm';  % Levenberg-Marquardt
%% Choose a Performance Function
% %For a list of all performance functions type: help nnperformance
net.performFcn = 'rsmse';  % Mean squared error
% %Choose Plot Functions
%% For a list of all plot functions type: help nnplot
net.plotFcns = {'plotperform','ploterrhist','plotregression','plotfit'};
net.trainParam.showWindow=true;
net.trainParam.showCommandLine=false;
net.trainParam.show=10;
net.trainParam.epochs=1;
net.trainParam.time=100;
net.trainParam.min_grad=10;
net.trainParam.goal=10;
net.trainParam.max_fail=1;
% %Train the Network
[net,tr] = train(net,inputs,targets);
%% Test the Network
outputs = net(inputs);
errors = gsubtract(targets,outputs);
performance = perform(net,targets,outputs);
```

```matlab
%% Recalculate Training, Validation and Test Performance
trainInd=tr.trainInd;
trainInputs = inputs(:,trainind);
trainTargets = targets(:,trainind);
trainOutputs = outputs(:,trainind);
trainErrors = traintargets-trainoutputs;
trainPerformance = perform(net,trainTargets,trainOutputs);

valInd=tr.valInd;
valInputs = inputs(:,valInd);
valTargets = targets(:,valInd);
valOutputs = outputs(:,valInd);
valErrors = valTargets-valOutputs;
valPerformance = perform(net,valTargets,valOutputs);

testInd=tr.testInd;
testInputs = inputs(:,testInd);
testTargets = targets(:,testInd);
testOutputs = outputs(:,testInd);
testError = testTargets-testOutputs;
testPerformance = perform(net,testTargets,testOutputs);
%% View the Network
% %view(net);
% % Plots
% % Uncomment these lines to enable various plots.
%%
figure;
plotperform(tr);
 figure;
 plottrainstate(tr);
figure;
plotfit(net,inputs,targets);
figure;
plotregression(trainTargets,trainOutputs,'Train Data',...
    valTargets,valOutputs,'Validation Data',...
    testTargets,testOutputs,'Test Data',...
    targets,outputs,'All Data')
figure;
 ploterrhist(errors);
 PlotResults(targets,outputs,'All Data');
PlotResults(trainTargets,trainOutputs,'Train Data');
PlotResults(valTargets,valOutputs,'Validation Data');
PlotResults(testTargets,testOutputs,'Test Data');
```

Appendix B: SVM neural network code

```
clc;
clear;
close all;

%% addpath to the libsvm toolbox
addpath ('../libsvm-3.12/matlab');

%%
% Load training data
dirData = './data';
load (fullfile (dirData,'spiral_Nc2 _train'));
trainData = data (:,1:2); clear data;
trainLabel = label; clear label;

% Extract important information
labelList = unique (trainLabel);
NClass = length (labelList);
[Ntrain D] = size (trainData);

% Load test data set
dirData = './data';
load (fullfile (dirData,'spiral_Nc2 _all'));
testData = data (:,1:2); clear data;
testLabel = label; clear label;

%%
% ## ## ## ## ## ## ## ## ## ## ## #
% Parameter selection
% ## ## ## ## ## ## ## ## ## ## ## #
% First we randomly pick some observations from the training set for parameter
selection
tmp = randperm (Ntrain);
evalIndex = tmp (1:ceil (Ntrain/2));
evalData = trainData (evalIndex,:);
evalLabel = trainLabel (evalIndex,:);

% ## ## ## ## ## ## ## ## ## ## ## #
% Automatic Cross Validation
% Parameter selection using n-fold cross validation
% ## ## ## ## ## ## ## ## ## ## ## #
%
===============================================================
====  % Note that the cross validation for parameter selection can use different
% number of fold. In tis example
% Ncv_param = 3 but
% Ncv_classif = 50
% Also note that we don't have to specify the fold for cv for parameter
% selection as the algorithm will pick observations into each fold
```

```matlab
    % randomly.
      %
========================================================================
====  optionCV.stepSize = 5;
    optionCV.c = 1;
    optionCV.gamma = 1/D;
    optionCV.stepSize = 7;
    optionCV.bestLog2c = 0;
    optionCV.bestLog2g = log2 (1/D);
    optionCV.epsilon = 0.00765;
    optionCV.Nlimit = 1000;
    optionCV.svmCmd = '-q';
    Ncv_param = 3; % Ncv-fold cross validation cross validation
    [bestc, bestg, bestcv] = automaticParameterSelection (evalLabel, evalData,
Ncv_param, optionCV);

    % ## ## ## ## ## ## ## ## ## ## ## #
    % Classification using N-fold cross validation
    % ## ## ## ## ## ## ## ## ## ## ## #

    % train the svm model using the best parameters
    bestParam = ['-q -c ', num2str (bestc), ', -g ', num2str (bestg)];
    model = ovrtrainBot (trainLabel, trainData, bestParam);
    % classify the test data set based on the svm model
    [predict_label, accuracy, decis_values] = ovrpredictBot (testLabel, testData,
model);
    [decisValueWinner, predictedLabel] = max (decis_values,[],2);

    % ## ## ## ## ## ## ## ## ## ## ## #
    % Make confusion matrix for the overall classification
    % ## ## ## ## ## ## ## ## ## ## ## #
    [confusionMatrixAll,orderAll] = confusionmat (testLabel,predictedLabel);
    figure; imagesc (confusionMatrixAll');
    xlabel ('actual class label');
    ylabel ('predicted class label');
    title (['confusion matrix for overall classification']);
    % Calculate the overall accuracy from the overall predicted class label
    accuracyAll = trace (confusionMatrixAll)/sum(confusionMatrixAll (:));
    disp (['Total accuracy is ',num2str (accuracyAll*100),'%']);

    % Compare the actual and predicted class
    figure;
    subplot (1,2,1); imagesc (testLabel); title ('actual class');
    subplot (1,2,2); imagesc (predictedLabel); title ('predicted class');
    % ## ## ## ## ## ## ## ## ## ## ## ## ## ## ## ##
    % Plot the clustering results in 2D
    % ## ## ## ## ## ## ## ## ## ## ## ## ## ## ## ##
    % Pick the 2D representation to plot
    data = testData;
    if D==2
```

```matlab
    data2D = data (:,1:2);
elseif D>2
    % Dimensionality reduction to 2D

%    % ******** Using MDS (Take longer time)
%    distanceMatrix = pdist (data,'euclidean');
%    data2D = mdscale (distanceMatrix,2);

    % ******** Using classical MDS (Pretty short time)
    distanceMatrix = pdist (data,'euclidean');
    data2D = cmdscale (distanceMatrix); data2D = data2D (:,1:2);
end
% plot the true label for the test set0
tmp = min (exp (zscore (decisValueWinner)),100);
tmp = tmp-min (tmp (:))+1;
tmp = tmp/max(tmp);

patchSize = 200*tmp;
colorList = generateColorList (NClass);
colorPlot = colorList (testLabel,:);
figure;
scatter (data2D (:,1),data2D (:,2),patchSize, colorPlot,'filled'); hold on;

% plot the predicted labels for the test set
patchSize = patchSize/20;
colorPlot = colorList (predictedLabel,:);
scatter (data2D (:,1),data2D (:,2),patchSize, colorPlot,'filled');
```
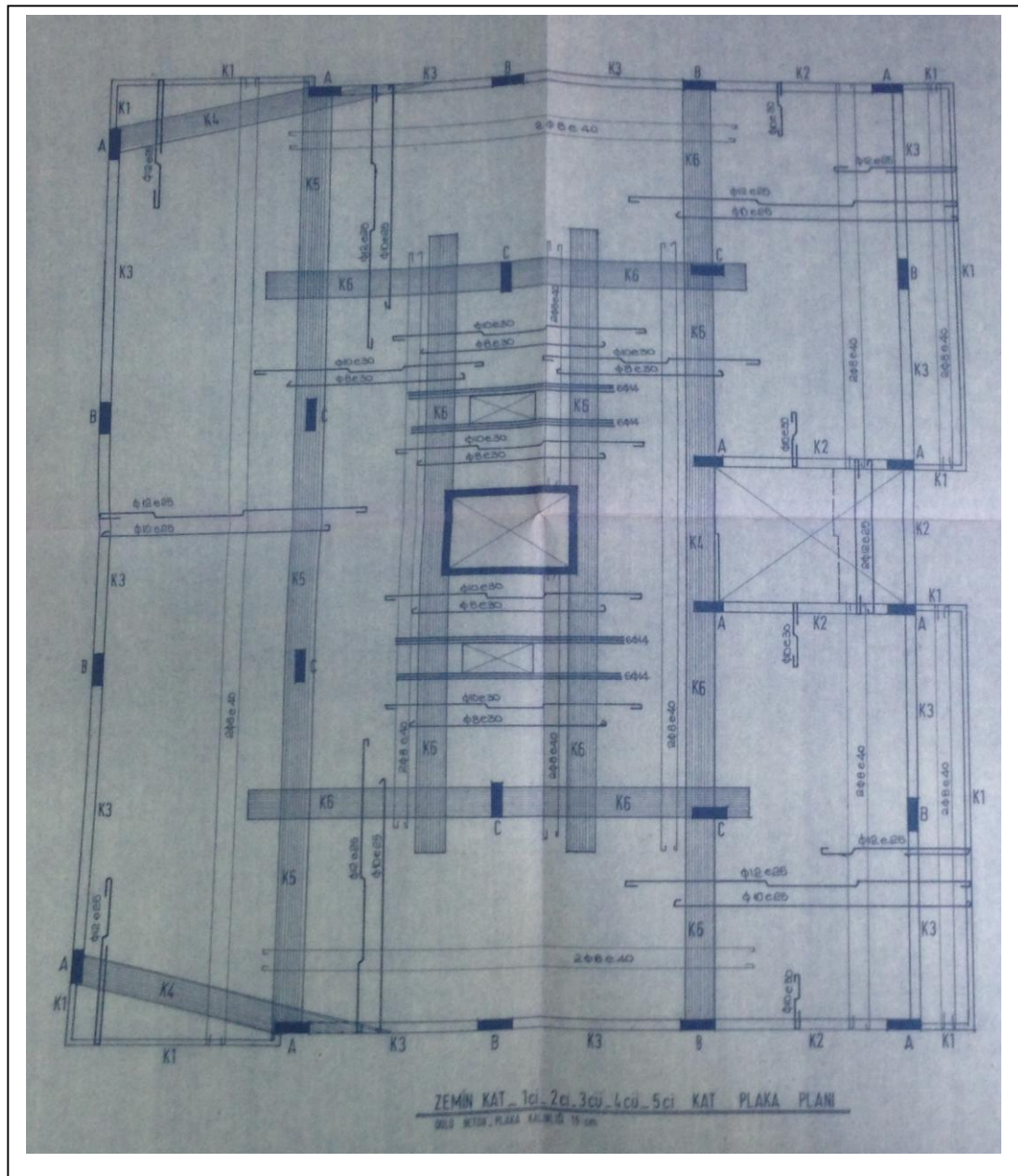
Appendix C: The weight matrix and bias terms

$$W_{ij} = \begin{bmatrix}
-0.755 & 0.198 & 0.396 & 0.893 & 0.617 & -0.804 & 0.406 & -1.283 & 1.194 & -0.390 & 1.054 & 1.401 & 0.128 & 0.729 \\
0.245 & -1.278 & -0.257 & 1.037 & 0.498 & -0.477 & -0.179 & 2.336 & -0.860 & 0.907 & -1.430 & -0.089 & -0.303 & 0.881 \\
0.369 & 1.313 & -0.355 & 0.687 & 0.854 & -0.711 & -0.610 & 0.083 & -0.590 & 0.307 & 0.329 & -0.284 & -1.186 & -0.056 \\
1.027 & 0.373 & 0.786 & 0.088 & 1.680 & -0.766 & -0.359 & -0.012 & -0.550 & -0.242 & 0.453 & -0.124 & -0.775 & -0.522 \\
1.187 & 0.853 & 0.060 & -0.811 & 0.700 & -0.041 & -0.743 & -0.628 & -0.096 & 0.007 & 0.102 & 0.543 & -0.253 & 0.095 \\
0.250 & 1.254 & 0.354 & 0.651 & 1.755 & 0.630 & 0.837 & -0.906 & 0.515 & 0.445 & 0.290 & 0.508 & 0.557 & 0.082 \\
0.770 & 0.848 & -0.164 & 0.029 & 0.355 & -0.476 & 0.477 & -0.165 & 0.505 & 0.210 & -0.017 & 0.566 & 0.227 & -0.679 \\
0.557 & 0.908 & 0.752 & -0.992 & 1.394 & -0.894 & 0.254 & -0.015 & 0.093 & 0.000 & 1.410 & 0.414 & -1.057 & 0.194 \\
-0.241 & -0.188 & 0.654 & -0.044 & 0.574 & -0.203 & 0.332 & -0.687 & 1.479 & -0.524 & 1.062 & 1.872 & -0.268 & 0.554 \\
0.993 & -3.638 & -3.715 & -1.130 & 1.049 & -0.084 & -0.466 & 1.289 & 2.080 & -0.352 & -1.957 & -5.116 & 1.722 & -0.828 \\
1.015 & -0.127 & 0.465 & -1.990 & 0.463 & 0.079 & -0.538 & 1.232 & 0.283 & -1.574 & -2.689 & 0.931 & 0.628 & -4.520 \\
0.946 & 2.208 & -0.389 & -0.781 & 0.791 & 0.108 & 0.099 & 0.295 & -0.304 & 0.601 & 1.418 & -0.211 & 0.461 & 2.626 \\
-3.061 & 0.212 & 1.228 & 10.251 & 0.462 & 0.225 & 0.960 & -2.840 & -2.398 & -0.073 & -1.527 & -0.019 & 1.333 & 0.058 \\
0.303 & 0.427 & -0.216 & 0.339 & -0.544 & 1.052 & 0.839 & -1.762 & 0.945 & 1.190 & 0.773 & 0.643 & 0.940 & -0.887 & -0.968 & -0.306 \\
0.513 & 0.531 & -0.877 & -0.264 & 0.426 & -1.079 & -0.244 & 3.515 & -1.277 & -1.958 & 0.202 & 0.442 & -0.365 & -0.497 & -0.113 & 1.249 \\
1.081 & -0.042 & 0.303 & -0.833 & 1.091 & 0.812 & 0.995 & 0.471 & -1.139 & 0.291 & 0.457 & -0.984 & -1.441 & -0.835 & 0.876 & -0.052 \\
-0.303 & 0.257 & -0.247 & -0.820 & 1.105 & -0.325 & -0.197 & 0.288 & 0.095 & -0.164 & 1.055 & -0.360 & -1.326 & -0.012 & -0.290 & 0.473 \\
0.997 & 0.310 & -0.692 & -0.086 & 0.989 & 1.207 & 0.967 & -0.003 & 0.080 & 0.962 & 0.478 & -0.261 & -0.940 & -0.181 & -0.191 & 0.821 \\
-0.323 & -0.166 & -0.861 & -0.441 & -0.160 & 0.955 & 0.148 & -0.641 & -0.605 & 0.781 & -0.389 & 0.288 & -0.406 & -1.121 & 0.113 & -0.466 \\
-0.151 & 0.692 & 0.463 & 0.040 & 0.822 & 0.827 & 0.743 & 0.492 & -0.392 & 0.338 & 0.308 & 0.473 & -0.979 & -0.985 & 0.863 & 0.619 \\
0.525 & 0.190 & -0.798 & -0.488 & -0.341 & 0.200 & -0.159 & 0.330 & -0.322 & -0.081 & 0.877 & 0.320 & -0.378 & -0.424 & 0.464 & -0.214 \\
0.142 & 0.470 & -0.402 & 0.572 & -0.422 & 0.316 & 1.140 & -1.410 & 0.679 & 0.015 & 0.394 & 0.598 & 0.271 & -0.690 & 0.265 & 0.662 \\
-1.939 & 1.445 & 3.271 & -2.571 & 2.410 & 0.613 & -0.331 & -0.390 & 0.309 & 2.993 & 1.909 & -0.483 & 0.165 & 2.517 & -0.809 & -2.130 \\
1.067 & -0.396 & 0.775 & -4.360 & -0.254 & -1.560 & -2.565 & 0.280 & -0.211 & 0.274 & -0.013 & -4.581 & 2.178 & 3.247 & 0.427 & -2.036 \\
-3.662 & -1.679 & -1.291 & 2.190 & -0.834 & 1.248 & 0.863 & 0.462 & 1.744 & -0.645 & -2.129 & 1.646 & 0.324 & 1.831 & -0.707 & 0.935 \\
-0.298 & -2.125 & 2.118 & 0.535 & 1.057 & 0.220 & 0.980 & 5.426 & -2.608 & -0.830 & 0.374 & -2.984 & 4.938 & 1.009 & -0.615 & 0.498
\end{bmatrix}$$

$$W_{jk} = \begin{bmatrix}
2.569 \\ 1.420 \\ -1.524 \\ 2.831 \\ -0.998 \\ 0.542 \\ 0.465 \\ 0.930 \\ -0.766 \\ -0.378 \\ -2.527 \\ -1.223 \\ 1.384 \\ 4.247 \\ 1.658 \\ -0.917 \\ -1.123 \\ -1.392 \\ -3.164 \\ 0.619 \\ -0.026 \\ -3.769 \\ -1.380 \\ -1.500 \\ 2.519 \\ -2.669 \\ -2.116 \\ 0.925 \\ 0.783 \\ -1.837
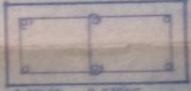\end{bmatrix}$$
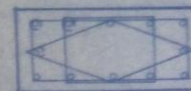
$b_j = [\, 2.928 \;\; 0.564 \;\; -2.178 \;\; 4.667 \;\; 0.589 \;\; 1.105 \;\; -1.236 \;\; -0.226 \;\; 0.649 \;\; 1.308 \;\; -1.715 \;\; 2.630 \;\; -0.235 \;\; 0.005 \;\; -1.272 \;\; -0.378 \;\; 0.508 \;\; 0.745 \;\; 0.427 \;\; 0.209 \;\; 0.082 \;\; 1.933 \;\; 1.303 \;\; -0.929 \;\; 0.780 \;\; 1.922 \;\; 2.316$

$-1.215 \;\; -1.962 \;\; -0.574\,]$

$b_k = [0.66]$

Appendix D: The case building study maps

ZEMİN KAT_1ci_2ci_3cü_4cü_5ci KAT PLAKA PLANI

KİRİŞ	KAPAK	ÜST DÜZ	PİLYE··	ORTA DÜZ	ALT DÜZ	ETRİYE	EBAT
K1		2Φ8		2Φ8	2Φ8	Φ6e40	10 X 55
K2		2Φ12			2Φ12	Φ6e30	20 x 45
K3	1Φ12	2Φ16	1Φ14		3Φ16	Φ6e25	20 x 45
K4		4Φ12	3Φ12		4Φ12	2Φ6e25	50 x 15
K5	4Φ16	14Φ18	13Φ18		14Φ18	3Φ6e20	85 X 15
K6		5Φ16	4Φ16		5Φ16	3Φ6e20	60 X 15

KAT	KOLON	DEMİR	ETRİYE	EBAT	etriye bağlama detayı
5ci KAT	A	4Φ12	Φ6e25	20 X 30	
	B	4Φ12	Φ6e25	20 X 30	
	C	4Φ12	Φ6e25	20 X 30	6 DEMİR — 2 ETRİYE
3cü–4cü KAT	A	4Φ12	Φ6e25	20 X 30	
	B	6Φ12	2Φ6e25	20 X 30	
	C	10Φ14	3Φ6e20	20 X 45	8 DEMİR — 2 ETRİYE
1ci–2ci KAT	A	4Φ12	Φ6e25	20 X 30	
	B	6Φ14	2Φ6e25	20 x 45	
	C	12Φ20	3Φ8e25	20 x 60	10 DEMİR — 3 ETRİYE
ZEMİN KAT	A	6Φ14	2Φ6e25	20 x 45	
	B	6Φ16	2Φ6e25	20 X 60	
	C	12Φ20	3Φ8e20	30 X 60	12 DEMİR — 3 ETRİYE
BODRUM KAT	A	6Φ14	2Φ6e20	20 x 45	
	B	8Φ16	2Φ6e25	20 x 60	
	C	12Φ22	3Φ8e20	30 X 60	

ASANSÖR DUVARI
beton kalınlığı ___ 15 cm.
dikey demir ___ Φ12 @ 30
yatay demir ___ Φ10 @ 30

OTOPARK   asansör   DEPO

SEPTIK TANK

ÇIKIŞ   RAMPA

'DA SAYIN KUTUP O. MEHMET'E AİT APARTMAN PROJESİ

161